TECHNISCHE
UNIVERSITÄT
WIEN

DISSERTATION

Quantum simulation of effective field theories with one-dimensional ultra-cold Bose gases

ausgeführt zum Zwecke der Erlangung des akademischen Grades eines
Doktors der technischen Wissenschaften

unter Leitung von
Univ.Prof. Dipl.-Ing. Dr.techn. Hannes-Jörg Schmiedmayer
E141 Atominstitut

eingereicht an der Technische Universität Wien
Fakultät für Physik

von
Dipl.-Ing. Mohammadamin Tajik
[redacted]

Wien, August 2023

M. Tajik

Gutachter:

H-J. Schmiedmayer

Silke Weinfurtner

Nelly Ng Huei Ying

به جان جمله مستان که مستم
به جان جمله جانبازان که جانم
عطاردوار دفترباره بودم
چو دیدم لوح پیشانی ساقی

بگیر ای دلبر عیار دستم
به جان رستگارانش که رستم
زبردست ادیبان می نشستم
شدم مست و قلم‌ها را شکستم

Acknowledgements

First and foremost, I am very grateful to my supervisor, Jörg Schmiedmayer, for his trust. When I first entered his group as a project student back in 2015, I had zero experience working in a lab and couldn't even tell the difference between M4 and M6 screws. His trust in my enthusiasm and, of course, Bernhard's expertise, who supervised me, resulted in an exciting master's project and a series of projects presented in this Ph.D. thesis.

Now that I mentioned his name, I want to thank Bernhard Rauer for everything he taught me and for his patience and kindness. As a Ph.D. student, he spared his time to train me and help me with the DMD project.

Next, I want to thank Thomas Schweigler. After I started my Ph.D., he was my mentor on the KRb experiment. He helped me with data analysis and gave us a solid framework for different simulations. I immensely enjoyed our discussions and learned a lot from him.

Continuing with my mentors, I want to thank Spyros Sotiriadis and Ivan Kukuljan. They are my friends, collaborators, and my theory teachers. The work presented in this thesis was only possible with their insight and hard work. Our late-night Zoom meetings will be missed.

Speaking about theory support, I must thank Sebastian Erne and Igor Mazets for their excellent knowledge and willingness to help. I learned a lot from discussing with them.

I was honored to collaborate with profound theoretical physicists, including Marek Gluza, Eugene Demler, Jens Eisert, and Dries Sels. I am grateful for their contributions to the works presented in this thesis.

Running a cold-atom apparatus is not possible without a caring and responsible team. I was lucky to be a part of such a team, plus, they were extremely fun and kind. On this note, let me thank my friends and KRb teammates whose expertise and stimulating discussions were invaluable. First up is our Gallipolina, Federica Cataldini, a joyful person, a natural dancer, and a fun travel companion. I thank Fede also for proofreading parts of my thesis. Next, Frederik Møller, who is excellent at organizing sports events and generalized hydrodynamics. And then, our Frenchman Nicolas Sebe, with whom I have fond memories in Vienna and Berlin. I thank our humble and helpful Si-Cong Ji, who was there whenever I needed help. He also kindly proofread parts of this thesis. And, of course, João "Aritza" David Ventura Sabino, with whom I spent most of my time in the lab. It's hard to highlight specific moments from all our fun in and outside ATI, but indeed, being his best man at his brilliant wedding was an honor I won't forget. I wish the best of luck to the next generation of KRb students, Philipp Schüttelkopf and Nataliia Bazhan. Philipp already did a great job exchanging our Rubiduim dispenser, and Nataliia is taking over one of the exciting projects that I started. I also thank both of them for proofreading parts of my thesis.

My special thanks go to my dear Stephan Schneider. It was a pleasure and honor to work with him, not only because of his management skills and insight into administrative issues but also because he was helpful in the lab and a fun drinking partner in the coffee corner. He made the life of a lot of people a lot easier.

I thank my former and current officemates and friends Thomas Weigner, whom I never saw in a bad mood, "MC" Wenzel Kersten for being the best office DJ in the world, and Nikolaus de Zordo, for tolerating/enjoying my loud Zoom meetings.

I have to thank my dear Filippo "Fava" Borselli for deviating the topic of all conversations in the coffee corner to "ducks", "Mon Professeur" Camille Leveque for taking me to Boulderbar and teaching me how to climb, "Prince" Pradyumna Paranjape for amazing Indian desserts he brings or makes and for teaching me how to make Indian Chai, Andreas Angerer for organizing Champions League nights, Mira Maiwöger and Tom Astner for cooking awesome lunches. I am grateful to Rug-Way Wu, Chen Li, and Qi Liang for lending us equipment, no questions asked. I thank Max Prüfer for proofreading parts of this thesis. I thank Tiantian Zhang for the fun conversations during coffee breaks between writing. Having a writing buddy while wrapping up a Ph.D. thesis is fantastic. I'm happy we were writing our theses at the same time. I must mention my dear friend Riya Sett, a fun physicist who sings and dances "Bandari" very well. Also, my Iranian comrades Niyusha Hosseini and Hamid Haghmoradi. Their encouraging words were heartwarming.

And finally, who deserves a long hug more than the charming American who convinced me to write such a long acknowledgment? I thank Andrew Kanagin for being optimistic, loud, and genuine. He invited and hosted me at his parent's in Arizona and took me to Grand Canyon and Vegas. His black Lamy Safari will stay with me forever.

I have to thank the administrative staff at the Atominstitut, especially Barbara Stros, Britta Buchberger, and Evgeniya Schimpf. My special thanks go to the mechanical workshop of Atominstitut for the rapid handling of machining the parts needed for our experiment. I also appreciate the help of Andrzej Pelczar and his team in the electronics workshop.

I am grateful to Silke Weinfurtner and Nelly Ng for kindly agreeing to review my thesis.

I would also like to thank Rob Phillips for hosting me at Caltech for five months and allowing me to learn about out-of-equilibrium dynamics in biophysics. My sincere thanks also go to the whole Phillips group for their kindness, especially to Heun-Jin Lee, my lab advisor.

A heartfelt thank you to my dear parents, my supportive mother-in-law, my dear Dayi Hamid, and Dayi Mohammad, and my most beloved aunt Ghaghi for providing me with unfailing support and continuous encouragement throughout my years of study. This accomplishment would not have been possible without them.

My deepest gratitude goes to my sister, Zeinab, and our dear friends, Mina and Sona. They were always there for me, especially during Covid lockdowns, offering a listening ear and a helping hand whenever I needed it. Their unwavering support and encouragement are highly appreciated.

Last but not least, my special thanks go to my dear Kamelia for her constant support and love during my studies and her patience through the writing process. Without her, this achievement would have been tasteless.

Abstract

In the past decade, experimental and theoretical physicists joined forces to study quantum field theory in one-dimensional Bose gases. The efforts have proven these ultra-cold gases a reliable analog quantum simulator, as they are highly tunable and well isolated from their environment. This thesis studies the quantum field simulation of the Klein-Gordon model using a pair of quasi-one-dimensional tunneling-coupled Bose gases on an atom chip. We will first briefly overview the experimental setup after introducing the theoretical framework. We will then present one of the significant advances to the atom chip experiments, enabling arbitrary one-dimensional confinements for cold gases. Afterward, we study the scaling and propagation of information in the Klein-Gordon model. First, we measure the von Neumann entropy and quantum mutual information for thermal and prethermalized Gaussian states in the experiment and verify the long-standing prediction of the area law of quantum mutual information for thermal states of the Klein-Gordon model. We then investigate the post-quench dynamics of correlations on a simulated inhomogeneous metric propagating on curved light cones. This thesis represents a step toward utilizing one-dimensional ultra-cold quantum simulators to measure entanglement in quantum field theories and to study field theories with inhomogeneous metrics. The tools introduced in this work set the ground for exploring these topics in interacting quantum field theories, such as the sine-Gordon model.

Zusammenfassung

Im letzten Jahrzehnt haben sich experimentelle und theoretische Physiker zusammengetan, um die Quantenfeldtheorie der eindimensionalen Bose-Gase zu untersuchen. Dabei haben sich ultrakalte Gase als zuverlässige analoge Quantensimulatoren erwiesen, da sie hochgradig regelbar und gut von ihrer Umgebung isoliert sind. Diese Arbeit untersucht die Quantenfeldsimulation des Klein-Gordon-Modells unter Verwendung eines Paares quasi-eindimensionaler tunnelgekoppelter Bose-Gase auf einem Atomchip. In dieser Arbeit werden wir nach einer Einführung des theoretischen Rahmens einen kurzen Überblick über den experimentellen Aufbau geben. Anschließend stellen wir eine der wichtigsten Verbesserungen des Experiments vor, die beliebige eindimensionales Fallenpotential für kalte Gase ermöglicht. Anschließend untersuchen wir das Skalieren und Ausbreitung von Information im Klein-Gordon-Modell. Dafür messen wir zunächst die von-Neumann-Entropie und die Quanten-Gegenseitigkeitsinformation für thermische und präthermalisierte Gauß'sche-Zustände im Experiment und verifizieren die seit langem bestehende Vorhersage des Flächengesetzes der Quanten-Gegenseitigkeitsinformation für thermische Zustände des Klein-Gordon-Modells, das einen Hamiltonoperator mit einer spektralen Lücke beschreibt. Dannach untersuchen wir die Post-Quench-Dynamik von Korrelationen auf einer simulierten inhomogenen Metrik, die sich als gekrümmte Lichtkegel ausbreiten. Diese Arbeit ist ein Schritt in Richtung der Nutzung eindimensionaler ultrakalter Quantensimulatoren zur Messung der Verschränkung in Quantenfeldtheorien und zur Untersuchung von Feldtheorien mit inhomogenen Metriken. Die in dieser Arbeit vorgestellten Werkzeuge bilden die Grundlage für die Erforschung dieser Themen in wechselwirkenden Quantenfeldtheorien, wie dem sine-Gordon-Modell.

Publications

Parts of this thesis have been published in the following publications:

- M. Tajik, B. Rauer, T. Schweigler, F. Cataldini, J. Sabino, F. Møller, S.-C. Ji, I. Mazets and J. Schmiedmayer
  Designing arbitrary one-dimensional potentials on an atom chip
  Opt. Express 27, 33474-33487 (2019); arXiv:1908.01563
- A. Deutschmann-Olek, M. Tajik, M. Calzavara, J. Schmiedmayer, T. Calarco, and A. Kugi
  Iterative shaping of optical potentials for one-dimensional Bose-Einstein condensates
  in 2022 IEEE 61st Conference on Decision and Control (CDC), pp. 5801–5806, (2022); arXiv:2208.00706
- M. Tajik, I. Kukuljan, S. Sotiriadis, B. Rauer, T. Schweigler, F. Cataldini, J. Sabino, F. Møller, P. Schüttelkopf, S.-C. Ji, D. Sels, E. Demler and J. Schmiedmayer
  Verification of the area law of mutual information in a quantum field simulator theory
  Nature Physics 19, pages 1022–1026 (2023); arXiv:2206.10563
- M. Tajik, M. Gluza, N. Sebe, P. Schüttelkopf, F. Cataldini, J. Sabino, F. Møller, S.-C. Ji, S. Erne, G. Guarnieri, S. Sotiriadis, J. Eisert and J. Schmiedmayer
  Experimental observation of curved light-cones in a quantum field simulator
  Proceedings of the National Academy of Sciences, vol. 120, no. 21, p. e2301287120, (2023); arXiv:2209.09132

Other publications to which the author has contributed:

- B. Rauer, S. Erne, T. Schweigler, F. Cataldini, M. Tajik, and J. Schmiedmayer
  Recurrences in an isolated quantum many-body system
  Science, vol. 360, no. 6386, pp. 307–310, (2018); arXiv:1705.08231
- T. Schweigler, M. Gluza, M. Tajik, S. Sotiriadis, F. Cataldini, S.-C. Ji, F. Møller, J. Sabino, B. Rauer, J. Eisert and J. Schmiedmayer
  Decay and recurrence of non-Gaussian correlations in a quantum many-body system
  Nature Physics 17 (5), 559-563 (2021); arXiv:2003.01808
- F. Møller, T. Schweigler, M. Tajik, J. Sabino, F. Cataldini, S.-C. Ji and J. Schmiedmayer
  Thermometry of one-dimensional Bose gases with neural networks
  Phys. Rev. A 104 (4), 043305 (2021); arXiv:2105.03127
- S.-C. Ji, T. Schweigler, M. Tajik, F. Cataldini, J. Sabino, F. Møller, S. Erne and J. Schmiedmayer
  Floquet engineering a bosonic Josephson junction
  Phys. Rev. Lett. 129, 080402 (2022); arXiv:2202.06873
- M. Gluza, T. Schweigler, M. Tajik, J. Sabino, F. Cataldini, F. Møller, S.-C. Ji, B. Rauer, J. Schmiedmayer, J. Eisert and S. Sotiriadis
  Mechanisms for the emergence of Gaussian correlations
  SciPost Physics 12 (3), 113 (2022); arXiv:2108.07829
- F. Cataldini, F. Møller, M. Tajik, J. Sabino, T. Schweigler, S.-C. Ji, B. Rauer and J. Schmiedmayer
  Emergent Pauli blocking in a weakly interacting Bose gas
  Phys. Rev. X 12, 041032 (2022); arXiv:2111.13647

Contents

1 Introduction **1**

2 Effective field theories describing cold bosons **5**

2.1 The Lieb-Liniger model: N bosons in a pot 5

2.2 Effective field theories 9

  2.2.1 Tomonaga-Luttinger liquid model 9

  2.2.2 Sine-Gordon model 12

  2.2.3 Klein-Gordon model 15

3 Experimental setup and observables **17**

3.1 Introducing the "KRb" setup 18

  3.1.1 Overview 18

  3.1.2 Experimental cycle 20

3.2 Probing via absorption imaging 21

  3.2.1 Time of flight expansion 22

  3.2.2 Absorption imaging: quantifying shadows 23

3.3 Experimental observables 27

  3.3.1 A single condensate 27

  3.3.2 Coupled condensates 28

4 Arbitrary one-dimensional potentials on an atom chip **31**

4.1 Static magnetic potentials 32

  4.1.1 Quadrupole traps 33

  4.1.2 Ioffe-Pritchard traps 34

4.2 Radio frequency dressed potentials 35

4.3 Optical dipole potentials 35

  4.3.1 Arbitrary optical dipole potentials via beamshaping 36

  4.3.2 Optical setup 37

4.3.3 Calibration . . . 40
4.3.4 Closed-loop pattern optimization . . . 41
4.3.5 Examples . . . 45
4.4 Outlook . . . 48

5 Verification of the area law of mutual information 49
5.1 Quantum information measures in many-body systems . . . 49
5.2 Von Neumann entropy and mutual information . . . 50
5.2.1 Von Neumann entropy . . . 51
5.2.2 Quantum mutual information . . . 54
5.3 Quantum information measures for Gaussian states . . . 55
5.3.1 Von Neumann entropy and quantum mutual information . . . 56
5.4 Theoretical model . . . 57
5.4.1 Klein-Gordon Hamiltonian with homogeneous background density 57
5.4.2 Thermal equilibrium states of the Klein-Gordon Hamiltonian . . 58
5.5 Experimental protocol and tomography process . . . 58
5.5.1 Initial states . . . 59
5.5.2 Mass quench . . . 60
5.5.3 Tomography process: Post-quench quantum read-out . . . 60
5.6 Experimental results . . . 65
5.6.1 Tomography results . . . 65
5.6.2 Von Neumann entropy and mutual information . . . 69
5.7 Outlook . . . 73

6 Observation of curved light-cones 75
6.1 Quantum field simulation on a curved background . . . 75
6.2 Experimental protocol and quantification of velocity field correlations . 76
6.2.1 Initial states . . . 76
6.2.2 Mass quench . . . 77
6.2.3 Observable . . . 77
6.3 Experimental results . . . 79
6.3.1 Second order correlations of the velocity field . . . 79
6.3.2 Correlation front velocity . . . 83
6.4 Theoretical description . . . 84
6.4.1 From action to Hamiltonian . . . 85
6.4.2 Heisenberg equations of motion . . . 88
6.4.3 Correlation fronts propagation . . . 91

6.4.4 The effect of space-dependent Luttinger parameter 97
6.5 Outlook 99

7 Final words **103**

Appendix A Cosine transformations **105**
A.1 Dimensional analysis 108
A.2 Discrete cosine transform 109

References **113**

Curriculum Vitae **123**

Chapter 1

Introduction

Ultra-cold atoms

The experimental realization of Bose-Einstein condensates in 1995 [1, 2] was undoubtedly a profound event in the modern history of science. A seventy years old idea by Albert Einstein and Satyendranath Bose [3–5], which sounded like a dream, finally came true. Although many scientists would consider this discovery the end of a quest, most people would agree that it marks the beginning of an era. Not only has this state of matter proven to be a valuable platform to explore the fundamentals of many-body physics, but all the technological advances that paved the way to realizing it have an enormous impact on atomic, solid state, and other similar fields.

Ultra-cold atoms on an atom chip

In the past two decades, cold or ultra-cold atomic systems have been used for various purposes, from fundamental questions like many-body problems [6], quantum simulation [7], and quantum information [8, 9] to applications like quantum sensing and gravimetry [10]. Our experiment in Vienna studies one-dimensional (1D) ultra-cold Bose gases cooled and trapped on an atom chip device. We can utilize different trapping geometries to realize a pair of parallel tunneling-coupled condensates and probe the system via matter-wave interferometry [11]. The experiment was designed to answer fundamental questions in 1D many-body physics. Questions like: "Does such a system thermalize?" [12–14], "How well do the theoretical descriptions match the experiment?" [15, 16], "Testing integrable models" [17, 18]. Although 1D sounds boring, even questions like "why this system is so 1D?" were unanswered until 2020 [18]. During our studies, one of the impressive connections established between theory and experiment is the experimental verification [15–17, 19] of effective field theoretical description of tunneling-coupled 1D Bose gasses [20, 21]. These effective models [22] play a vital role in our understanding of many-body quantum systems: Instead of describing 10000 particles with their microscopic degrees of freedom, which is a nightmare, these theories give insight into relevant collective excitations of the many-body system. Indeed such descriptions come with a price: They are only valid in a certain energy range. In our experiment, we are mainly interested in the low-energy excitations described by a non-interacting massive field theory, namely the Klein-Gordon theory, or an interactive field theory such as the sine-Gordon model [23].

Ultra-cold atoms on an atom chip used for analog quantum simulation

While waiting for a full-functioning quantum computer, analog quantum simulation is a practical approach to exploring complex quantum systems by mimicking their behavior in a controllable and well-understood physical system [7, 24]. In this paradigm, the experimental system, often called *the quantum simulator*, is engineered to emulate the dynamics of a target quantum model of interest. The idea of analog quantum simulation stems from the realization that specific quantum systems, such as those exhibiting many-body interactions or strong correlations, are exceedingly challenging to solve using classical computational methods. These systems play a crucial role in understanding fundamental phenomena in condensed matter physics, high-energy physics, quantum chemistry, and gravity [9, 25–32].

Our recent investigations mentioned above qualify our experimental system as a *quantum field simulator*, a platform to explore quantum field theory models beyond our current theoretical understanding. Our setup is *tuneable* and *readable*: We have developed trapping techniques that modify key parameters of the theory, as we will discuss in this thesis. Also, we have direct and indirect access to different degrees of freedom, enabling us to measure essential observables of the theory.

This thesis focuses on simulating the Klein-Gordon Hamiltonian by realizing strongly tunneling-coupled parallel 1D Bose gases.

How to read this manuscript?

Which personal pronoun where?

Some authors like "we"; others say it's my work, so "I". The other group avoids the dilemma by writing the whole manuscript in a passive voice. I will use all three! For the most part, I will be using "we"; depending on the context, it either refers to "the

Die approbierte gedruckte Originalversion dieser Dissertation ist an der TU Wien Bibliothek verfügbar.
The approved original version of this doctoral thesis is available in print at TU Wien Bibliothek.
TU Bibliothek Your knowledge hub WIEN

author and readership" as going through the derivation of equations together or to "the author and labmates/collaborators". The first-person pronoun will directly address my intentions, ideas, or contributions.

Where to find more?

The results presented in this thesis are a sequel to a long and deep experimental and theoretical exploration carried out by our team members and collaborators from all over the globe. I tried to write a coherent story about my projects using all the necessary ingredients to understand every next step. I also tried to minimize paraphrasing of the irrelevant material already thoroughly discussed in previous works. Instead, whenever necessary, I tried to mention precisely the reference(s) that contain complementary information on that topic, pointing out the relevant section of the given reference. Different aspects of the experimental setup or theoretical tools related to our experiment are explained in the theses written by former students in our group [13, 14, 33–41] or collaborating groups [42, 43]

More about the structure

The second chapter of this thesis introduces the effective field theories that our experimental system can simulate. I will start from a general Hamiltonian in three dimensions and work out the approximations and assumptions necessary to get the Klein-Gordon model.

In chapter 3, I will briefly overview the experimental setup. The chapter will focus on the imaging systems used for absorption imaging. In the last part of the chapter, I will go through the crucial experimental observables.

The fourth chapter explains how our experimental setup combines magnetic and optical dipole potentials. In the first stage of my doctoral studies, I implemented the optical dipole trap setup built during my Master's project [37] in the experiment. This setup was one of the major upgrades to the apparatus, enabling arbitrary one-dimensional trapping in our system.

In chapter 5, I will discuss the quantification of information in equilibrium states through post-quench tomography. In this chapter, I will explain how we measure von Neumann entropy and mutual information and demonstrate the area law of mutual information. The chapter contains the results presented in our paper [44] but with a more pedagogical introduction to quantum information measures. Also, the time evolution under a free massless theory is discussed in detail. The raw data for the results presented here are uploaded on a public server along with codes to analyze absorption images. [45].

Chapter 6 is about information propagation. There, I will show how the trapping geometry can simulate an inhomogeneous metric by modulating the speed of sound in the condensates. The chapter presents the results published in our paper [46], but a few details like the differences between homogeneous and inhomogeneous Tomonaga-Luttinger liquid models are discussed more clearly. The phase profiles for the results presented here can be found in reference [47].

Lastly, chapter 7 presents only a couple of ideas in other directions based on what we have learned so far. There is an Outlook section at the end of each chapter, discussing possible future directions related to the research presented in that chapter.

Structure of references

Before we start, let's go through the frequently used references first.

Thomas Schweigler's PhD thesis [39] (Schweigler-Thesis). I will refer to this invaluable manuscript a lot. Thomas, a former Ph.D. candidate and post-doc in our group, explains many useful theoretical and experimental results in his thesis. I will mainly refer to the discussions and results regarding the sine-Gordon model. There are specific experimental details, like simulating and characterizing the imaging systems, that he has done rigorously.

Bernhard Rauer's PhD thesis [38] (Rauer-Thesis). Bernhard, a former Ph.D. candidate and post-doc in our group, worked on quenches similar to what we are interested in here. His thesis contains nice discussions on the Lieb-Liniger model, Tomonaga-Luttinger liquid, and, generally, the dynamics of superfluids after a quench. Bernhard's thesis is one of the best sources to understand the radio-frequency dressed traps needed to realize a double-well potential for cold atoms on atom chips. In the chapter, I will refer to his thesis introducing the experimental setup, especially magnetic trapping and evaporative cooling.

My master's thesis [37] (Tajik-Thesis). My master's thesis extensively explains our implementation of optical dipole traps in the experimental setup. Details about beam preparation and alignment are presented there that can't be found elsewhere.

Chapter 2

Effective field theories describing cold bosons

From Lieb-Liniger to Klein-Gordon model

In this chapter, I will show the link between the microscopic description of quasi-one-dimensional quasi-condensates to the effective description offered by quantum field theoretical models. In section 2.1, I will start from a general Hamiltonian for N interacting bosons in 3D and make the proper assumptions and approximations to get to the famous Lieb-Liniger model. The rest of the chapter is an introduction to three important effective models, namely *Tomonaga-Luttinger liquid*, *sine-Gordon*, and *Klein-Gordon* model. This chapter serves as a general introduction to the theoretical models that our experiment can simulate. In chapters 5 and 6, further related theoretical details are discussed.

I assumed the reader is familiar with concepts of graduate-level quantum mechanics, such as second quantization and density matrix formalism. Needless to mention that the same level of math is required to follow the rest of the manuscript.

2.1 The Lieb-Liniger model: N bosons in a pot

From three dimensions to only one

We start by writing the most general Hamiltonian in 1+3 dimensions (one time and three spatial dimensions) for N interacting bosons confined in an external potential $U(\vec{r})$. For a dilute gas of bosons, we only take two-body interactions through the potential U_{int} into account and write the Hamiltonian as

$$\hat{H} = \sum_{i}^{N}\left[-\frac{\hbar^2}{2m}\nabla_i^2 + U\left(\vec{r}_i\right)\right] + \sum_{i<j}^{N} U_{\text{int}}\left(\vec{r}_i - \vec{r}_j\right) \ , \tag{2.1}$$

where m is the mass of a single particle, $\vec{r}_i$ is the position of the i'th particle, and $\hbar = h/2\pi = 1.05 \times 10^{-34}\,\text{J s}$ is the reduced Planck constant. Note that this Hamiltonian acts on a many-body wave function $\psi(\vec{r}_i)$ in the first quantization.

We now apply a few experimental considerations that will be discussed in section 4.1 to describe our quasi-one-dimensional (quasi-1D) Bose gas. First we write the external trapping potential as $U_{\text{ext}}\left(\vec{r}_i\right) = U(z_i) + U_{\perp}(x_i, y_i)$. Our transverse trapping potential, $U_{\perp}(x_i, y_i)$, is typically much stronger than the longitudinal (axial) potential $U(z_i)$. It is instructive first to consider the case where $U(z) = 0$ except on the boundaries $(z = 0,\ z = L)$ where it has infinite walls. A good approximation for the transverse magnetic trap produced by our atom chip is a harmonic potential with angular frequency $\omega_{\perp} \approx 2\pi \times 2\,\text{kHz}$. In our system, sufficiently strong transverse potential compared to other energy scales, including temperature and chemical potential, restricts the system's dynamics to one dimension. We recently showed that due to the fermionic nature of weakly interacting bosons, Pauli blocking prohibits the dynamic of the gas in the transverse direction, enhancing the 1D properties of our system [18].

Second, we write the interaction potential as $U_{\text{int}}(z) = g_{1\text{D}}\delta(z)$, with

$$g_{1\text{D}} = \hbar\omega_{\perp} a_{\text{s}} \frac{2 + 3a_{\text{s}} n_{1\text{D}}}{(1 + 2a_{\text{s}} n_{1\text{D}})} \ , \tag{2.2}$$

where a_{s} is the three-dimensional s-wave scattering length (5.8 nm for ^{87}Rb atoms) and $n_{1\text{D}} = N/L$ is the linear atomic density[1]. This approximation is valid in our experiment because the thermal de Broglie wavelength of the atomic gas,

$$\lambda_{dB} = \sqrt{\frac{2\pi\hbar^2}{mk_BT}} \ , \tag{2.3}$$

is much larger than the effective extension of the interaction potential.

Inserting the two potentials in eq. (2.1), we obtain the so-called *Lieb-Liniger Hamiltonian* [48, 49]

$$\hat{H} = -\sum_{i}^{N}\frac{\hbar^2}{2m}\frac{\partial^2}{\partial z_i^2} + g_{1\text{D}}\sum_{i<j}^{N}\delta\left(z_i - z_j\right) \ , \tag{2.4}$$

---

[1] Read **Schweigler-Thesis** section 2.3 for a derivation of eq. (2.2).

describing a gas of ultra-cold bosons confined in a 1D box-like geometry. Lieb-Liniger Hamiltonian is a simple model whose thermal equilibrium states exhibit a rich phase diagram as presented in fig. 2.1. In the figure, γ is the Lieb-Liniger parameter, which is a dimensionless interaction strength given by the ratio of the mean inter-particle distance, $n_{1\mathrm{D}}^{-1}$ and the intrinsic length scale $l_{\mathrm{int}} = \hbar^2/(m g_{1\mathrm{D}})$,

$$\gamma = \frac{n_{1\mathrm{D}}^{-1}}{l_{\mathrm{int}}} = \frac{m g_{1\mathrm{D}}}{\hbar^2 n_{1\mathrm{D}}} . \tag{2.5}$$

In the limit where $\gamma \gg 1$, the system's energy is primarily governed by particle interactions. The bosons experience strong repulsion in this regime, leading them to behave like free fermions. This limit is commonly called the *Tonks-Girardeau* regime [50]. On the other hand, when $\gamma \ll 1$, the interactions between bosons are relatively weak. In this regime, a significant portion of the bosons tends to occupy the zero momentum state, forming a quasi-condensate in 1D.

In fig. 2.1, t is a dimensionless temperature defined as the ratio between the thermal energy, $k_{\mathrm{B}}T$, and an intrinsic interaction energy, $E_{\mathrm{int}} = m g_{1\mathrm{D}}^2/(2\hbar)$,

$$t = \frac{k_{\mathrm{B}}T}{E_{\mathrm{int}}} = \frac{2\hbar k_{\mathrm{B}}T}{m g_{1\mathrm{D}}^2} . \tag{2.6}$$

Section 2.1 in **Rauer-Thesis** comprehensively explains the regimes introduced in fig. 2.1. The experiments presented in this thesis would cover a small part of the phase space marked with "Exp." in the figure. The parameters are typically $1.1 \times 10^{-3} < \gamma < 4.7 \times 10^{-3}$ and $2 \times 10^2 < t < 2.4 \times 10^3$, placing us in the quasi-condensate regime dominated by thermal fluctuations.

Second quantization

The Lieb-Liniger Hamiltonian introduced in eq. (2.4), in second quantization form, is given by

$$\hat{H} = \int \mathrm{d}z\, \hat{\psi}^\dagger(z) \left[-\frac{\hbar^2}{2m}\partial_z^2 + \frac{g_{1\mathrm{D}}}{2}\hat{\psi}^\dagger(z)\hat{\psi}(z) \right] \hat{\psi}(z) . \tag{2.7}$$

Here, the bosonic fields $\hat{\psi}^\dagger(z)$ and $\hat{\psi}(z)$ create/annihilate a boson at position z, fullfiling a bosonic commutation relation $\left[\hat{\psi}^\dagger(z), \hat{\psi}(z')\right] = \mathrm{i}\delta(z - z')$. The operator $\hat{\rho}(z) = \hat{\psi}^\dagger(z)\hat{\psi}(z)$ gives the linear particle density. Note that we will write all our equations in SI units. Adding a chemical potential term μ in grand canonical representation to set

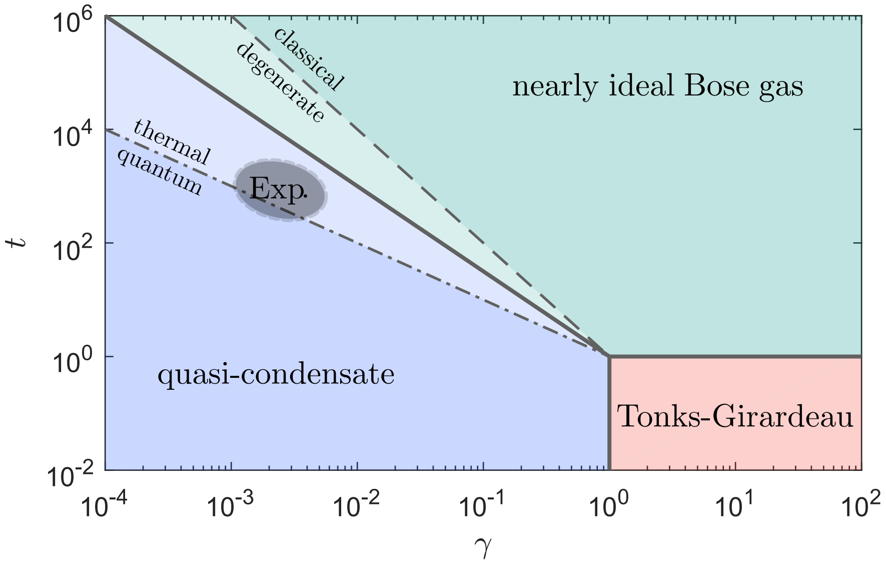

Figure 2.1 Phase diagram of the Lieb-Liniger model. The Tonks-Girardeau regime is represented by the red region ($\gamma \gg 1, t \ll 1$), the nearly ideal Bose gas is shown in green ($t\gamma^{3/2} > 1, t \gg 1$), and the quasi-condensate regime is depicted in blue ($t\gamma^{3/2} < 1, \gamma \ll 1$). The degeneracy transition is marked by the dashed line ($t\gamma^2 = 1$), while the thermal-quantum boundary is indicated by the dash-dotted line ($t\gamma = 1$) for the fluctuations in the quasi-condensate regime. All boundaries between phases are smooth crossovers, not sharp transitions. The gray-shaded ellipse denotes the parameter regime of the measurements discussed in this thesis. Figure adapted with permission from **Rauer-Thesis**.

Die approbierte gedruckte Originalversion dieser Dissertation ist an der TU Wien Bibliothek verfügbar.
The approved original version of this doctoral thesis is available in print at TU Wien Bibliothek.
TU Bibliothek, Your knowledge hub, WIEN

an average boson number N, and restoring the external potential $U(z)$, we obtain

$$\hat{H} = \int \mathrm{d}z\, \hat{\psi}^\dagger(z) \left[-\frac{\hbar^2}{2m}\partial_z^2 + U(z) - \mu + \frac{g_{1\mathrm{D}}}{2}\hat{\psi}^\dagger(z)\hat{\psi}(z) \right] \hat{\psi}(z)\ . \tag{2.8}$$

This Hamiltonian is our starting point. Following our discussions in the previous section, we will apply low-energy approximations to derive effective theories describing our experimental system in the quasi-condensate regime. As we mentioned earlier, the Lieb-Liniger Hamiltonian is an integrable model and exactly solvable. Nevertheless, effective models are generally more insightful as they describe different physical systems in various fields of physics, from cosmology to solid-state physics. Also, effective theories are more convenient for calculating the dynamics.

2.2 Effective field theories

In this section, we will first show how low-energy treatment of Hamiltonian in eq. (2.8) leads to a free massless quadratic Hamiltonian called the *Tomonaga-Luttinger liquid* (TLL) model for a single condensate. We then continue by including an interaction term to describe the coupling between a pair of parallel quasi-condensates in different coupling regimes. Doing this, we will come across two important models, namely the *sine-Gordon* (SG) Hamiltonian and then the *Klein-Gordon* (KG) Hamiltonian. The latter is of the utmost importance for this work's forthcoming results.

2.2.1 Tomonaga-Luttinger liquid model

In this section, we follow Mora and Castin [20] to work out a Bogoliubov theory for the quasi-condensate regime. As they thoroughly discuss in section I.A. of [20], in continium, the atom number fluctuations, $\langle\hat{\rho}(z)^2\rangle - \langle\hat{\rho}(z)\rangle^2$, diverge. The $\delta(z)$ function stemming from bosonic commutation relations in $\langle\hat{\rho}(z)^2\rangle = \delta(0)\hat{\rho}(z) + \langle\psi^\dagger(z)\psi^\dagger(z)\psi(z)\psi(z)\rangle$ is responsible for the ill behavior.

To overcome this obstacle, they discretize the space. In 1D, we consider a grid $\{z_i\}$ with $i = 1, 2, \ldots, N_{\mathrm{grid}}$ and grid spacing $\Delta z = z_{i+1} - z_i$. This grid spacing has to be smaller than other characteristic lengths of the system, including the healing length,

$$\xi = \frac{\hbar}{\sqrt{m\mu}}\ , \tag{2.9}$$

and the thermal de Broglie wavelength, λ_{dB} in eq. (2.3). See section I.C. of [20] for more details. Replacing the differential operators in eq. (2.8) with finite differences, we obtain

$$\hat{H} = \sum_{i=1}^{N_{\mathrm{grid}}} \Delta z \, \hat{\psi}^{\dagger}(z_i) \left[-\frac{\hbar^2}{2m}\Delta + U(z_i) - \mu + \frac{g_{1\mathrm{D}}}{2}\hat{\psi}^{\dagger}(z_i)\hat{\psi}(z_i) \right] \hat{\psi}(z_i) \, , \tag{2.10}$$

with

$$\Delta f(z_i) = \frac{f(z_{i+1}) - 2f(z_i) + f(z_{i-1})}{\Delta z^2}, \quad \nabla f(z_i) = \frac{f(z_{i+1}) - f(z_{i-1})}{2\Delta z} \, . \tag{2.11}$$

The bosonic operators $\hat{\psi}^{\dagger}(z_i)$ and $\hat{\psi}(z_i)$, now create/annihilate a particle in a box of size Δz at the position z_i. Their commutation relation is, therefore

$$\left[\hat{\psi}(z_i), \hat{\psi}^{\dagger}(z_j)\right] = \frac{\delta_{ij}}{\Delta z}, \tag{2.12}$$

where δ_{ij} is the Kronecker delta and is dimensionless. Note that the dimension of the Dirac delta function, $\delta(z)$, is one over length because $\int_{-\infty}^{\infty} dz\delta(z) = 1$ is dimensionless. The Hermitian operator

$$\Delta z \, \hat{\psi}^{\dagger}(z_i)\hat{\psi}(z_i) = \Delta z \, \hat{\rho}(z_i) \tag{2.13}$$

gives the total atom number in a box of length Δz at the position z_i. Introducing a Hermitian phase operator $\hat{\theta}(z_i)$, we can write $\hat{\psi}$ as

$$\hat{\psi}(z_i) \approx e^{\mathrm{i}\hat{\theta}(z_i)} \sqrt{\hat{\rho}(z_i)} \, . \tag{2.14}$$

Note that the approximate equality sign indicates that the operator $\exp\left(\mathrm{i}\hat{\theta}(z_i)\right)$ is only approximately unitary. See [20, 51] for more details. Also, note that the phase of a single condensate is not a physical observable. Here, $\hat{\theta}(z_i)$ and $\hat{\rho}(z_i)$ are the Hermitian phase and density operators respectively. The phase and density operators follow the canonical commutation relations

$$\left[\hat{\rho}(z_i), \hat{\theta}(z_j)\right] \approx \frac{\mathrm{i}\delta_{ij}}{\Delta z}, \quad [\hat{\rho}(z_i), \hat{\rho}(z_j))] = 0, \quad \left[\hat{\theta}(z_i), \hat{\theta}(z_j)\right] = 0 \tag{2.15}$$

The next step is to split the density operator $\hat{\rho}$ into a background density ρ_0 (not an operator anymore) and density fluctuations $\delta\hat{\rho}$ on top of this background. We write

$$\hat{\rho}(z_i) = \rho_0(z_i) + \delta\hat{\rho}(z_i) \, , \tag{2.16}$$

Die approbierte gedruckte Originalversion dieser Dissertation ist an der TU Wien Bibliothek verfügbar.
The approved original version of this doctoral thesis is available in print at TU Wien Bibliothek.
TU Bibliothek WIEN Your knowledge hub

so that the operator $\delta\hat{\rho}$ obeys the same commutation relations (2.15) as $\hat{\rho}$. We know insert eqs. (2.14) and (2.16) in the discrete Hamiltonian (2.10) and expand it in orders of

$$\frac{|\delta\hat{\rho}|}{\rho_0} \ll 1 \quad \text{and} \quad |\Delta z \nabla \hat{\theta}| \leqslant 1 \,, \tag{2.17}$$

we obtain $\hat{H} = \hat{H}^{(0)} + \hat{H}^{(1)} + \hat{H}^{(2)} + \cdots$. Conditions (2.17) assume that the density fluctuations are much smaller than the background density. Also, the change of the phase (the phase gradient) is very small across one single box of length Δz. We further consider both parameters to be of the same order.

After expansion, the zeroth order only depends on the background density $\rho_0(z_i)$. By minimizing $\hat{H}^{(0)}$ with respect to $\rho_0(z_i)$, we achieve a Gross-Pitaevskii equation for $\sqrt{\rho_0(z_i)}$

$$\left[-\frac{\hbar^2}{2m}\Delta + U(z_i) - \mu + g_{1\mathrm{D}}\,\rho_0(z_i)\right]\sqrt{\rho_0(z_i)} = 0. \tag{2.18}$$

If $\rho_0(z_i)$ fullfils this equation, $\hat{H}^{(1)}$ will be zero. For the second order, we obtain

$$\begin{aligned}\hat{H}^{(2)} = \sum_{i=1}^{N_{\mathrm{grid}}} \Delta z \Bigg\{ & -\frac{\hbar^2}{2m}\frac{\delta\hat{\rho}(z_i)}{2\sqrt{\rho_0(z_i)}}\Delta\left(\frac{\delta\hat{\rho}(z_i)}{2\sqrt{\rho_0(z_i)}}\right) + \frac{\hbar^2\delta\hat{\rho}^2(z_i)}{8m\sqrt{\rho_0^3(z_i)}}\Delta\sqrt{\rho_0(z_i)} \\ & + \frac{g_{1\mathrm{D}}}{2}\delta\hat{\rho}^2(z_i) + \frac{\hbar^2}{2m}\sqrt{\rho_0(z_i)\rho_0(z_{i+1})}\,\frac{\left[\hat{\theta}(z_{i+1}) - \hat{\theta}(z_i)\right]^2}{\Delta z^2}\Bigg\} \,.\end{aligned} \tag{2.19}$$

We have disregarded the contribution of a complex number since it has no impact on the dynamics of the fields.

Two further approximations are necessary to obtain the sought-after Tomonaga-Luttinger liquid model: First approximation is the so-called Thomas-Fermi approximation. We assume that the background density is changing very slowly, hence $\Delta\rho_0(z_i) = 0$ in both (2.18) and (2.19). The second approximation neglects the so-called quantum pressure - the first term in 2.19 - by assuming that the density fluctuations have a short wavelength. The two remaining expressions form the Tomonaga-Luttinger liquid Hamiltonian

$$\hat{H}_{\mathrm{TLL}} = \sum_z \Delta z \left\{ \frac{g_{1\mathrm{D}}}{2}\delta\hat{\rho}^2(z_i) + \frac{\hbar^2}{2m}\sqrt{\rho_0(z_i)\rho_0(z_{i+1})}\,\frac{\left[\hat{\theta}(z_{i+1}) - \hat{\theta}(z_i)\right]^2}{\Delta z^2} \right\} \,. \tag{2.20}$$

In the rest of the manuscript, it is often more convenient to work with the continuous form of this Hamiltonian ($\lim \Delta z \to 0$)

$$\hat{H}_{\mathrm{TLL}} = \int \mathrm{d}z \left[\frac{g_{1\mathrm{D}}}{2} \delta\hat{\rho}^2(z) + \frac{\hbar^2}{2m} \rho_0(z) \left(\frac{\partial \hat{\theta}(z)}{\partial z} \right)^2 \right] . \tag{2.21}$$

Note that in this effective description, the trapping potential, $U(z)$, and the chemical potential, μ are absorbed in the background density $\rho_0(z)$ through eq. (2.18). We should keep in mind that the 3D nature of the condensate, which is determined by the transverse trapping frequency $\omega_\perp$ and the three-dimensional scattering length a_s, is hidden in $g_{1\mathrm{D}}$ given by eq. (2.2).

2.2.2 Sine-Gordon model

In the previous section, we derived the low-energy effective field theory for a single quasi-condensate described by two conjugate fields $\hat{\rho}$ and $\hat{\theta}$. We will extend that discussion to a pair of parallel tunneling-coupled quasi-condensates. This setting is of immense importance for the forthcoming experiments discussed in this thesis. We write the bosonic fields as

$$\hat{\psi}_j(z) \approx e^{\mathrm{i}\hat{\theta}_j(z)} \sqrt{\rho_0(z) + \delta\hat{\rho}_j(z)} \, . \tag{2.22}$$

where $j = 1, 2$ labels each condensate. We assume that the 1D potential landscape, $U(z)$, and the atom numbers of the two condensates are identical. This leads to identical chemical potentials and, consecutively, identical background densities, $\rho_0(z)$.

The Hamiltonian for the combined system can be written as the sum of two independent Hamiltonians for each condensate, $\hat{H}_1$ and $\hat{H}_2$, plus a tunneling part $\hat{H}_\mathrm{T}$ as

$$\hat{H} = \hat{H}_1 + \hat{H}_2 + \hat{H}_\mathrm{T} \, . \tag{2.23}$$

The independent Hamiltonians are the Lieb-Liniger model (2.8),

$$\hat{H}_j = \int \mathrm{d}z \, \hat{\psi}_j^\dagger(z) \left[-\frac{\hbar^2}{2m} \partial_z^2 + U(z) - \mu + \frac{g_{1\mathrm{D}}}{2} \hat{\psi}_j^\dagger(z) \hat{\psi}_j(z) \right] \hat{\psi}_j(z) \, , \quad j = 1, 2 \, . \tag{2.24}$$

For tunneling, we choose a linear term [52],

$$\hat{H}_\mathrm{T} = -\hbar J \int dz \left[\hat{\psi}_1^\dagger(z) \hat{\psi}_2(z) + \hat{\psi}_2^\dagger(z) \hat{\psi}_1(z) \right] \, , \tag{2.25}$$

where J is the single particle tunneling rate and sets the strength of the coupling. The first term of $\hat{H}_T$ corresponds to particle annihilation in well 2 at position z and then particle creation in well 1 at the same position, and the second term describes tunneling from well 1 to well 2.

We are again interested in the low-energy description where the fluctuations are small. We first consider the case where tunneling is zero and then add the tunneling term.

Vanishing tunnelling

Assuming two independent condensates, the tunneling term vanishes - for example, by setting $J = 0$. Following the same process as in section 2.2.1, we obtain the sum of two independent TLL Hamiltonians,

$$\begin{aligned}\hat{H}_{\mathrm{TLL}} = &\int \mathrm{d}z \left[\frac{g_{\mathrm{1D}}}{2}\delta\hat{\rho}_1{}^2(z) + \frac{\hbar^2}{2m}\rho_0(z)\left(\frac{\partial\hat{\theta}_1(z)}{\partial z}\right)^2\right] \\ &+ \int \mathrm{d}z \left[\frac{g_{\mathrm{1D}}}{2}\delta\hat{\rho}_2{}^2(z) + \frac{\hbar^2}{2m}\rho_0(z)\left(\frac{\partial\hat{\theta}_2(z)}{\partial z}\right)^2\right] .\end{aligned} \tag{2.26}$$

Note that our system is described by four fields: Two phase fields $\hat{\theta}_1$ and $\hat{\theta}_2$, and two density fluctuation fields $\hat{\delta}\rho_1$ and $\hat{\delta}\rho_2$. As mentioned in section 2.2.1, the absolute phase of a condensate is not a physical observable. However, the difference between the two phases can be interferometrically measured and indeed is *the main experimental observable* for the projects discussed in this thesis. This motivation leads to constructing four fields based on the pair of fields associated with each condensate. We define the so-called *common* or *symmetric* fields (or degrees of freedom) as

$$\delta\hat{\rho}_+(z) = \frac{1}{2}\left[\delta\hat{\rho}_1(z) + \delta\hat{\rho}_2(z)\right], \quad \hat{\varphi}_+(z) = \hat{\theta}_1(z) + \hat{\theta}_2(z) , \tag{2.27}$$

and the *relative* or *assymmetric* fields (or degrees of freedom) as

$$\delta\hat{\rho}_-(z) = \frac{1}{2}\left[\delta\hat{\rho}_1(z) - \delta\hat{\rho}_2(z)\right], \quad \hat{\varphi}_-(z) = \hat{\theta}_1(z) - \hat{\theta}_2(z) . \tag{2.28}$$

The canonical commutation relations have the familiar form

$$\begin{aligned}
&[\delta\hat{\rho}_+(z),\hat{\varphi}_+(z')] = [\delta\hat{\rho}_-(z),\hat{\varphi}_-(z')] = [\delta\hat{\rho}_1(z),\hat{\varphi}_1(z')] = [\delta\hat{\rho}_2(z),\hat{\varphi}_2(z')] = \mathrm{i}\delta(z-z') \\
&[\delta\hat{\rho}_+(z),\hat{\varphi}_-(z')] = [\delta\hat{\rho}_-(z),\hat{\varphi}_+(z')] = [\delta\hat{\rho}_1(z),\hat{\varphi}_2(z')] = [\delta\hat{\rho}_2(z),\hat{\varphi}_1(z')] = 0. \qquad (2.29)
\end{aligned}$$

From chapter 5 onward, I will denote the relative degrees of freedom without a subscript minus sign, meaning $\hat{\varphi} \equiv \hat{\varphi}_-$ and $\delta\hat{\rho} \equiv \delta\hat{\rho}_-$.

Now we rewrite eq. (2.26) by inserting the definitions for common and relative degrees of freedom as

$$\begin{aligned}
\hat{H}_{\mathrm{TLL}} = &\int \mathrm{d}z \left[g_{1\mathrm{D}} \delta\hat{\rho_+}^2(z) + \frac{\hbar^2}{4m}\rho_0(z)\left(\frac{\partial\hat{\varphi}_+(z)}{\partial z}\right)^2 \right] \\
&+ \int \mathrm{d}z \left[g_{1\mathrm{D}} \delta\hat{\rho_-}^2(z) + \frac{\hbar^2}{4m}\rho_0(z)\left(\frac{\partial\hat{\varphi}_-(z)}{\partial z}\right)^2 \right] . \qquad (2.30)
\end{aligned}$$

Note that the Hamiltonian breaks down into two separate parts,

$$\hat{H} = \hat{H}_1 + \hat{H}_2 = \hat{H}_+ + \hat{H}_- \ , \qquad (2.31)$$

where the common and relative fields do not mix, meaning that the dynamics of these two sections are independent of each other. Also, we assumed a symmetric double-well with the same number of atoms and trapping potential to obtain this independent form. The case where the density profiles are not identical is discussed in [35].

Finite tunneling

To derive the low-energy description for the tunneling term, we neglect the density fluctuations and write the bosonic fields in each well as

$$\hat{\psi}_j(z) \approx e^{\mathrm{i}\hat{\theta}_j(z)}\sqrt{\rho_0(z)}\,, \quad j = 1,2\ . \qquad (2.32)$$

Inserting these fields in eq. (2.25) yields

$$\hat{H}_{\mathrm{T}} = -2\hbar J \int dz \rho_0(z) \cos\left(\hat{\varphi}_-(z)\right) \ . \qquad (2.33)$$

This particular choice guarantees that the relative and common fields do not mix and density fluctuations do not play a role in the coupling. Although this assumption is very restrictive, the approximation turns out to be sufficient to explain most of our experiments.

As the tunneling term only contains the relative phase field, the common degrees of freedom dynamics are governed by the same quadratic Hamiltonian as in the uncoupled case, namely $\hat{H}_+$. The relative degrees of freedom are now described by the sum of the TLL Hamiltonian plus the tunneling term, known as the *sine-Gordon* (SG) model [21]:

$$\hat{H}_{\mathrm{SG}} = \int \mathrm{d}z \left[g_{\mathrm{1D}}\, \delta\hat{\rho}_-^2(z) + \frac{\hbar^2 \rho_0(z)}{4m} \left(\frac{\partial \hat{\varphi}_-(z)}{\partial z} \right)^2 - 2\hbar J \rho_0(z) \cos\left(\hat{\varphi}_-(z)\right) \right] . \tag{2.34}$$

The thermal equilibrium state of this Hamiltonian is the main focus of Thomas Schweigler's research [39]. The SG model's theoretical and experimental aspects are investigated in several works in our group [15, 16, 53].

The validity of eq. (2.34) as an approximation for eq. (2.23) is discussed in section 2.5 of **Schweigler-Thesis** and [53].

2.2.3 Klein-Gordon model

For tunneling-coupled quasi-condensates with dominating thermal fluctuations, the dimensionless ratio

$$q = \frac{\lambda_T}{\ell_J} \tag{2.35}$$

is directly related to the so-called *coherence factor*, $\Big\langle \cos\Big(\hat{\phi}_-(z)\Big)\Big\rangle$, and parametrizes the importance of non-linear contributions in eq. (2.34). Here,

$$\lambda_T(z) = \frac{2\hbar^2 \rho_0(z)}{m k_B T} \tag{2.36}$$

is the thermal phase coherence length and

$$\ell_J = \sqrt{\frac{\hbar}{4mJ}} \, , \tag{2.37}$$

is the healing length of the phase (or the correlation length).

For the interest of the works in this thesis, we focus on the strongly coupled condensates, where the single-particle tunneling rate, J, is large enough to make the phase fluctuations comparable with other small quantities (2.17) [52], corresponding to $q > 2$.

Assuming that the relative phase $\hat{\varphi}_-(z)$ is small, we expand $\cos(\hat{\varphi}_-(z))$ and take the first two terms, $1 - \hat{\varphi}_-^2(z)/2$, we obtain

$$\hat{H}_{\mathrm{KG}} = \int \mathrm{d}z \left[g_{1\mathrm{D}}\, \delta\hat{\rho}_-^2(z) + \frac{\hbar^2 \rho_0(z)}{4m} \left(\frac{\partial \hat{\varphi}_-(z)}{\partial z} \right)^2 + \hbar J \rho_0(z) \hat{\varphi}_-^2(z) \right] . \tag{2.38}$$

Note that the first term in the expansion is only a constant that rescales the chemical potential. The TLL model describes the common degrees of freedom as before.

Die approbierte gedruckte Originalversion dieser Dissertation ist an der TU Wien Bibliothek verfügbar.
The approved original version of this doctoral thesis is available in print at TU Wien Bibliothek.
TU Bibliothek WIEN Your knowledge hub

Chapter 3

Experimental setup and observables

Creating and probing ultra-cold Bose gases on an atom chip

In this chapter, I will briefly introduce our experimental setup, the physical system, and the main observables. I will start by briefly explaining the physical system under investigation and the experimental setup in section 3.1.1. A typical experimental cycle is then introduced in section 3.1.2. In the second section, I will go through the observables we can directly measure by looking at the atomic densities obtained by absorption imaging.

Note that I have assumed that the reader is familiar with cold atom experiments [54], particularly atom chip experiments [55]. Also, a general understanding of Bose-Einstein condensation is required [56, 57].

The journey of a lucky rubidium atom

When a Rubidium atom flies away from a Rubidium dispenser, it is at room temperature, that is 293.15 K. If that atom is one of the lucky ones who make it to the final trapping potential, it will be in a gas with a temperature of 0.000000050 K. To appreciate the difference in the order of magnitude in temperature, let's translate this energy difference to speed: If we slow down the light by this much, it would mean that it could travel only 1 km, instead of 300 000 km in one second! In such low temperatures, the atoms are almost not moving anymore. A rather unintuitive tool is used to slow down the atoms: Lasers! *Laser cooling* and *magnetic trapping* do the heavy lifting to cool down atoms to µK regime. To cool further to 20-150 nK, we use *evaporative cooling*, similar to cooling down a cup of coffee by blowing the hotter molecules away. In our experiment, we throw the more energetic atoms out of the trap, reducing the total energy of the gas and cooling it down. We finally end up with a cigar-shaped atomic gas containing 5000-100000 Rubidium atoms. The resulting atomic cloud is highly anisotropic with an aspect ratio of almost 1000. This state of matter is called quasi-one-dimensional quasi-Bose-Einstein condensate. The first "quasi" is because we live in a 3D world. The reason for the second "quasi" is that the Bose-Einstein condensation is prohibited in 1D because of the fluctuations. Check out section 2.1 to see how "1Dness" emerges from a 3D Hamiltonian.

3.1 Introducing the "KRb" setup

Our colloquially-called KRb setup, as the name suggests, is designed and built to investigate Bose-Fermi mixtures. The setup is capable of cooling and trapping bosonic (^{87}Rb) and fermionic atoms (^{40}K). In this thesis, however, we only work with rubidium atoms. In the heart of our setup lies an atom chip device, which is one of the various platforms developed for investigating cold atoms [58–60], molecules [61], and charged particles like ions [62] or electrons [63]. Advances in nano fabrication [64] enable the manufacturing complex structures of current-carrying microwires that create various magnetic field arrangements. These arrangements enable the confinement, cooling, and control of cold matter through various trapping methods, including electrostatic potentials [65] and radio frequency dressed state potentials [66].

In section 3.1.1, I give an overview of the setup, naming the essential techniques and devices used to run the experiment. After presenting the main aspects of the setup, I will introduce a timeline, summarizing a typical experimental cycle.

3.1.1 Overview

Before talking about the setup, let's talk about what we want from it: For analog quantum simulation of the field theories introduced in chapter 2, we want to create a pair of tunneling-coupled clouds of around ten thousand rubidium atoms below 100 nK.

Cold atom experiments are performed in a vacuum to isolate the atomic cloud from the environment. As depicted in fig. 3.1(c), our experimental configuration comprises two vacuum chambers interconnected through a differential pumping stage. We call the lower chamber, where ^{87}Rb atoms are continuously dispensed, the *source chamber*. The upper chamber, where the final condensates are realized, is called the *science chamber*. Using a two-chamber system makes it easier to maintain an extremely low vacuum pressure (10^{-10} mbar) in the science chamber.

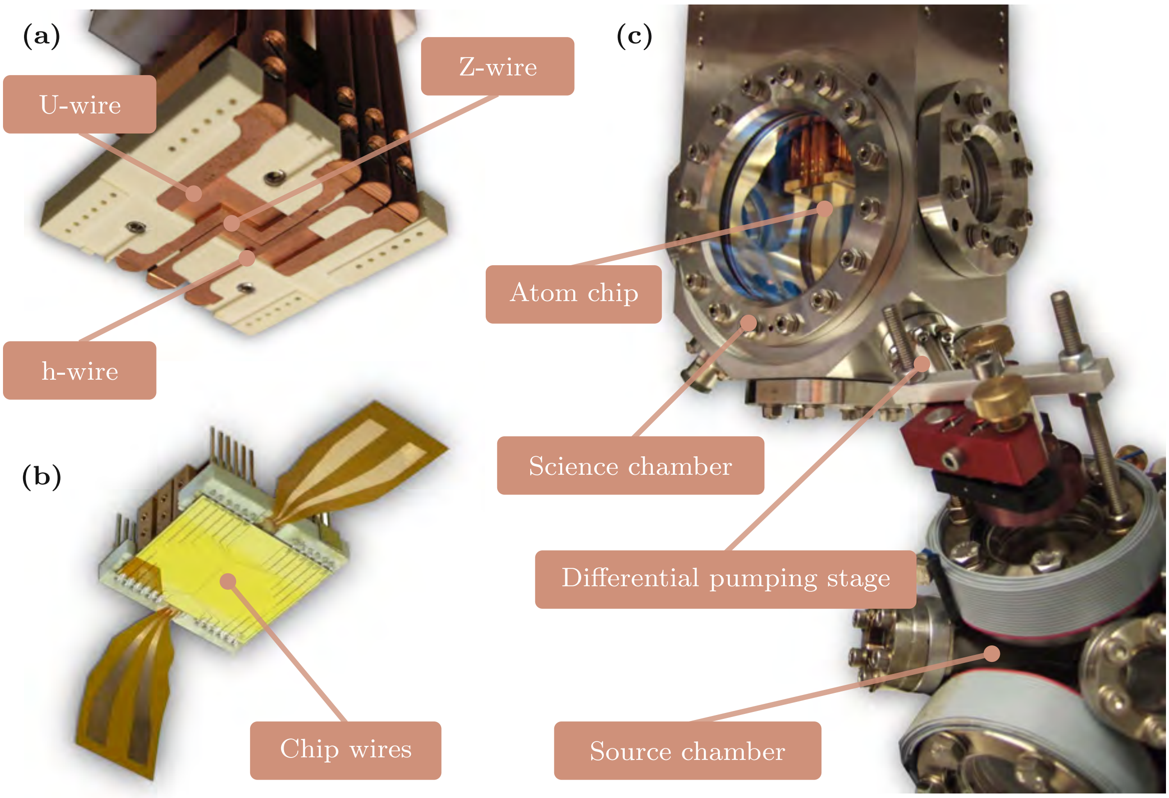
(a)
U-wire
Z-wire
h-wire
(b)
Chip wires
(c)
Atom chip
Science chamber
Differential pumping stage
Source chamber

Figure 3.1 Overview of the experimental setup: Macroscopic copper wires, atom chip, and vacuum chambers. **(a)** The macroscopic copper wire structures. **(b)** The atom chip is mounted above these copper wires. The structure of chip wires can be seen here. **(c)** Atoms are optically transported from the source chamber to the science chamber via a push beam. In the science chamber, they are trapped in a quadrupole trap formed by the macroscopic U-wire and bias coils. The Z-wire and the h-wire are then used to load the atoms in the chip trap, which is formed by chip wires and has a much smaller volume than the mirror MOT trap.

In the source chamber, room-temperature atoms are collected using a three-beam retro-reflected magneto-optical trap (MOT). Simultaneously, a push beam, nearly resonating with the atoms, propels them through the differential pumping stage into the science chamber, which is loaded into a mirror MOT near the chip surface.

A macroscopic Z-wire and h-wire (employed as a smaller Z-wire), as demonstrated in fig. 3.1(a), are combined with an external bias field to create an intermediate trap. This intermediate trap loads the atoms from the mirror MOT to the chip trap in the science chamber and also facilitates a pre-cooling process. This intermediate trapping stage is necessary due to the relatively smaller trapping volume of the chip trap compared to the mirror MOT. The atoms undergo further evaporative cooling [67] in the chip trap and can be manipulated using radio frequency-dressed state potentials or optical dipole traps. At this stage, we achieved our goal of producing a pair of tunneling-coupled quasi-1D quasi-condensates. But we still have to probe the system.

After performing the desired experimental protocol in the trap, we switch off all the traps, let the cloud fall under gravity, and freely expand before we take an absorption image [68] via resonant light. We call the time between switching off the traps and imaging the *time of flight* (TOF). The main observable in the experiment is the integrated 2D atomic density obtained by comparing the image taken from the atoms with a reference image taken shortly afterward. As our probing method is destructive, we perform the same experiment several times -depending on the experiment, between 50 to 1000 shots. In the next section, I will summarize a typical experimental cycle.

3.1.2 Experimental cycle

Chip experiments are famous for repeatability and robustness. Large statistics are often crucial for many measurements, making a short cycle time highly desirable. Below is a breakdown of a typical experimental cycle.

1 **Collection** (10 s): The rubidium vapor generated by a dispenser is collected, cooled, and transferred to the science chamber using the double MOT system depicted in fig. 3.1.

2 **Molasses** (7 ms): During this stage, the magnetic fields are deactivated, allowing the atoms to be cooled to 50 μK through sub-Doppler cooling.

3 **Optical pumping** (0.5 ms): An optical pumping pulse is applied to prepare the atoms in the maximally stretched state $|F = 2, m_F = 2\rangle$, which is a low-field seeking state.

4 **Intermediate trapping stage** (6 s): The macroscopic Z- and h-wires generate an Ioffe-Pritchard trap to load the atom chip in this stage. Evaporative cooling is initiated during this stage, which can further cool the atoms to $1-3\,\mu$K.

5 **Loading the chip trap** (0.5 s): During this stage, the macroscopic trap is gradually turned off while the chip trap is ramped up. Evaporative cooling is paused during the loading process. By the end of this stage, the magnetic trap is solely created by the chip wires along with the external bias coils.

6 **Further evaporative cooling in the chip trap** ($1.4 - 1.9$ s): Evaporative cooling is continued in the chip trap. Eventually, a 1D quasi-condensate is achieved, consisting of up to ten thousand atoms at temperatures ranging from 15 to 150 nK.

7 **Manipulation** ($0 - 500$ ms): Depending on the experimental requirements, additional manipulation can be performed during this stage, including modification of the transverse or longitudinal confinements by applying radio frequency fields or optical dipole potentials.

8 **Probing:** The trap is deactivated, allowing the atoms to fall under gravity. The atomic density is measured using absorption imaging, which causes the atoms to scatter away. We will discuss absorption imaging and our three imaging systems in the next section. With this step, an experimental cycle is completed.

3.2 Probing via absorption imaging

Our main method of probing the atoms is by measuring the integrated 2D atomic density via absorption imaging after expansion. The sub-micron transverse width of the condensates makes the *in situ* imaging unfeasible. Also, for two condensates, matter-wave interferometry relies on the overlap of the two atomic clouds that only happens after expansion.

Here, we first calculate the density of the clouds after a free (non-interacting) expansion. We then briefly mention the basics of absorption imaging in section 3.2.2, where we also introduce our three imaging systems in the experiment. Finally, in section 3.3.1 and 3.3.2, we summarize the observables for single-well and double-well experiments. Examples of typical absorption images with a sample code to analyze them are provided online [45].

3.2.1 Time of flight expansion

Considering two parallel condensates, we start by writing down the following Ansatz for the fields describing each, $j = 1, 2$,

$$\Psi_j(\vec{r}, t) = \phi_j(x, y, t)\psi_j(z, t) \, . \tag{3.1}$$

For the discussion in this section, we treat the fields as classical stochastic fields; hence, no hats. Similar to chapter 2, we write $\psi_j(z, t)$ in the phase-density representation,

$$\psi_j(z, t) = e^{\mathrm{i}\hat{\theta}_j(z,t)}\sqrt{\rho_j(z, t)} \, . \tag{3.2}$$

For the transverse field, $\phi_j(x, y, t)$, we further assume the ground state of the harmonic oscillator, which has a Gaussian form with a time-dependent width $\sigma(t)$,

$$\begin{aligned} \phi_1(x, y, t) &= \frac{1}{\sqrt{\pi\sigma^2(t)}} \exp\left(-\frac{(x + d)^2 + y^2}{2\sigma(t)}\right) \\ \phi_2(x, y, t) &= \frac{1}{\sqrt{\pi\sigma^2(t)}} \exp\left(-\frac{(x - d)^2 + y^2}{2\sigma(t)}\right) \, . \end{aligned} \tag{3.3}$$

The distance between the center of the trapped clouds is $2d$. Free expansion of these wave functions manifests itself in a growing width of the Gaussians,

$$\sigma(t) = a_\perp\sqrt{1 + \omega_\perp^2 t^2} \, , \tag{3.4}$$

with $a_\perp = \sqrt{\hbar/(m\omega_\perp)}$ being the *in situ* width of the Gaussian ground state. Note that a couple of assumptions must be made to put all the time dependence of ϕ_j in σ: First, we neglect the interactions during the expansion. Following that, we neglect the interaction-induced broadening. We further assume that the free expansion keeps Ψ_j factorizable, that is, eq. (3.1) holds at all times.

We are now ready to calculate the atomic density, $\rho(\vec{r}, t)$, of the two clouds after the expansion,

$$\begin{aligned} \rho(\vec{r}, t) = |\Psi_1(\vec{r}, t) + \Psi_2(\vec{r}, t)|^2 = |\psi_1(z, t)|^2|\phi_1(x, y, t)|^2 + |\psi_2(z, t)|^2|\phi_2(x, y, t)|^2 \\ + \mathrm{Re}\left[\psi_1^*(z, t)\psi_2(z, t)\phi_1^*(x, y, t)\phi_2(x, y, t)\right] \end{aligned} \tag{3.5}$$

Replacing eqs. (3.2) and (3.3) in eq. (3.5), we obtain

$$\begin{aligned}\rho(\vec{r},t) =& \frac{1}{\pi\sigma^2(t)}\exp\left(\frac{-y^2}{\sigma^2(t)}\right)\Bigg\{\rho_1(z,t)\exp\left(-\frac{(x+d)^2}{\sigma^2(t)}\right)\\ &+\rho_2(z,t)\exp\left(-\frac{(x-d)^2}{\sigma^2(t)}\right)\\ &+2\sqrt{\rho_1(z,t)\rho_2(z,t)}\exp\left(-\frac{x^2+d^2}{\sigma^2(t)}\right)\cos\left[2\pi\frac{x}{\lambda_\mathrm{F}(t)}-\varphi_-(z,t)\right]\Bigg\}\,.\end{aligned} \tag{3.6}$$

Here, $\varphi_-(z,t) = \theta_1(z,t) - \theta_2(z,t)$ is the relative phase between the condensates, and $\lambda_\mathrm{F}(t)$ is the fringe spacing,

$$\lambda_\mathrm{F}(t) = \frac{\pi m a_\perp^2}{\hbar d}\frac{\sigma^2(t)}{t} = \frac{\pi m a_\perp^4}{\hbar d}\frac{1+\omega_\perp^2 t^2}{t}\,. \tag{3.7}$$

For $x \gg d$, the density is approximated by

$$\begin{aligned}\rho(\vec{r},t) = \frac{\rho_1(z,t)+\rho_2(z,t)}{\pi\sigma^2(t)}\exp\left(-\frac{x^2+y^2}{\sigma^2(t)}\right)\Bigg\{1\\ +\frac{2\sqrt{\rho_1(z,t)\rho_2(z,t)}}{\rho_1(z,t)+\rho_2(z,t)}\cos\left[2\pi\frac{x}{\lambda_\mathrm{F}(t)}-\varphi_-(z,t)\right]\Bigg\}\,.\end{aligned} \tag{3.8}$$

We will use this equation later in section 3.3.2.

In the experiment, we always measure $\rho(\vec{r},t)$ integrated along the imaging direction. It is obvious that for a single condensate, $\rho_2(z,t) = 0$ and $d = 0$. For a more detailed discussion, one should refer to **Schweigler-Thesis** section 2.6.1 or **Rauer-Thesis** section 3.3.1 and references therein.

3.2.2 Absorption imaging: quantifying shadows

In our experiment, we see the atoms by looking at their shadows. Absorption imaging relies on quantifying the absorbed light from an incoming beam. In the experiment, we have three imaging systems along every spatial direction as demonstrated in fig. 3.2. Be reminded that the z-axis is aligned with the weakly confined direction of the cigar-shaped condensates, and x- and y-axis are the transverse directions, with the positive y-axis pointing in the direction of gravity.

I will briefly introduce each absorption imaging system after discussing how integrated density profiles are estimated from absorption pictures.

Die approbierte gedruckte Originalversion dieser Dissertation ist an der TU Wien Bibliothek verfügbar.
The approved original version of this doctoral thesis is available in print at TU Wien Bibliothek.
TU Bibliothek WIEN Your knowledge hub

How much resonant light is absorbed by a cloud of atoms depends on the density of the cloud. The integrated density along an imaging axis z, denoted by $\rho(x,y) = \int dz \rho(\vec{r})$, is related to the intensity of the incoming beam, $I_0(x,y)$, and the intensity after the absorption,$I(x,y)$, by

$$\rho(x,y) = \frac{1}{\sigma_{\text{abs}}} \ln\left(\frac{I_0(x,y)}{I(x,y)}\right) + \frac{I_0(x,y) - I(x,y)}{\sigma_{\text{abs}} I_{\text{sat}}} \,. \tag{3.9}$$

Here, the atoms are approximated as a two-level system in equilibrium. In eq. (3.9), I_{sat} is the saturation intensity, and σ_{abs} the absorption cross-section. Measuring $I(x,y)$ and $I_0(x,y)$ (measured by taking a second picture without any atoms present), we can determine $\rho(x,y)$.

In the experiment, I_0 and I can not be measured at the same time. First, the absorbed intensity is collected by a CCD camera, and then after a short time, the reference beam is measured. Having the gain and quantum efficiency of the camera, we can measure the absolute intensity. For the imaging beam, we use laser light in resonance with the $F = 2 \rightarrow F' = 3$ transition of the ^{87}Rb D_2 line. Our typical intensities lay between 15% to 35% of the saturation intensity.

In the following, I will introduce the optical setups used for absorption imaging in our system. Note that throughout this manuscript, the width of the Gaussian approximation for the point-spread function, σ_{PSF}, represents the *effective* imaging resolution of our imaging systems. After TOF, the cloud expands, and its size extends beyond the depth of field of the imaging system. Furthermore, the imaging beam pushes the cloud through the focal region. As a result, the point spread function becomes blurred, leading to an effectively larger spot size. The size of this expanded spot depends on factors such as atomic density, imaging intensity, and exposure time. A comprehensive analysis of these effects, along with a detailed investigation of the imaging quantization axis, light polarization, and the impact of stray fields, can be found in **Schweigler-Thesis**.

Vertical imaging system

The main results of this thesis are based on spatially resolved relative phase profiles, $\varphi_-(z)$, extracted from the integrated 2D densities, $\rho(x,z)$ obtained by the vertical imaging system.

The imaging system comprises a single doublet objective lens and a two-lens telephoto combination, which projects the image onto a CCD camera[1]. With a

---

[1] Andor iXon DV887DCS-BV. An EMCCD camera is utilized without the electron multiplier mode

Die approbierte gedruckte Originalversion dieser Dissertation ist an der TU Wien Bibliothek verfügbar.
The approved original version of this doctoral thesis is available in print at TU Wien Bibliothek.
TU Bibliothek WIEN Your knowledge hub

magnification of 8.22×, the pixel size in the object space is 1.95 µm, providing a field of view measuring 1 mm × 1 mm.

Due to the atoms' fall during expansion, the focus of the system needs to be adjusted to achieve the desired TOF. However, this adjustment is complicated by astigmatism in the optical setup caused by a slight tilt of the imaging light path in relation to the optical axis. By utilizing different features along the x- and z-axes to independently locate the two foci, we can quantify this aberration and compensate for it. The foci obtained from these two methods[2] exhibit a discrepancy of approximately 120 µm. For the results presented in this thesis, we use a TOF of 15.6 ms, which corresponds to the point between the two focal points and turned out to be the ideal point to record interference fringes.

Without astigmatism, one would expect a diffraction-limited spot size of 2.2 µm, based on a numerical aperture (NA) of 0.08. However, in practice, the effective spot size for the expanded and displaced cloud depends on the chosen focus and the specific feature of interest.

Furthermore, it is necessary to shield the vertical imaging CCD from stray light originating from the dipole trap. As the dipole beam reflects off the chip surface, some light scatters from the etched trenches between the wires and impurities on the chip surface. To prevent this scattered light from reaching the CCD, a shutter is positioned directly in front of the camera. More information on this setup can be found in [36], **Rauer-Thesis**, and **Schweigler-Thesis**.

Transverse imaging system

To measure the density along the z-axis with a better resolution or shorter TOF, we use this imaging system. Its imaging axis is aligned with the x-axis (transverse to the z-axis).

The imaging system is oriented at a 2° angle to the chip surface, allowing the imaging light to be reflected from the surface. This configuration enables measurements of clouds after very short expansion times. When the expansion times exceed 10 ms, atomic clouds move sufficiently far from the chip, allowing the imaging light to pass beneath it without reflection. The imaged density distribution is integrated along an axis that is nearly aligned with the x direction. In the case of two gases released from a double-well trap, the imaging process integrates out all of the interference effects.

A schematic of the optical setup can be found in fig. 4.4, which illustrates how the optical system used for the optical dipole trapping is integrated into the transverse imaging system. The central component of the imaging system is a custom-built four-lens objective with a numerical aperture (NA) of 0.26. Combined with a two-lens telephoto system on the image side, this imaging setup magnifies the observed density distributions by 12.4× onto a CCD camera[3]. The pixel size in the object space is 1.05 µm, and the field of view covers 1.07 mm × 0.72 mm, allowing for the observation of falling clouds for up to 12 ms.

---

[2] See **Rauer-Thesis** for details of these measurements.

An additional adjustable circular aperture, set to a diameter of approximately 36 mm in the parallel part of the imaging system, limits the effective NA to 0.20, minimizing aberrations. This configuration yields a diffraction-limited intensity spot with a width of $\sigma_{\mathrm{PSF}} = 0.9\,\mu\mathrm{m}$ when approximated by a Gaussian. However, due to the small depth of field resulting from the large NA, the resolution is significantly reduced by the spatial extension of the cloud and the push through the focal plane. For typical cloud sizes and imaging parameters, the measured effective spot size, σ_{PSF}, ranges between 1.7 µm and 2.1 µm.

Since the imaging axis is not perfectly perpendicular to the direction of gravity, the focal point obtained for the standard TOF of 11.2 ms is shifted by 21 µm compared to the cloud position after 2 ms TOF, which is the chosen expansion time for our quasi-*in situ* imaging. Moreover, as the transverse cloud size is much smaller after this short expansion and the push through the focal plane is non-linear, the optimal focal point to minimize the effective spot size will be different. However, adjusting the focus for short expansion times is not feasible for the *in situ* measurements presented in the next chapter. Another challenge when dealing with short expansion times is the reflection of imaging light from the chip surface. This reflection creates a standing wave pattern at the atoms' location and introduces an additional virtual image that requires consideration and correction during the experimental analysis. Therefore, all density profiles presented in this thesis, measured with short expansion times, were rescaled to match the expected total number of particles independently measured at the standard TOF.

Longitudinal imaging system

The third imaging system is aligned with the weakly confining axis of the chip trap, enabling the integration of expanded density distributions along the z-axis and providing information about the particle distribution in the xy plane.

---

[3] Andor DV435-BV-958

The imaging system is composed of two doublet lenses and a CCD camera,[4]. It offers a magnification of 5.3×, resulting in a pixel size of 2.45 µm in the object space. The field of view spans 2.51 mm × 1.67 mm, allowing for distortion-free observation of falling atom clouds during a time-of-flight (TOF) ranging from 4 to 18 ms.

Combined with the dipole trap, the longitudinal imaging is limited to TOFs shorter than 11 ms due to light scattered from the chip structures. For shorter TOFs, the camera's cleaning shift is sufficiently fast to clear the region of interest. However, no mechanism is installed to prevent the dipole light from reaching the CCD.

This setup allows access to information regarding the transverse degrees of freedom. In fig. 3.2(a), an expanding quasi-condensate's transverse Gaussian density distribution is displayed. When gases are released from a double-well trap, interference patterns can be observed. However, due to the integration along the z-axis, the fringes become smeared for quasi-condensates with significant relative phase fluctuations, resulting in high contrast only for phase-coherent samples (see fig. 3.2(d)). This imaging system is only used to calibrate the double-well potential by balance measurements as explained in section 3.3.2.

3.3 Experimental observables

3.3.1 A single condensate

As mentioned in chapter 2, the phase of a single condensate is not a physical observable. Hence, absorption imaging only gives us access to the cloud's density after expansion. From single experimental shots, spatially resolved density fluctuations, $\delta\rho(z)$ can be measured. These fluctuations can be used to determine the temperature in both single or double well potentials. But in this thesis, we only work with pairs of coupled condensates. Hence, I shift the discussion of thermometry via density ripples to the next section. Also, using an ensemble of experimental realizations, the average density, $\rho_0(z)$ can be measured.

The simulated images of a single expanded cloud are shown in fig. 3.2(a-c). Here, the pictures taken by the vertical (c) and transverse (b) imaging systems contain the same information. However, as mentioned earlier, the resolution of the transverse imaging system is better.

---

[4] Andor DV435-BV-958

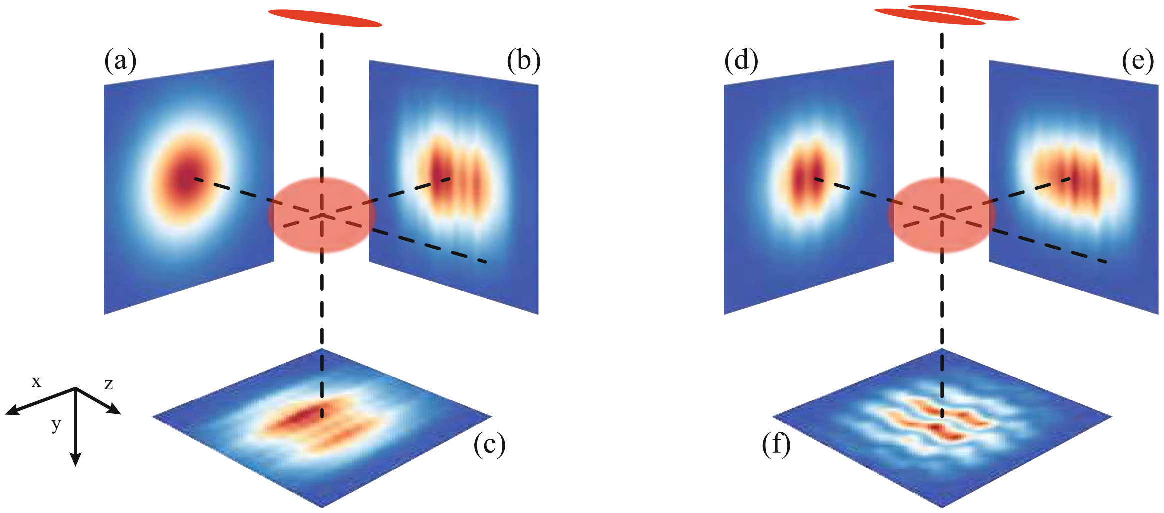

Figure 3.2 Schematic of available imaging directions. Left panel: A schematic illustrating the expansion of a single 1D quasi-condensate (depicted in red) and the orientations of the imaging axes (indicated by dashed lines) relative to the cloud's geometry. The panels perpendicular to the imaging axes, **(a-c)**, display density distributions obtained by integrating along the corresponding axes, related to the longitudinal, transverse, and vertical imaging systems, respectively. **Right panel:** The same depiction for a pair of 1D tunneling-coupled condensates released from a double-well potential. In this case, interference fringes can be observed by longitudinal **(d)** and vertical imaging **(f)**. The transverse imaging system **(e)** records the common density fluctuation after TOF. Figure adapted with permission from **Rauer-Thesis**.

3.3.2 Coupled condensates

The simulated images after expansion are shown in fig. 3.2(d-f) for a pair of parallel condensates. Now we can extract relevant information from each imaging direction: We use the images from the vertical imaging system to calculate the relative phase, $\phi_-(z)$. The common density fluctuations, $\delta\rho_+(z)$, can be measured from the images taken with the transverse imaging system. Last but not least, we use the longitudinal imaging system to compare the total number of atoms in each well and ensure a balanced double-well trap.

Spatially-resolved relative phase

For two parallel condensates after expansion, the absorption images of the vertical imaging system provide us the density given by eq. (3.8), integrated along the y-axis, that is $\rho(x,z) = \int \mathrm{d}y\, \rho(\vec{r}, t_{\mathrm{TOF}})$. A simulated image is shown in fig. 3.2(f), and an experimentally measured example is shown in fig. 3.3.

To extract the relative phase, we fit the following function to every slice with a fixed z,

$$f_z(x) = A \exp\left(-\frac{(x-x_0)^2}{\sigma_{\mathrm{TOF}}^2}\right)\left\{1 + C\cos\left[2\pi\frac{x-x_0}{\lambda_{\mathrm{F}}} - \varphi_-\right]\right\} + B\,. \tag{3.10}$$

The function has seven fit parameters:

- φ_-: This is the relative phase for that z slice.
- A: An overall amplitude.
- B: An overall offset accounting for noise.
- C: The fringe contrast.
- x_0: The center of the Gaussian envelope. Note that in the theoretical calculation of section 3.2.1, we assumed that $x_0 = 0$. Here, we don't have that information, and x_0 has to be determined by fitting.
- σ_{TOF}: The Gaussian width of the transverse wave function after expansion, that is $\sigma(t_{\mathrm{TOF}} = 15.6\,\mathrm{ms})$ in the measurements presented in this thesis.
- λ_{F}: The fringe spacing after expansion, $\lambda_{\mathrm{F}}(t_{\mathrm{TOF}} = 15.6\,\mathrm{ms})$

An example of a slice is illustrated in fig. 3.3. Since φ_- is in the argument of a cosine function, we can only estimate it up to a multiple of 2π for every slice. We then impose continuity and perform phase unwrapping to get a profile similar to the one shown in fig. 3.3. Note that a global $2\pi n$ ambiguity persists.

Density ripples thermometry

In chapter 6, we report the temperature of the thermal state in equilibrium. Although we deal with the relative degrees of freedom, we assume that the temperature of common and relative degrees of freedom are the same in thermal equilibrium. To obtain the reported temperatures in that chapter, we observe "density ripples" that emerge during extended periods of free expansion. The initial thermal phase fluctuations manifest as density fluctuations following an 11.2, ms free expansion, enabling the extraction of temperature information by analyzing their correlations [69]. Section

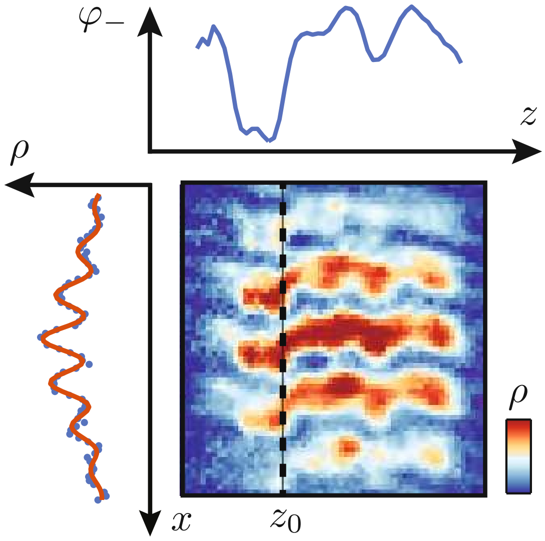

Figure 3.3 Extraction of the relative phase profile from interference fringes. After free fall and expansion, the two-dimensional projected density profile, $\rho(x, z)$, is obtained by absorption images taken by the vertical imaging system. The spatially resolved relative phase $\varphi_-(z)$ is determined from interference fringes. For every slice in the z direction, a cosine function multiplied by a Gaussian bell is fitted to extract the relative phase. A sample slice is shown at $z = z_0$.

4.1.3 of **Schweigler-Thesis** thoroughly explains the tunneling-coupled condensates method. We have also developed a machine learning-based temperature estimation method from post-expansion density ripples [70].

Atomnumber balance in double-well potentials

For all of the double-well experiments in this thesis, we assume that the trapping potentials and the chemical potential are the same for both of the condensates, resulting in the same averaged density, ρ_0 as mentioned in chapter 2. To this end, before starting a measurement, we do a so-called balance measurement, in which we adjust the current difference between the two radio frequency wires and measure the atom number in each well using the longitudinal imaging system. To separate the clouds, we ramp down the amplitude of the radio frequency fields 0.1 ms before turning off the static traps, giving them a slight kick in opposite directions.

Chapter 4

Arbitrary one-dimensional potentials on an atom chip

Combining optical and magnetic potentials

In this chapter, I will discuss the trapping techniques in detail, especially the addition of optical dipole traps to the experimental setup, which was my project at the very early stage of my studies.

As I mentioned in chapter 1, using an experimental platform as an analog quantum simulator requires certain degrees of tunability, or the way I like to call them, *knobs*. Among all the essential experimental details, the shape of the magnetic and optical dipole traps controls both relevant experimental knobs in our system. Please note, however, that this is a very brief introduction. For more details on trapping techniques, refer to **Tajik-Thesis** and **Rauer-Thesis**.

First, the single particle tunneling rate between the two condensates, denoted by J in chapter 2, is controlled by the radio frequency dressed potentials. Second, the trapping potential in the longitudinal axis, $U(z)$, is given by the sum of the magnetic and optical dipole potentials. This potential determines the average density profile in 1D, $\rho_0(z)$, which ultimately sets the speed of sound in the condensates. A sketch of the setup is presented in fig. 4.1.

In section 4.1, we will see the theoretical basis of magnetic trapping and how it is applied in different experiment stages. Section 4.2 discusses the creation of double-well potentials with radio frequency signals. And finally, we discuss the realization of arbitrary optical dipole potential through beam shaping in section 4.3. Parts of this chapter have been published in [71], with some parts having substantial overlap, and others being borrowed verbatim.

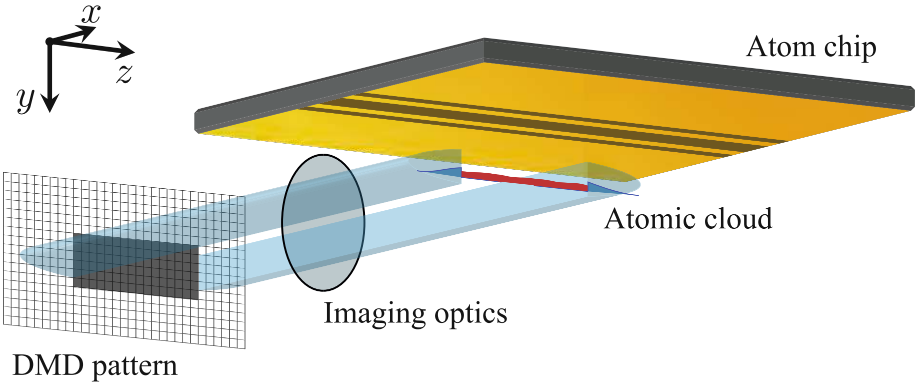

Figure 4.1 Combining optical dipole and magnetic potentials on an atom chip. The spatial pattern produced by a digital micromirror device (DMD) is projected onto the atomic cloud plane below the atom chip, allowing precise modification and "correction" of the trapping potential provided by the chip. The x-axis aligns with the propagation direction of the dipole light, while the y-axis points towards the direction of gravity, and the z-axis aligns with the longitudinal direction of the atom chip trap. The schematic representation of the DMD pattern presented here demonstrates the selective removal of the central part of the elongated Gaussian beam, resulting in steep potential walls on its sides. For a more detailed example of how the intensity profile corrects the potential roughness, refer to fig. 4.2, and for a typical DMD pattern, see fig. 4.6.

4.1 Static magnetic potentials

The common method to confine neutral atoms in our experiment is to use the magnetic interaction between the atomic pin degree of freedom and a *static* magnetic field. The resulting magnetic potential is given by

$$U_{\mathrm{mag}}(\vec{r}) = -\vec{\mu} \cdot \vec{B}(\vec{r}) \ , \tag{4.1}$$

where $\vec{\mu}$ is the magnetic dipole moment and $\vec{B}(\vec{r})$ is the magnetic field. For an atom with angular momentum $\vec{F}$, the magnetic dipole moment is given by $\vec{\mu} = -g_F \mu_{\mathrm{B}} \vec{F}$. Here, g_F is the Landé g-factor associated with $\vec{F}$, and μ_{B} is the Bohr magneton. The magnetic potential for this atom in a weak magnetic field, where $\vec{F}$ is still a good quantum number, can be written as

$$U_{\mathrm{mag}}(\vec{r}) = g_F \mu_{\mathrm{B}} \vec{F} \cdot \vec{B}(\vec{r}) = m_F g_F \mu_{\mathrm{B}} |\vec{B}(\vec{r})| \ , \tag{4.2}$$

where we assumed that the vector $\vec{F}$ always follows the direction of the magnetic field. Hence, only m_F, the quantum number along $\vec{B}$, shows up in the equation.

For an atom in a specific state, if the product of m_F and g_F is positive ($m_F g_F > 0$), it tends to move towards areas with lower magnetic field strength to minimize its energy. These states are commonly referred to as low-field-seeking states. Conversely, when $m_F g_F$ is negative ($m_F g_F < 0$), the atom is attracted to regions with stronger magnetic fields. These states are known as high-field-seeking states. However, high-field-seeking states cannot be confined to a particular area in free space due to the constraints imposed by Maxwell's equations, which prevent a maximum magnetic field in free space.

In the following, I introduce two important magnetic field configurations widely used in ultra-cold atom experiments.

4.1.1 Quadrupole traps

Quadrupole traps are achievable through magnetic field configurations where the minimum of the magnetic trap occurs at a point where the magnetic field crosses zero. The simplest form of a quadrupole field can be expressed as $\vec{B}(\vec{r}) = \hat{x}\, B'_x x + \hat{y}\, B'_y y + \hat{z}\, B'_z z$, where B'_x, B'_y, and B'_z are constants satisfying the equation $B'_x + B'_y + B'_z = 0$ as per Maxwell's equations. The magnitude of the field $|\vec{B}(\vec{r})| = \sqrt{(B'_x x)^2 + (B'_y y)^2 + (B'_z z)^2}$ is linear in each spatial dimension and reaches a minimum value of zero at the center of the trap.

For colder atomic ensembles, this zero crossing is the cause of the so-called Majorana spin flips: Let's consider a reference frame fixed to an atom in a low-field-seeking state moving within a trap with a magnetic field minimum. In this reference frame, the atom's position remains fixed, and the magnetic field acting on the atom becomes a time-varying field $\vec{B}(t)$. As long as the atom's quantization axis can adiabatically follow the changes in the magnetic field's direction, the atom will remain trapped, and equation 4.2 will hold. However, if the direction of the magnetic field (let's call it $\theta(t)$) changes faster than the Larmor frequency $\omega_\mathrm{L}(t) = m_F g_F \mu_\mathrm{B} |\vec{B}(t)|/\hbar$, a spin flip may occur, leaving the atom in an untrapped state. Therefore, the trap remains stable only if the change in the magnetic field direction $\theta(t)$, as observed by the atom, occurs at a slower rate than the Larmor frequency, $d\theta(t)/dt < \omega_\mathrm{L}(t)$. This condition can be violated in regions near the minima of the magnetic field where the field strength is small, leading to the above-mentioned Majorana spin flips.

Avoiding these losses is vital to creating Bose-Einstein condensates and ultra-cold atomic samples, as we will discuss one of the workarounds in the next section. However, in the earlier stages of the experiment, we use quadrupole traps to confine atoms for the cooling processes. In the source chamber, we create a 3D quadrupole trap using three sets of coils arranged in an anti-Helmholtz configuration surrounding the source chamber. A U-shaped macroscopic structure (depicted in fig. 3.1) along with a pair of coils arranged in a Helmholtz configuration is utilized to achieve a quadrupole trap near the chip.

4.1.2 Ioffe-Pritchard traps

Designing desired field configurations is challenging because Maxwell equations highly constrain them. The following field configuration creates a harmonic trap with a non-zero minimum, which is known as Ioffe-Pritchard configuration [72, 73].

$$\begin{aligned}\vec{B}(\vec{r}) = {} & (B'\,x - \frac{B''}{2}\,xz)\,\hat{x} \\ & + (-B'\,y - \frac{B''}{2}\,yz)\,\hat{y} \\ & + B_{\text{bias}}\,\hat{z} + \frac{B''}{2}\Big(z^2 - \frac{1}{2}(x^2+y^2)\Big)\,\hat{z}\,.\end{aligned} \tag{4.3}$$

The approximate field strength around the origin ($x, y \ll B_{\text{bias}}/B'$, $z \ll \sqrt{B_{\text{bias}}/B''}$) is

$$|\vec{B}(\vec{r})| = B_{\text{bias}} + \frac{B''}{2}z^2 + \frac{1}{2}\Big(\frac{B'^2}{B_{\text{bias}}} - \frac{B''}{2}\Big)(x^2+y^2)\,. \tag{4.4}$$

The resulting magnetic potential based on eq. (4.2) is

$$U_{\text{mag}}(\vec{r}) = m\omega_z^2\,z^2/2 + m\omega_\perp^2\,(x^2+y^2)/2\,, \tag{4.5}$$

where m is the mass of a rubidium atom in our experiment, and ω_z and $\omega_\perp$ are the longitudinal (axial) and transverse trapping frequencies, respectively, and are given by the following equations,

$$\omega_z = \sqrt{\frac{m_{\text{F}} g_{\text{F}} \mu_{\text{B}}}{m} B''} \approx 2\pi \times 10\,\text{Hz} \tag{4.6}$$

$$\omega_\perp = \sqrt{\frac{m_{\text{F}} g_{\text{F}} \mu_{\text{B}}}{m}\Big(\frac{B'^2}{B_{\text{bias}}} - \frac{B''}{2}\Big)} \approx 2\pi \times 2\,\text{kHz}\,. \tag{4.7}$$

The aspect ratio $\omega_\perp/\omega_\parallel$ shows how isotropic the trap is. In our experiment, the microfabricated wires on the atom chip create highly anisotropic cigar-shaped condensate with aspect ratios of about 200.

Die approbierte gedruckte Originalversion dieser Dissertation ist an der TU Wien Bibliothek verfügbar.
The approved original version of this doctoral thesis is available in print at TU Wien Bibliothek.
TU Bibliothek WIEN Your knowledge hub

4.2 Radio frequency dressed potentials

So far, we have discussed a highly anisotropic static magnetic potential using an atom chip. But the atom chips are capable of more: Our atom chip has, additionally, a pair of microwires carrying radio frequency currents. They are designed such that the resulting radio frequency field near the trap minimum is almost homogeneous. The trapping potential stemming from the superposition of the static magnetic field $\vec{B}_{\text{stat}}(\vec{r})$ discussed above and the rapidly oscillating radio frequency field, $\vec{B}_{\text{RF}}(\vec{r})\cos(\omega_{\text{RF}}t)$, turns out to be

$$\begin{aligned} U_{\text{chip}} &= m'_F g_F \mu_{\text{B}} \sqrt{\Big(|\vec{B}_{\text{stat}}(\vec{r})| - \frac{\hbar\omega_{\text{RF}}}{|g_F|\mu_{\text{B}}}\Big)^2 + \Big(\frac{|\vec{B}_{\text{RF},\perp}(\vec{r})|}{2}\Big)^2} \\ &= m'_F \hbar \sqrt{\Delta^2(\vec{r}) + \Omega^2(\vec{r})}\ , \end{aligned} \tag{4.8}$$

where m'_F is the quantum number of the dressed basis, $\vec{B}_{\text{RF},\perp}(\vec{r})$, is the component of the radio frequency field that is perpendicular to the static magnetic field, $\vec{B}_{\text{RF},\perp}(\vec{r}) \cdot \vec{B}_{\text{stat}}(\vec{r}) = 0$.

In our experiment, we control the radio frequency fields by independently adjusting the current flow in the two wires. The relative phase between the currents determines the orientation of the field. We obtain a linearly polarized radio frequency field perpendicular to the chip surface by setting this relative phase to π. We choose to have a positive detuning, $\Delta > 0$, where $\omega_{\text{RF}} = 2\pi \times 360\,\text{kHz}$ is slightly lower than the Zeeman splitting (about $2\pi \times 390\,\text{kHz}$). In this case, a double-well configuration is formed after a critical field strength. Adjusting the barrier height tunes the single-particle tunneling rate, J, which is one of the crucial knobs in our quantum field simulator.

4.3 Optical dipole potentials

Although various trapping geometries can be produced using radio frequency dressed state potentials, once the atom chip is designed, adjusting the longitudinal confinement is greatly limited. Moreover, there exists potential roughness due to imperfections of micro-wires on the chip [74]. Adding an optical dipole potential allows us to correct the potential roughness and shape of the longitudinal trapping potential.

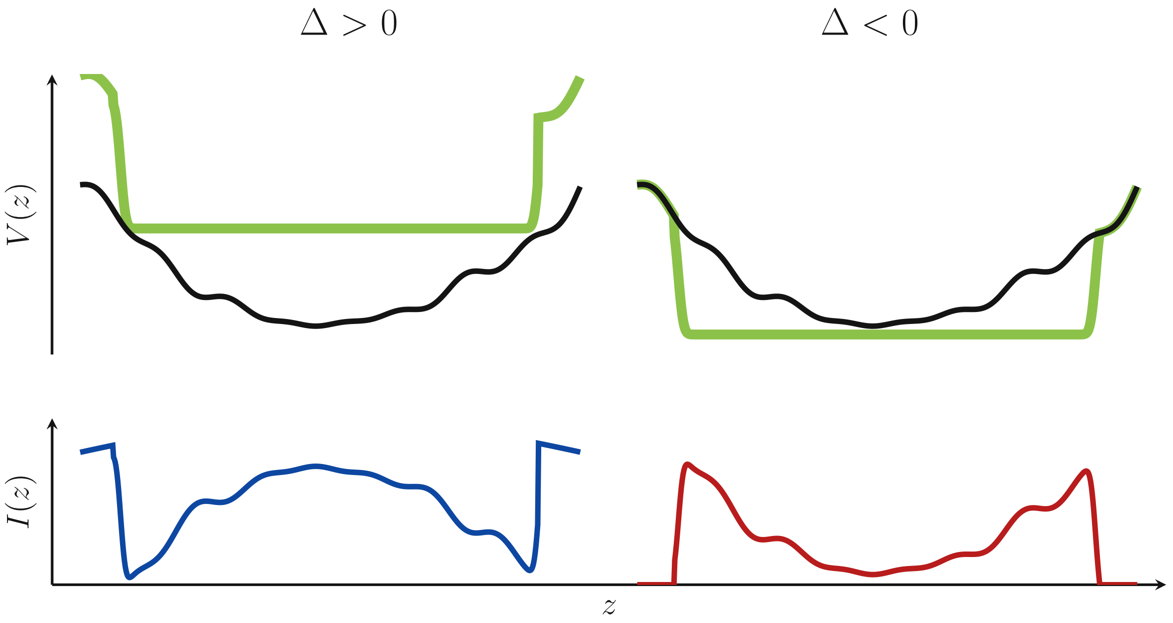

Figure 4.2 Creating a box-like potential (green) by adding blue- or red-detuned light ($\Delta > 0$ and $\Delta < 0$ respectively) to a rough harmonic potential (black). The potentials and intensity profiles needed to achieve those are presented.

4.3.1 Arbitrary optical dipole potentials via beamshaping

The potential generated by the interaction of a light field with a driving frequency ω_L and the induced dipole moments of neutral atoms with the transition frequency ω_0 can be approximated by

$$V_\mathrm{dip}(\vec{r}) = \frac{3\pi c^2}{2\omega_0^3}\frac{\Gamma}{\Delta} I(\vec{r}) \;, \tag{4.9}$$

where $\Delta = \omega - \omega_0$ is the detuning, c is the speed of light, and Γ is the on-resonance damping rate [75][1]. The sign of Δ determines whether the potential is attractive ($\Delta < 0$, red-detuned) or repulsive ($\Delta > 0$, blue-detuned). To illustrate this concept, fig. 4.2 shows how the appropriate intensity distribution can compensate for the imperfect harmonic confinement and create a box-like potential by adding either blue- or red-detuned dipole potentials.

The corresponding light beams' spatial properties determine the optical dipole potentials' characteristics. This opens up possibilities for beam-shaping techniques using Spatial Light Modulators (SLMs) to manipulate not only the intensity but also the phase of the light fields. In our setup, we utilize a Digital Micromirror Device

---

[1] A comprehensive introduction to optical dipole traps for neutral atoms is given in reference [75]. A brief derivation of eq. (4.9) can be found in **Tajik-Thesis** section 2.2.

Die approbierte gedruckte Originalversion dieser Dissertation ist an der TU Wien Bibliothek verfügbar.
The approved original version of this doctoral thesis is available in print at TU Wien Bibliothek.
TU Bibliothek WIEN Your knowledge hub

(DMD), which is a reflective SLM capable of fast and flexible intensity modulation of light fields.

Although DMDs offer great control and speed, they are limited to producing pixelated binary patterns. Temporal and/or spatial averaging techniques must be applied to generate grayscale images from these binary patterns.

When imaging the 2D binary pattern of the DMD, we obtain a 2D intensity distribution, $I(y, z)$, on the image plane, where the atomic cloud is located (plane of atoms). Since we have 1D Bose gases confined in highly anisotropic magnetic traps as discussed in section 4.1, the transverse width of the atomic cloud, $a_\perp \approx 250\,\mathrm{nm}$ is significantly smaller than the resolution of a typical optical imaging system. Consequently, only a tiny segment of the image, $I(z) \equiv I(y = y_{\mathrm{cloud}}, z)$, is relevant for shaping the longitudinal potential, assuming the cloud is located at y_{cloud}.

We employ spatial averaging of the binary DMD pattern to achieve fine intensity resolution in the projected light pattern. This is accomplished by designing an imaging system with a significant demagnification factor that enables multiple binary pixels to contribute to a single diffraction-limited spot in the image plane (see fig. 4.3).

Spatial filtering is an additional tool that affects the optical resolution of the system by manipulating the Fourier components of light. Blocking high-frequency components degrades the optical resolution, expanding the contribution range of a single DMD pixel. For 1D systems, where only the resolution along the longitudinal direction matters, reducing the numerical aperture along the perpendicular direction leaves the longitudinal resolution unaffected while allowing more pixels from the perpendicular direction to contribute to the 1D intensity. This enhances the potential's tunability at $y = y_{\mathrm{cloud}}$. However, the trade-off for spatial filtering is a reduction in overall intensity.

Note that we are mainly interested in shaping the intensity of the light field. Thus, we choose to image the DMD pattern directly. Putting the DMD in the Fourier plane can allow for the modulation of both phase and intensity [76]. However, if phase modulation is unnecessary, direct imaging proves to be a more straightforward method.

4.3.2 Optical setup

To create the dipole potentials, we use an "opus660" laser from "Laser Quantum", with wavelength $\lambda_{\mathrm{dip}} = 660\,\mathrm{nm}$ which provides 1.5 W of spatially single mode light, blue-detuned with respect to the D line of ^{87}Rb ($\lambda_{\mathrm{D}_2} = 780\,\mathrm{nm}$, $\lambda_{\mathrm{D}_1} = 795\,\mathrm{nm}$). A blue-detuned light field is advantageous for our primary purpose, that is correcting an existing potential and creating potentials with steep walls in 1D. The choice of λ_{dip} is mainly motivated by the anti-reflection coating of the existing optical elements in

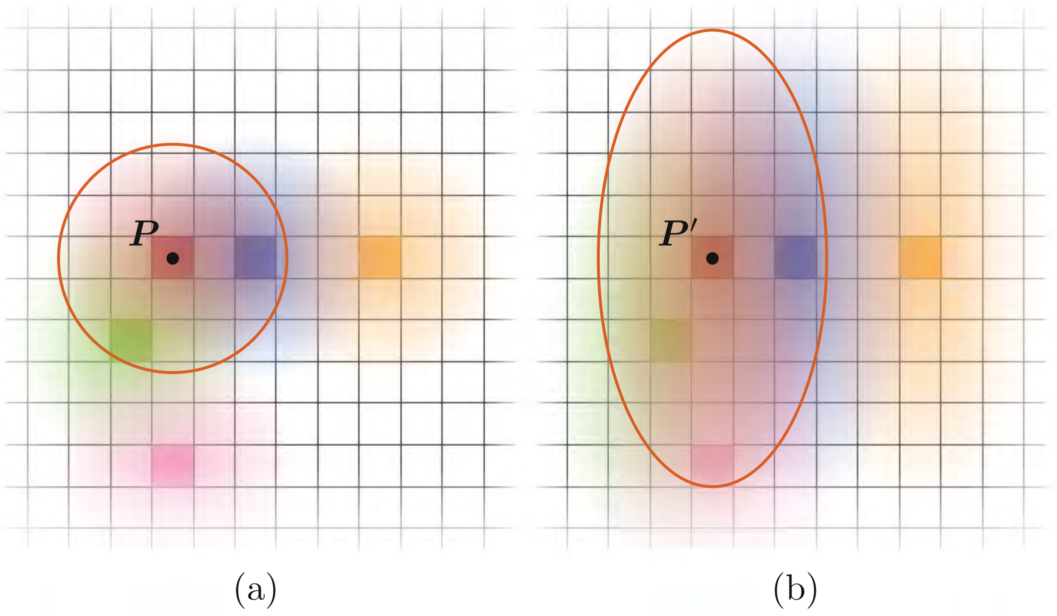

Figure 4.3 Expanding the dynamic range of intensity using the concept of spatial averaging and spatial filtering. The images of single DMD pixels are shown in the image plane. The DMD pixels are well resolved in the image plane for a diffraction-limited spot much smaller than the pixel size. Of the five pixels switched on (shown in different colors), only one (red) would contribute to the intensity of point P (P′). If the image is blurred due to the finite imaging resolution, the pixels are imaged as broad, overlapping spots. In this case, all pixels within the orange circle (ellipse) contribute to the intensity of point P (P′). In (a), the point spread function (PSF) of the imaging system is symmetric, and three of the five active pixels (red, blue, green) contribute substantially to the intensity at point P. In (b), horizontal-pass spatial filtering broadens the PSF in the vertical direction, which leads to an increased number of pixels contributing to the intensity at point P′.

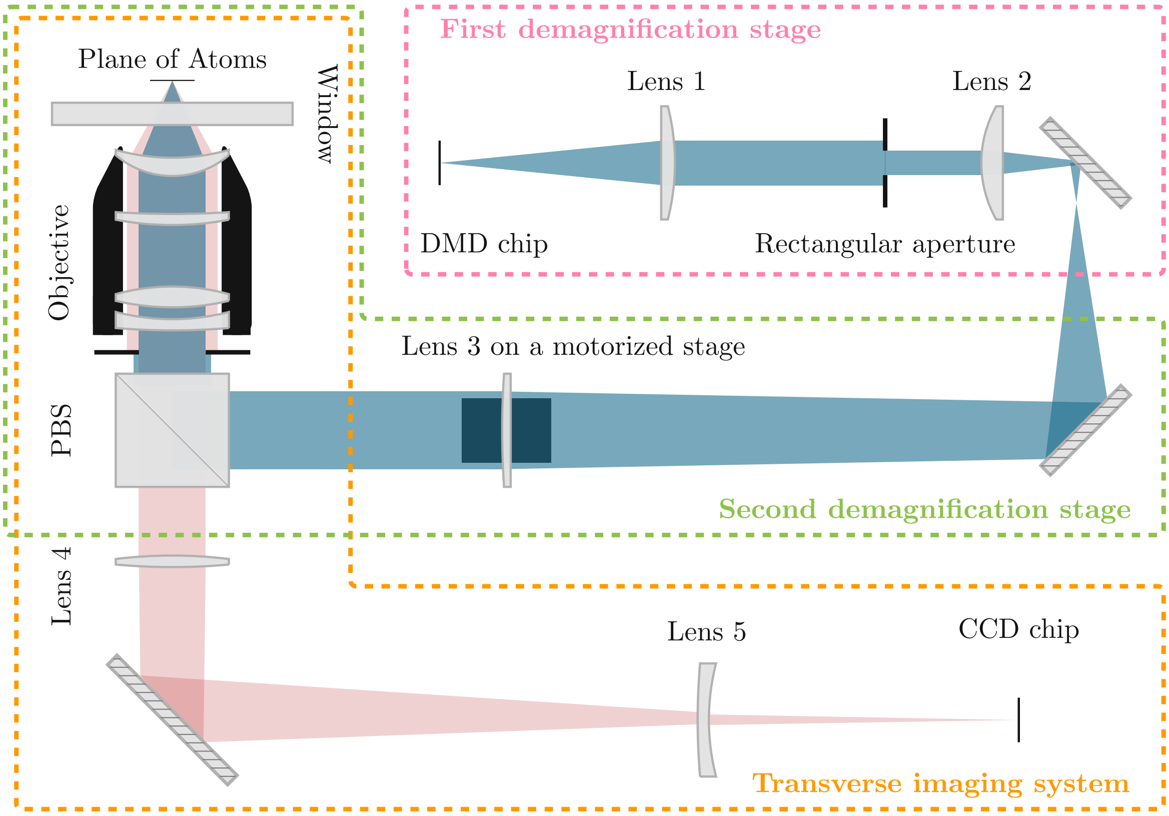
First demagnification stage
Lens 1
Lens 2
DMD chip
Rectangular aperture
Plane of Atoms
Window
Objective
PBS
Lens 3 on a motorized stage
Second demagnification stage
Lens 4
Lens 5
CCD chip
Transverse imaging system

Figure 4.4 Integration of the optical setup for DMD-shaped dipole potentials into the transverse imaging system (TIS). In the first demagnification stage, lens 1 ("Thorlabs LA1256-B") and lens 2 ("Thorlabs LA1050-B") form a 4f system connected to the second demagnification stage by two mirrors. The first mirror has its backside polished and an overview camera placed behind it to observe the DMD pattern (not shown). Lens 3 ("Thorlabs LA1727-B"), together with the objective of the TIS, forms the second demagnification stage. This lens can be shifted with a motorized stage to adjust the focus of the DMD imaging system in the plane of atoms. The dipole trap path is then superimposed on the imaging path on a polarizing beamsplitter (PBS) cube. While the p-polarized imaging light, $\lambda = 780\,\text{nm}$ (pink), passes through the PBS cube, the s-polarized optical trap light, $\lambda = 660\,\text{nm}$ (blue) is reflected into the home-built diffraction limited objective of the TIS. The objective consists of four commercially available lenses ("Thorlabs LE1527, LE1359, AC508-150-B, and LF1129") with a NA of 0.26 [12]. The imaging beam is focused on the CCD chip via lens 4 ("Thorlabs AC508-400-B") and lens 5 ("Thorlabs LF1764"), forming a telephoto group to shrink the size of the optical system.

the experiment (see Fig. 4.4), which favors wavelengths ranging from 650 to 1150 nm. Being far-detuned from the resonance guarantees that for $V_{\mathrm{dip}}/\hbar \sim 2\pi \times 1\,\mathrm{kHz}$ the scattering rate is $\sim 2\pi \times 0.1\,\mathrm{mHz}$. This leads to only one spontaneous scattering per second for an ensemble of 10^4 atoms, causing negligible atom loss and heating.

We apply the concepts discussed in the previous section by imaging DMD patterns directly onto the plane of atoms. Our DMD chip is a DLP9500 from "Texas Instruments" with 1080×1920 micro-mirrors, each $10.8 \times 10.8\,\mu\mathrm{m}$. The refresh rate for the whole array is 17 kHz, which increases to 50 kHz when the number of active rows is limited to 50. The DMD chip is a part of the "V-9501" module by "ViALUX". This module also contains a "V4395" main board with a completely configured high-speed FPGA logic and firmware.

The optical setup imaging DMD patterns onto the plane of atoms is shown in fig. 4.4. It consists of two demagnification stages: First, a 4f system performs horizontal-pass spatial filtering using an adjustable rectangular slit. Secondly, a plano-convex lens, along with the objective of the TIS, images the DMD pattern onto the plane of atoms.

The DMD chip is placed at the focal point of the first lens, and the distance between lens 1 and lens 2 is the sum of the two focal lengths, $f_1 + f_2 = 30\,\mathrm{cm} + 10\,\mathrm{cm} = 40\,\mathrm{cm}$. The width of the rectangular slit sitting in the Fourier plane of the system can be adjusted independently in the vertical and horizontal directions from 0 to 12 mm. The image formed by the first two lenses is further demagnified by lens 3 and the objective of the TIS. The focus of the whole system is adjusted by lens 3, which is mounted on a motorized stage. This is necessary such that the TIS and the dipole light can be focused independently. The total magnification of the DMD imaging system is 1/25.9, and it has a minimum spot size (Airy diameter) of $4\,\mu\mathrm{m}$ in the plane of atoms. This implies that more than 70 DMD pixels contribute to the Airy disk at a single spot. The DMD chip is illuminated by a Gaussian beam whose horizontal extension is elongated by a cylindrical telescope. This is done to match the available intensity to the cloud's size and efficiently use the available power. The polarization of the dipole potential beam is also set such that the beam gets reflected in the PBS cube in the second demagnification stage with minimal loss. For more information on the beam preparation and alignment of the setup, please refer to **Tajik-Thesis**.

4.3.3 Calibration

Before initiating the pattern optimization, a calibration procedure is performed to determine the corresponding positions in the atomic plane to the various DMD pixels in the horizontal and vertical directions. For horizontal (longitudinal) calibration, multiple

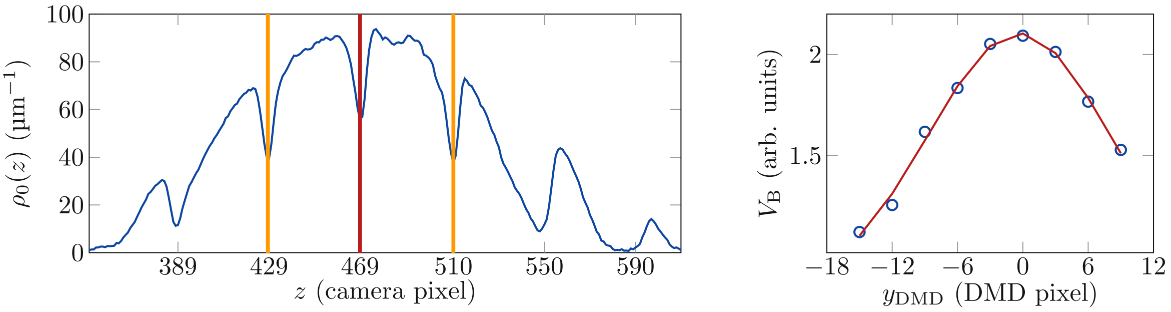

(a) **(b)**

Figure 4.5 An example of data used for horizontal (longitudinal) calibration and vertical calibration. (a) multiple super pixels (190 × 3 pixels) are turned on 100 DMD pixels apart from each other. The red vertical line corresponds to the image of the superpixel in the center of the DMD pattern. The distance between two orange lines and the position of the red line can be used for a linear mapping between DMD pixels and corresponding camera pixels. **(b)** Height of the barrier (V_{B}) created by a superpixel (3 × 15 pixels) is plotted for different vertical positions of the superpixel on the DMD pattern. The row $y_{\mathrm{DMD}} = 0$ is the central DMD row. The blue circles represent the data taken from $y_{\mathrm{DMD}} = -15$ to 9 with steps of 3 DMD pixels, and the red curve is a Gaussian fit.

DMD columns are activated at different positions, and their positions are detected on the 1D density profile, allowing for the derivation of a linear mapping between the position of the cloud and the DMD pixels(fig. 4.5(a)). For vertical calibration, a simple barrier is created using a thin superpixel in the center of the atomic cloud, with the height of the barrier being adjusted by vertically shifting this superpixel. The central row of the DMD pattern is selected at the position where the barrier height is maximum (fig. 4.5(b)). This central row corresponds to the position of the elongated atomic cloud ($y = y_{\mathrm{cloud}}$) in the atomic plane and contributes the most to $I(z)$. The vertical calibration also defines the vertical boundaries of the area of interest (AOI), the area outside which the DMD pixels do not contribute to $I(z)$.

4.3.4 Closed-loop pattern optimization

Using the optical setup described in section 4.3.2, AOI on the DMD chip containing $n_y \times n_z$ pixels (typically 20 × 500 pixels for a 200 µm long 1D trap) is projected onto the atomic plane. These pixels allow $2^{n_y \times n_z}$ different patterns to be generated. The challenge lies in finding a pattern that produces a 1D optical dipole potential, which, when combined with the magnetic confinement of the atom chip, creates the desired

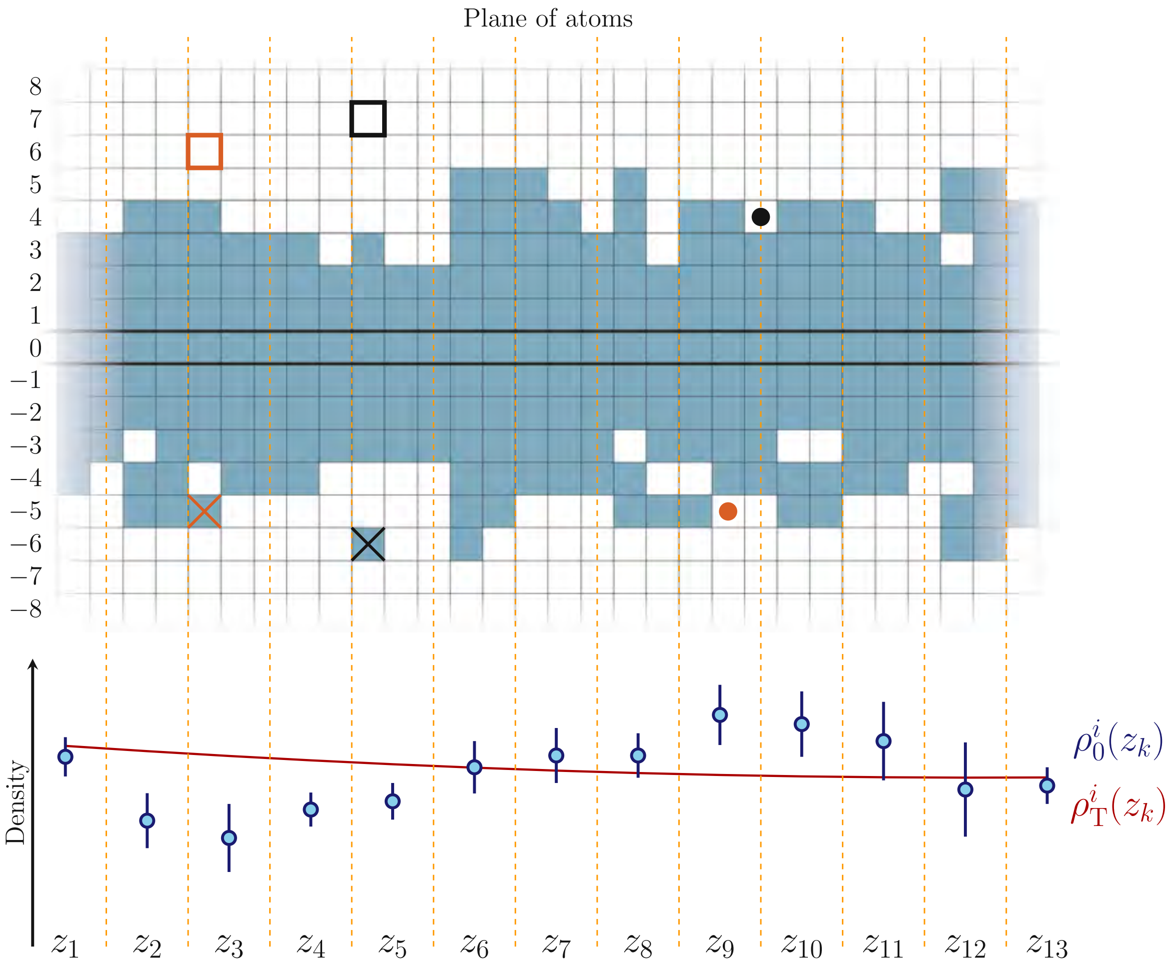
Plane of atoms
8
7
6
5
4
3
2
1
0
−1
−2
−3
−4
−5
−6
−7
−8
Density
z_1
z_2
z_3
z_4
z_5
z_6
z_7
z_8
z_9
z_{10}
z_{11}
z_{12}
z_{13}
$\rho_0^i(z_k)$
$\rho_\mathrm{T}^i(z_k)$

Figure 4.6 An example step of DMD pattern update process. Updating the DMD pattern based on the comparison between the averaged measured density, $\rho_0^i(z_k)$, and the target density, $\rho_T^i(z_k)$. The process is explained in detail in 4.3.4. The example here shows a small longitudinal segment of iteration number $i = 14$ of the optimization leading to the results shown in Fig. 4.7(c). The region on the DMD corresponds to an interval $z_1 = -39.89\,\mu\text{m}$ to $z_{13} = -26.23\,\mu\text{m}$.

target potential $V_\mathrm{T}(z)$. While it is possible to numerically calculate the 2D image of the DMD pattern and design it to achieve the desired potential, the actual dipole potential is sensitive to the precise alignment of optical elements and setup imperfections, making it difficult to predict accurately in a real-world setting. Therefore, an iterative pattern optimization process is employed to achieve the best possible reconstruction of the target potential.

In the experiment, we measure density profiles $\rho(z_k)$ as described in section 3.2.2, where the spatial grid z_k corresponds to the camera pixels in the plane of atoms. Hence, the primary objective of the pattern optimization is to find a DMD pattern that creates a 1D density profile $\rho(z_k)$ that closely matches a simulated target density $\rho_\mathrm{T}(z_k)$. The target density is obtained by solving the ground state of a 1D non-polynomial Schrödinger equation (NPSE) [77] with the external target potential $V_\mathrm{T}(z_k)$.

The optimization process for the DMD pattern begins by selecting an initial pattern p^0, which can be either completely black (all DMD pixels turned off), or a pattern from a previous optimization process.

At each iteration, i, using the DMD pattern p^i, the average 1D density profile $\rho_0^i(z_k) = \langle \rho(z_k) \rangle$ and the mean atom number $\bar{N}^i$ are obtained from n images. The mean atom number $\bar{N}^i$ is then used to calculate the target density $\rho_\mathrm{T}^i(z_k)$.

To assess the agreement between the measured averaged density $\rho_0^i(z_k)$ and the calculated target density $\rho_\mathrm{T}^i(z_k)$, we compute the normalized root-mean-square deviation given by

$$\epsilon_\mathrm{RMS}^i = \sqrt{\frac{1}{j-l} \sum_{k=j}^{l} \left(\frac{\rho_\mathrm{T}^i(z_k) - \rho_0^i(z_k)}{\rho_\mathrm{T}^i(z_k)} \right)^2}, \tag{4.10}$$

for a specific region from z_j to z_l, and compare it to a target value ϵ_T. The required quality for a specific target potential depends on the application. However, a lower limit for ϵ_T is determined by the noise in the density measurement. ϵ_T should not be smaller than the average standard error of the mean density σ_{ρ_0} in the same region.

The optimization process is terminated when $\epsilon_\mathrm{RMS}^i < \epsilon_\mathrm{T}$. In this case, the final DMD pattern is given by p^i. If $\epsilon_\mathrm{RMS}^i \geq \epsilon_\mathrm{T}$, a new pattern p^{i+1} is generated using the update procedure discussed below.

In the DMD pattern update procedure, the states of individual pixels are modified based on the difference between $\rho_0^i(z_k)$ and $\rho_T^i(z_k)$. More pixels are activated in regions where the measured density is higher than the target density, resulting in a locally higher potential. Conversely, deactivating pixels or shifting active pixels away from the center reduces the optical dipole potential in the corresponding region, leading to higher densities.

This process relies on the one-to-one correspondence between the trapping potential and the density distribution in the Thomas-Fermi approximation,

$$V(z) = \mu - \frac{g_{3\mathrm{D}}}{2\pi a_\perp^2} \frac{\rho_0(z)}{\sqrt{1+2a_\mathrm{s}\rho_0(z)}} - \frac{\hbar\omega_\perp}{2}\left(\sqrt{1+2a_\mathrm{s}\rho_0(z)} + \frac{1}{\sqrt{1+2a_\mathrm{s}\rho_0(z)}}\right) , \quad (4.11)$$

where a_s is the s-wave scattering length, $g_{3\mathrm{D}} = 4\pi\hbar^2 a_\mathrm{s}/m$ is the 3D, and μ is the chemical potential acting as an offset. For a fixed number of atoms, locally increasing/decreasing the potential decreases/increases the local density distribution.

Fig. 4.6 illustrates the mapping of seventeen rows of the DMD chip onto the plane of atoms, where the central row is denoted as the zeroth row. The orange dashed lines represent the horizontal position of the camera pixels mapped onto the plane of atoms, defining the spatial grid points z_k. The length of each grid point ($1.05\,\mu$m) corresponds to the length of approximately 2.5 DMD pixels mapped onto the plane of atoms ($2.5 \times 10.8\,\mu\mathrm{m}/25.9 = 1.04\,\mu$m).

For each grid point z_k, the corresponding region on the DMD chip remains unchanged if $|\rho_0^i(z_k) - \rho_T^i(z_k)| < \sigma_{\rho_0}^i(z_k)$, where $\sigma_{\rho_0}^i(z_k)$ represents the standard error of the mean density, indicated by the error bars in the figure. In this example, this condition holds true for z_1, z_6, z_7, z_8, z_{11}, z_{12}, and z_{13}. In cases where $|\rho_0^i(z_k) - \rho_T^i(z_k)| > \sigma_{\rho_0}^i(z_k)$, the magnitude of the total deviation determines how many pixels corresponding to the grid point z_k will be changed.

If $\rho_0^i(z_k) - \sigma_{\rho_0}^i(z_k) > \rho_T^i(z_k)$, the potential needs to be increased by turning on additional pixels. To determine these pixels, the distances of the outermost active pixels for the columns involved are compared, and the column with the smallest distance is selected. For example, consider the three columns involved in the region defined by z_{10}: The maximum distance of an active pixel from the central row is only 4 for the left column, while for the central and right columns, this number is 5. Therefore, the left column will be chosen in this case. In the selected column, if the outermost pixel is located below the central row, the pixel above the central row that is one row further away will be turned on. If the outermost pixel is above the central row, the pixel with the same distance but below the central row will be turned on. For z_{10}, the pixel marked with a black dot will be turned on. Similarly, for z_9, the pixel marked by an orange dot will be turned on.

On the other hand, if $\rho_0^i(z_k) + \sigma_{\rho_0}^i(z_k) < \rho_T^i(z_k)$, the potential needs to be decreased by shifting the outermost pixel away from the central row in each region. For example, in the region corresponding to z_3 (z_5), the pixel in row number -5 (-6) will be shifted to row number 6 (7) in the same column, as indicated in Figure 4.6. In principle, the pixel −5 (−6) could also be shifted to row −6 (−7). Although the results may differ due to interference, the choice between the two options is arbitrary. If the selected pixel is located at the border of the AOI, it will be turned off.

4.3.5 Examples

A few examples of closed-loop pattern optimization The results are presented in fig. 4.7. For each example, the optimization process started with different initial DMD patterns. In the first and fourth examples (fig. 4.7(a) and fig. 4.7(d)), all DMD pixels were turned off initially. Consequently, the initial density profiles (potential) plotted in fig. 4.7(a) and fig. 4.7(d) (in orange) represent the 1D magnetic potential. In contrast, for the examples shown in fig. 4.7(b) and fig. 4.7(c), we utilized a previously optimized DMD pattern as the starting point for the optimization process. All the potentials plotted in fig. 4.7, are obtained using the NPSE for 1D condensates [77] introduced in eq. (4.11).

In the presented examples, the number of experimental realizations needed to compute ρ_0^i was adjusted in each iteration based on the normalized root-mean-squared deviation from the previous step. This approach speeds up the optimization process, particularly in the initial stages, where only a rough density measurement is required. Initially, only two experimental shots ($n = 2$) were used to calculate the averaged 1D density and the mean atom number. As the optimization progressed, this number increased to five images ($n = 5$) and ten shots ($n = 10$) accordingly.

During the entire optimization process, the optical dipole trap was activated while evaporative cooling in a transverse double-well potential. After a short expansion time of 2 ms, absorption images were taken to obtain the density profiles.

The normalized root-mean-squared deviation for different examples in each iteration, $\epsilon^i_{\mathrm{RMS}}$, is plotted in fig. 4.8. The number of iterations required to meet the termination criterion varied depending on the initial and target potentials. For instance, modifying an existing box-like potential (adding a barrier) generally requires fewer iterations than achieving a box-like potential starting from a harmonic potential. The total optimization time for these examples was from 60 to 135 minutes.

To assess the stability of the achieved potentials after optimization, $\epsilon^i_{\mathrm{RMS}}$ is plotted over more than six hours in fig. 4.9(a). In this case, the optimization process stopped after 40 iterations and the resulting pattern remained unchanged throughout the rest of the measurement. fig. 4.9(b) shows the agreement between normalized densities measured immediately after the optimization stopped (orange curve) and those obtained after 200 minutes (green curve) and 400 minutes (blue curve).

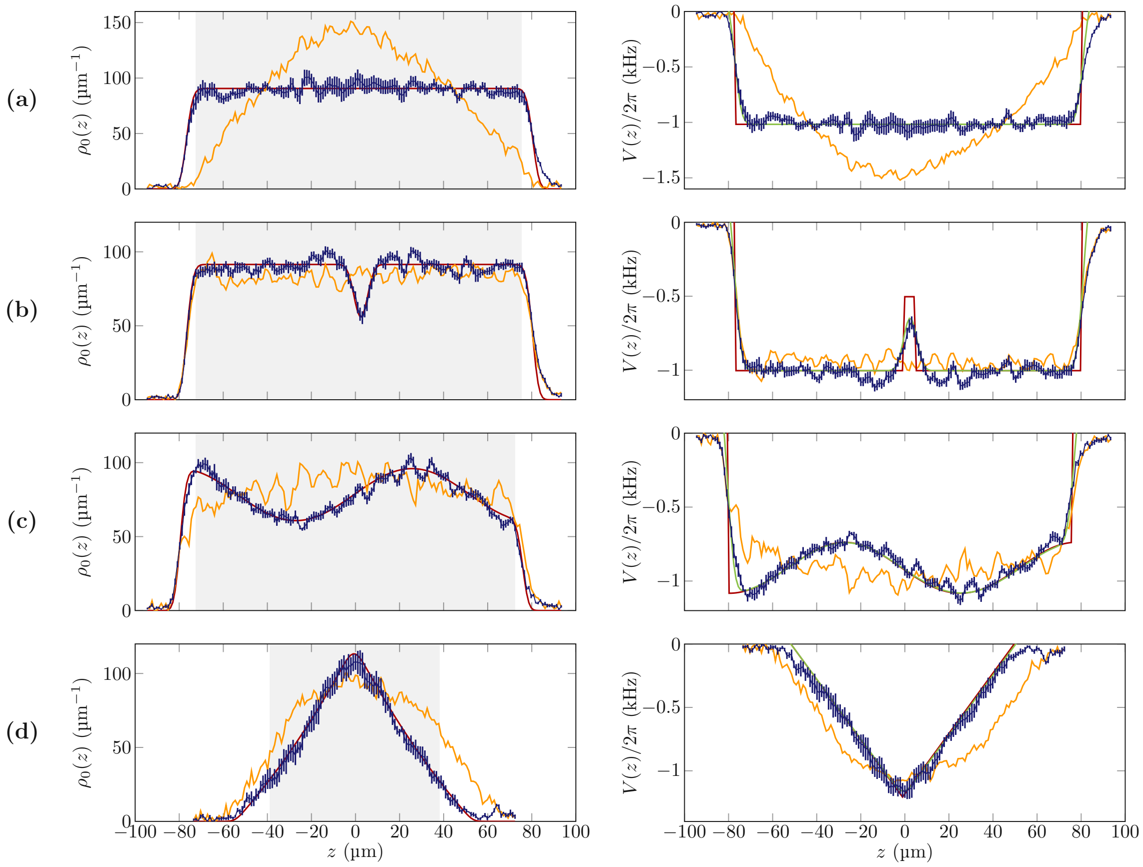

Figure 4.7 Examples of the closed-loop pattern optimization. Results for four different target potentials: **(a)** a box-like potential with length $L = 160\,\mu\mathrm{m}$, **(b)** two box-like potentials separated by a barrier, **(c)** a $L = 160\,\mu\mathrm{m}$ box-like potential with a sinusoidally modulated bottom and **(d)** a V-shaped potential. In the left (right) column, orange curves are averaged initial 1D densities (potentials), red curves are target densities (potentials), and blue curves are averaged 1D density profiles (potentials) and their standard errors for optimized patterns. The green curves in the right column are the target potentials broadened by the DMD imaging system. The measured potentials show a good agreement with these broadened target potentials. Note that the scale of the density (potential) axis is not the same for different cases. For the final density profiles, ϵ_{RMS} calculated over the gray shaded region is **(a)** 4.4%, **(b)** 5.5%, **(c)** 4.2% and **(d)** 5.9%. For **(b)**, the optimization process started with the optimized pattern achieved in **(a)**. For **(c)**, the optimization started with an older optimized pattern for a box-like potential with a slightly different calibration setting. In **(a)** and **(d)**, however, the optimization process started with a pattern in which all DMD pixels were off, i.e., orange curves in **(a)** and **(d)** represent our longitudinal magnetic potential when the condensate is split transversally in a double-well. Since the measured density for the first iteration is only averaged over two experimental realizations, the effect of shot noise is evident in the orange curves.

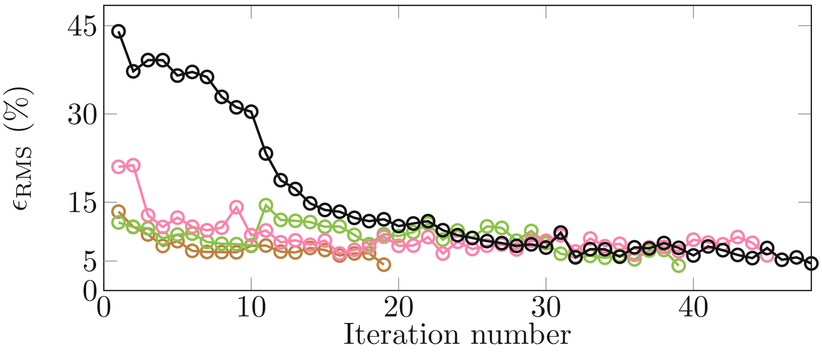

Figure 4.8 Evolution of the RMS error. ϵ_{RMS} is plotted over iteration number for three different cases (lines are guides to the eye): A box-like potential with length $L = 160\,\mu\mathrm{m}$ (black), two box-like potentials separated by a barrier (brown), a box-like potential with a sinusoidally modulated bottom (green) and a V-shaped potential (pink). All initial and final densities and potentials are plotted in fig. 4.7(a-d).

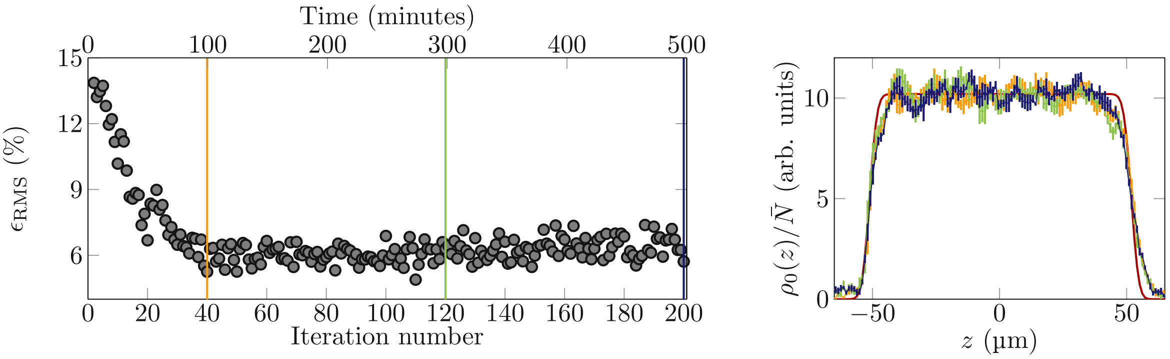

(a) **(b)**

Figure 4.9 Stability measurement (a) Evolution of ϵ_{RMS} before and after optimization for a box-like potential with length $L = 100\,\mu\mathrm{m}$. The horizontal axis on the top is the time corresponding to different iterations. The optimization stopped at iteration number 40 (orange line), and the DMD pattern remained unchanged throughout the measurement. **(b)** Normalized target density (red), normalized density profiles for iteration numbers 40 (orange), 120 (green), and 200 (blue) are plotted.

4.4 Outlook

In this chapter, we discussed the trapping schemes on an atom chip setup. We showed that we can create arbitrary 1D confinements in single or double well potentials. The closed-loop optimization process discussed here is the first attempt to design DMD patterns to create a desired intensity profile in the plane of atoms. Although this method has proven functional in various settings, optimizing dynamic potential requires faster optimization. With our colleagues, who are experts in optimal control, we have shown that *iterative learning control* can be applied to DMD pattern optimization to achieve faster convergent to desired potentials [78]. Our groupmates have used these methods in a novel DMD setup with an improved illumination and optimization method [79].

Implementation of arbitrary potentials presents numerous opportunities for conducting experiments with 1D quantum systems. The use of a box-like potential enables the creation of homogeneous systems, and the addition of barriers allows for longitudinal splitting and tunneling. By switching between different DMD patterns, quench experiments become possible. For instance, imprinting a density modulation corresponding to a specific mode's density quadrature allowed us to observe Pauli-Blocking [18, 40] in 1D condensates and investigate the evolution and decay of such excitations beyond effective field theories [80]. Moreover, DMD patterns can be changed more rapidly than the typical time scales of the one-dimensional quantum gas, allowing for the implementation of time-varying potentials. This capability opens the door to exploring various applications, including the construction and investigation of quantum field machines [41, 81, 82]. Overall, our system offers a versatile and powerful platform for advancing research in the realm of one-dimensional quantum systems.

Chapter 5

Verification of the area law of mutual information

Quantifying correlations in equilibrium

In this chapter, I briefly point out the importance of quantum information measures in quantum many-body systems and quantum field theory. I then introduce two of the renowned measures, namely von Neumann entropy and quantum mutual information. I will then focus on the Gaussian states and demonstrate how these measures are calculated for these states. Afterward, I will discuss the experimental techniques to measure these quantities in our quantum field simulator introduced in chapter 3. Finally, I present our results demonstrating the volume law of von Neumann entropy and the area law of quantum mutual information. Parts of this chapter have been published in [44], with some parts having substantial overlap, and others being borrowed verbatim.

5.1 Quantum information measures in many-body systems

Quantum field theories serve as one of the pillars in modern theoretical physics, providing a framework to describe physical systems, from fundamental particles to condensed matter and cosmology. In the quest to understand the complexities of quantum systems, the field of quantum information has emerged as a powerful and indispensable tool [83]. By focusing on the unique properties of quantum states and the entanglement that arises between them, quantum information theory has opened up new avenues for gaining deeper insights into the behavior of quantum many-body systems.

One of the key aspects that make quantum information theory indispensable in the study of quantum field theories is the ability to quantify and characterize correlations. In this regard, quantum information measures play a pivotal role. The von Neumann entropy, for instance, serves as a fundamental measure of the amount of entanglement present in a quantum state [84, 85]. It provides essential information about the purity of the state and the distribution of its quantum information across different subsystems.

Mutual information, another crucial quantum information measure, goes beyond merely quantifying entanglement in individual subsystems. It captures the correlations between different subsystems, revealing how they share information and influence each other's properties [86]. By studying mutual information in the context of quantum field theories, researchers gain insights into the complex interplay of quantum and classical correlations in extended systems.

Furthermore, information theory measures have revealed a fundamental property of quantum many-body systems known as area laws [87, 88]. This concept stems from gravitational physics where it was surprisingly found that the entropy of a black hole is proportional to the surface area of its event horizon rather than its volume [89]. Interestingly, a similar property was discovered in quantum many-body systems: the von Neumann entropy of ground states for systems with gapped Hamiltonians scales with the surface area of the subsystem rather than its volume [88]. Furthermore, this property extends to thermal states of systems with a gapped Hamiltonian, exhibiting an area law of mutual information [86]. This implies that the information shared between different parts of a quantum many-body system is significant only over a short distance, determined by the correlation length.

5.2 Von Neumann entropy and mutual information

One of the challenges in quantum information is to find a suitable quantum information quantity from the zoo of available measures and witnesses [83]. The choice of the proper measure or witness heavily depends on the physical system under investigation and, of course, the available information and observables related to the system. In experimental settings, the challenge is more prominent, where not only the available observables are limited, but even those are usually affected by experimental imperfections [90–93]. Often experimentalist work side by side with theorists to find or design a witness suiting the experimental system or develop novel experimental tricks and techniques to measure a quantum information quantity. Even when the state of a system is entirely determined, and the density matrix is known, there are quantum information quantities that require extensive calculations -often optimizations of some sort- that make them non-applicable in many practical scenarios. An example would be the quantum discord for many mode Gaussian states [94].

As mentioned in section 3.3.2, we have direct access to one of the relative field quadratures, namely the relative phase field and its higher correlations. Later in this chapter (section 5.5.3), I will explain a tomography process that allows us to indirectly measure the second-order density-density and phase-density correlations. This procedure grants us access to the full density matrix for Gaussian states, which we will discuss in section 5.3.

With the density matrix at hand, we can calculate several interesting quantum information measures that help us gain insight into the properties of our state and quantify the amount of information. It is easier to discuss the relevance of these quantities once they are introduced and explained. We start with a basic quantity, yet the most famous and prominent of them all: The von Neumann entropy.

5.2.1 Von Neumann entropy

Here, I will give a basic pedagogical introduction to von Neumann entropy for readers like myself, who are not used to the language of quantum information. Von Neumann entropy is the quantum mechanical counterpart of the famous Gibbs entropy in statistical physics. For a classical system with Ω microstates, each with energy E_i and probability p_i, the Gibbs entropy reads

$$S_{\mathrm{Gibbs}} = k_{\mathrm{B}} \sum_{i=1}^{\Omega} p_i \ln(p_i) \ . \tag{5.1}$$

Here, $k_{\mathrm{B}} = 1.38 \times 10^{-23}\,\mathrm{JK}^{-1}$ is a physical constant, known as the Boltzmann constant, that matches the units of S_{Gibbs} with the thermodynamic entropy, $dS_{thermo} = \delta Q/T$. In this manuscript, we will write entropies in units of k_{B}, and we use natural logarithm ($\ln \equiv \log_e$). Shannon later adopted the concept of entropy in the information theory to quantify the "ignorance" regarding possible outcomes of a random process, given the probability distribution. The example below clarifies this concept.

Example 5.1. Let's calculate the (Shannon) entropy for a coin toss when (1) the coin is "fair", i.e., $p_{\mathrm{H}} = p_{\mathrm{T}} = 1/2$, (2) the coin is "unfair", $p_{\mathrm{H}} = 1/4$, $p_{\mathrm{T}} = 3/4$, and the coin is "totally unfair", $p_{\mathrm{H}} = 0$, $p_{\mathrm{T}} = 1$.

$$\begin{aligned}
&(1)\ S_{\mathrm{Gibbs}} = -\frac{1}{2}\ln\left(\frac{1}{2}\right) - \frac{1}{2}\ln\left(\frac{1}{2}\right) = \ln 2 = 0.69\\
&(2)\ S_{\mathrm{Gibbs}} = -\frac{1}{4}\ln\left(\frac{1}{4}\right) - \frac{3}{4}\ln\left(\frac{3}{4}\right) = 0.56\\
&(3)\ S_{\mathrm{Gibbs}} = -0 \times \ln(0) - \ln(1) = 0
\end{aligned}$$

The results revealed the beauty of entropy as a measure of ignorance: For the state that we a priori know the outcome, our "ignorance" is zero. On the other hand, when the outcome of the coin toss is totally random, our ignorance is the largest. In fact, as a nice exercise, one can show that the famous Boltzmann's entropy,

$$S_{\mathrm{Boltzmann}} = k_{\mathrm{B}} \ln(\Omega)\,, \tag{5.2}$$

can be derived by maximizing the Gibbs entropy, under the constraint that the sum of all probabilities has to add to one, $\sum_{i=1}^{\Omega} p_i = 1$.

Having this interpretation in mind, we are ready to introduce a quantum version of entropy. Given a quantum system whose state is described by a density matrix ϱ, the von Neumann (vN) entropy is defined as

$$S = -\operatorname{Tr}(\varrho \ln(\varrho))\,. \tag{5.3}$$

Note that we reserve the capital S without a subscript for vN entropy throughout the manuscript. The form of vN entropy is very similar to the classical counterparts, and the interpretation is too. There is a subtle and essential difference here. The vN entropy does not tell us anything about the intrinsic ignorance encoded in a quantum state but rather the statistical ignorance of which state the system is actually in. It quantifies how statistically *mixed* our state is. These last few sentences are difficult to understand without giving a few examples.

Example 5.2. Let's calculate the vN entropy and the purity, $\mathrm{Tr}(\varrho^2)$ of $\varrho = \sum_i^N p_i \left|\psi_i\right\rangle \left\langle\psi_i\right|$, with $|\psi_1\rangle = (|0\rangle + |1\rangle)/\sqrt{2}$ and $|\psi_2\rangle = (|0\rangle - |1\rangle)/\sqrt{2}$ when (1) $p_1 = p_2 = 1/2$, (2) $p_1 = 1/4$, $p_2 = 3/4$, and finally, $p_1 = 0$, $p_2 = 1$.

To calculate the vN entropy, it is convenient to first find the eigenvalues of ϱ, $\{\lambda_i\}$ and write the vN entropy as

$$S = -\sum_i \lambda_i \ln \lambda_i\ .$$

Writing ϱ in basis of $|i\rangle\langle j|$, with $i,j=0,1$ yields

$$(1)\ \varrho=\begin{pmatrix}\frac{1}{2} & 0\\ 0 & \frac{1}{2}\end{pmatrix},\quad \lambda_1=\frac{1}{2},\ \lambda_2=\frac{1}{2}\Rightarrow S=\ln 2=0.69\ ,$$

$$(2)\ \varrho=\begin{pmatrix}\frac{1}{2} & -\frac{1}{4}\\ -\frac{1}{4} & \frac{1}{2}\end{pmatrix},\quad \lambda_1=\frac{1}{4},\ \lambda_2=\frac{3}{4}\Rightarrow S=2\ln 2-\frac{3}{4}\ln 3=0.56\ ,$$

$$(3)\ \varrho=\begin{pmatrix}\frac{1}{2} & -\frac{1}{2}\\ -\frac{1}{2} & \frac{1}{2}\end{pmatrix},\quad \lambda_1=1,\ \lambda_2=0\Rightarrow S=0\ .$$

We then calculate the purities:

$$(1)\ \mathrm{Tr}\Big(\varrho^2\Big)=\frac{1}{2},\quad (2)\ \mathrm{Tr}\Big(\varrho^2\Big)=\frac{5}{8}=0.625,\quad (3)\ \mathrm{Tr}\Big(\varrho^2\Big)=1$$

As the results suggest, similar to $\mathrm{Tr}(\varrho^2)$, vN entropy is also measuring how mixed our state is. For a pure state like (3), vN entropy is zero, and for a maximally mixed state such as (1), we get $\ln\Omega$, where Ω is the dimension of the Hilbert space in this case.

This example showed that even for p_1 or p_2 equal to zero, our state $|\psi\rangle$ is in a superposition, and our ignorance about a measurement outcome that stems from the quantum mechanical nature of the state is preserved. Although vN entropy is a measure of purity, other aspects make it an important quantity in quantum information: First, for pure states, the vN entropy of subsystems is a measure of entanglement. It is called *entanglement entropy*. Second, other interesting quantities are defined based on or can be calculated using vN entropy. Later we will discuss mutual information as an example.

Entanglement entropy

In a multi-partite system, the von Neumann entropy of a subsystem A is calculated using the reduced density matrix associated with A, namely $\varrho_A = \mathrm{Tr}_{A^{\mathrm{C}}}(\varrho)$, where A^{C} (A complement) denotes the rest of the system and ϱ is the density matrix of the whole system.

Example 5.3. Let's calculate S and S_A for a Bell state $|\psi^+\rangle=(|0\rangle_A|1\rangle_B+|1\rangle_A|0\rangle_B)/\sqrt{2}$.

Similar to the previous example, we first write $\varrho = |\psi^+\rangle\langle\psi^+|$ as a matrix and calculate the eigenvalues to calculate S,

$$\varrho = \frac{1}{2}\begin{pmatrix} 0 & 0 & 0 & 0 \\ 0 & 1 & 1 & 0 \\ 0 & 1 & 1 & 0 \\ 0 & 0 & 0 & 0 \end{pmatrix}, \quad \lambda_1 = 1,\ \lambda_{2,3,4} = 0 \Rightarrow S = 0\ .$$

Now, we calculate $\varrho_A = \mathrm{Tr}_B(\varrho) = \sum_{i=0,1} \langle i|_B\, \varrho\, |i\rangle_B$,

$$\varrho_A = \begin{pmatrix} \frac{1}{2} & 0 \\ 0 & \frac{1}{2} \end{pmatrix}, \quad \lambda_1 = \frac{1}{2},\ \lambda_2 = \frac{1}{2} \Rightarrow S_A = \ln 2 = 0.69\ .$$

As we expected for a pure state, S vanishes. But the state of the subsystem looks like a maximally mixed state, which is interpreted as *maximally entangled* when the full state is pure. If we consider $|\psi\rangle = |0\rangle_A |1\rangle_B$, which is pure and separable, we will see that both S and S_A vanish, suggesting that the state is not entangled.

Rényi entropy

Rényi entropy is a generalized form of von Neumann entropy. For a subsystem A with a reduced density matrix ϱ_A, the Rényi-α entropy is defined as

$$S^{(\alpha)} = \frac{1}{1-\alpha} \ln(\mathrm{Tr}(\varrho_A^\alpha))\,, \tag{5.4}$$

where α is defined over $(0,1) \cup (1,\infty)$. In the limit of $\alpha \to 1$, the Rényi-1 entropy converges to vN entropy. If the density matrix of a quantum system is given, the vN entropy and Rényi entropies can be calculated. However, in settings where the density matrix is not directly accessible, but instead the purity, $\mathrm{Tr}(\varrho)$, can be measured, Rényi-2 entropy has proven extremely useful [91, 93].

5.2.2 Quantum mutual information

Quantum mutual information between two subsystems of a multi-partite quantum system say A and B, is a measure of the total correlation between the two parts and is defined as

$$I(A:B) = S_A + S_B - S_{A\cup B}\,. \tag{5.5}$$

Note that the difference between mutual information and quantum mutual information is the entropy used in eq. (5.5). We use the abbreviation MI for quantum mutual information throughout the manuscript. In the context of mixed states, MI has proven to be a useful quantity: It is a measure of the total amount of information and quantifies classical and quantum correlations. It also manifests an area law at finite temperatures that can be rigorously proven. Moreover, one can rigorously show that a system with finite correlation length fulfills an area law. Another feature of MI is that in the limit of zero temperature (pure states), it coincides with the entanglement entropy for the subsystem. To show this, we calculate the MI of a subsystem A with the rest of the system, A^{C}. Using eq. (5.5) with $B = A^{\mathrm{C}}$ we get

$$I(A : A^{\mathrm{C}}) = S_A + S_{A^{\mathrm{C}}} - S_{A \cup A^{\mathrm{C}}} \,. \tag{5.6}$$

For a pure state, the entropy of the total system is equal to zero, $S_{A \cup A^{\mathrm{C}}} = 0$.

Example 5.4. Let's calculate $I(A : B)$ for (1) $|\psi^+\rangle = (|0\rangle_A |1\rangle_B + |1\rangle_A |0\rangle_B)/\sqrt{2}$ and (2) $|\psi\rangle = |0\rangle_A |1\rangle_B$.

Using the results of example 5.3,

$$\begin{aligned} &(1)\ S = 0, S_A = S_B = \ln 2 \Rightarrow I(A : B) = S_A + S_B - S = 2 \ln 2 \\ &(2)\ S = 0, S_A = S_B = 0 \Rightarrow I(A : B) = S_A + S_B - S = 0 \,. \end{aligned}$$

In an entangled system, we see that the shared information between subsystems is nonzero, which is not the case for the separable state in (2).

Having tens of thousands of atoms at finite temperatures in our experiment makes MI an interesting quantum information object and a solid measure to quantify the correlations between different regions. In the following, we will prepare the stage to present our measurements, verifying the area law of MI.

5.3 Quantum information measures for Gaussian states

As we will see in section 5.4.2, the thermal equilibrium states of Klein-Gordon Hamiltonian are Gaussian states. These states are an important set of states, that play an important role in quantum field theory and continuous-variable quantum computation [95]. As a reminder, our field quadrature operators are phase, $\hat{\varphi}$, and density fluctuations, $\delta\hat{\rho}$, with canonical commutation relations

$$[\hat{\varphi}(z), \delta\hat{\rho}(z')] = \mathrm{i}\delta(z - z')\,, \qquad [\hat{\varphi}(z), \hat{\varphi}(z')] = 0\,, \qquad [\delta\hat{\rho}(z), \delta\hat{\rho}(z')] = 0\,, \tag{5.7}$$

where $\delta(z - z')$ is the Dirac delta distribution. Since we are dealing with a finite number of modes in the experiment, we use the discretized version of this commutation relation that reads

$$[\hat{\varphi}(z_n), \delta\hat{\rho}(z_m)] = \frac{\mathrm{i}}{\Delta z}\delta_{nm}\,. \tag{5.8}$$

Here, $\Delta z = z_{n+1} - z_n$ is the grid spacing and δ_{nm} represents the Kronecker delta.

By definition, only the first and second moments of the field quadratures are needed to describe a Gaussian state. We denote the second moments with the covariance matrix

$$\Gamma = \begin{pmatrix} Q & R \\ R^{\mathrm{T}} & P \end{pmatrix}, \tag{5.9}$$

in which $Q_{nm} = \langle\hat{\varphi}(z_n)\hat{\varphi}(z_m)\rangle$, $P_{nm} = \langle\delta\hat{\rho}(z_n)\delta\hat{\rho}(z_m)\rangle$, $R_{nm} = \left\langle\frac{1}{2}\left\{\hat{\varphi}(z_n), \delta\hat{\rho}(z_m)\right\}\right\rangle$ with $n, m \in \{1, 2, \ldots, N\}$, where N is the total number of modes. Here, we are not interested in the first moments, as they do not affect the quantum information measures and actually vanish due to the symmetries in our system as we will discuss later.

5.3.1 Von Neumann entropy and quantum mutual information

To calculate vN or Rényi entropies we use the symplectic eigenvalues of Γ that encode the information about the state. The n^{th} eigenstate γ_n is obtained by diagonalizing the matrix $\mathcal{G}$,

$$\mathcal{G} = \mathrm{i}\Omega\Gamma\,, \tag{5.10}$$

$$\Omega = \begin{pmatrix} 0 & \mathbb{I}_N \\ -\mathbb{I}_N & 0 \end{pmatrix}. \tag{5.11}$$

Here, Ω is the symplectic unit and $\mathbb{I}_N$ represents the $N \times N$ identity matrix. The vN entropy then reads

$$S(\Gamma) = \sum_{n=1}^{N}\left[\left(\gamma_n + \tfrac{1}{2}\right)\ln\left(\gamma_n + \tfrac{1}{2}\right) - \left(\gamma_n - \tfrac{1}{2}\right)\ln\left(\gamma_n - \tfrac{1}{2}\right)\right]. \tag{5.12}$$

For a pedagogical introduction to Gaussian states and derivation of this equation, see [96].

5.4 Theoretical model

After constructing the quantum information basis in the first part of this chapter, the rest is dedicated to the verification of the area law of MI in quantum field theory. In particular, we are interested in the equilibrium states of the massive Klein-Gordon (KG) Hamiltonian, which is a free quadratic theory. As we will see in the upcoming sections, the thermal equilibrium states of this model are Gaussian states, allowing us to easily calculate the quantum information measures as discussed in section 5.3. Despite its simplicity, experimental verification of the area law of MI for the KG model is yet to be provided.

5.4.1 Klein-Gordon Hamiltonian with homogeneous background density

All the experiments presented in this chapter are performed in a longitudinal box-like potential, resulting in a nearly homogeneous averaged density, $\rho_0(z) \equiv n_{1\mathrm{D}}$. Hence, for a system of size L, the KG Hamiltonian from eq. (2.38), can be written as

$$\hat{H}_{\mathrm{KG}} = \int_0^L \mathrm{d}z \left[g_{1\mathrm{D}} \delta\hat{\rho}^2(z) + \frac{\hbar^2 n_{1\mathrm{D}}}{4m} \left(\partial_z \hat{\varphi}(z)\right)^2 + \hbar J n_{1\mathrm{D}} \hat{\varphi}^2(z) \right] . \tag{5.13}$$

As a reminder, $g_{1\mathrm{D}}$ is the 1D interaction strength, introduced in eq. (2.2), J is the single-particle tunneling rate, and $m = 1.44 \times 10^{-25}$ kg the mass of a ^{87}Rb atom.

Defining the speed of sound v, the Luttinger parameter K, and the KG mass M,

$$v = \sqrt{\frac{g_{1\mathrm{D}} n_{1\mathrm{D}}}{m}} , \tag{5.14}$$

$$K = \frac{\hbar\pi}{2} \sqrt{\frac{n_{1\mathrm{D}}}{m g_{1\mathrm{D}}}} , \tag{5.15}$$

$$M = 2m \sqrt{\frac{\hbar J}{g_{1\mathrm{D}} n_{1\mathrm{D}}}} , \tag{5.16}$$

we can write the KG Hamiltonian in terms of macroscopic variables as

$$\hat{H}_{\mathrm{KG}} = \frac{\hbar v}{2} \int_0^L \mathrm{d}z \left[\frac{\pi}{K} \delta\hat{\rho}^2(z) + \frac{K}{\pi} \left(\partial_z \hat{\varphi}(z)\right)^2 \right] + \frac{M^2 v^4}{2\hbar v} \int_0^L \mathrm{d}z \, \frac{K}{\pi} \hat{\varphi}^2(z) . \tag{5.17}$$

5.4.2 Thermal equilibrium states of the Klein-Gordon Hamiltonian

The covariance matrix elements of the thermal equilibrium states of the KG Hamiltonian in real space are given by [97],

$$\begin{aligned} Q_{ij} &= \frac{\pi}{2KL}\frac{\hbar v}{Mv^2}\coth\left(\frac{Mv^2}{2k_BT}\right) \\ &\quad + \frac{\pi}{KL}\sum_{n=1}^{N}\frac{\hbar v}{\epsilon_n}\coth\left(\frac{\epsilon_n}{2k_BT}\right)\cos(k_nz_i)\cos(k_nz_j)\ , && (5.18) \\ R_{ij} &= 0\ , && (5.19) \\ P_{ij} &= \frac{K}{2\pi L}\frac{Mv^2}{\hbar v}\coth\left(\frac{Mv^2}{2k_BT}\right) \\ &\quad + \frac{K}{\pi L}\sum_{n=1}^{N}\frac{\epsilon_n}{\hbar v}\coth\left(\frac{\epsilon_n}{2k_BT}\right)\cos(k_nz_i)\cos(k_nz_j)\ , && (5.20) \end{aligned}$$

with the dispersion relation $\epsilon_n = \sqrt{\hbar^2k_n^2v^2 + M^2v^4}$. Here, T is the temperature, and N is the UV cut-off. To simulate the effect of the finite imaging resolution, all theoretical calculations presented here are convolved with a Gaussian point-spread function (PSF) with a standard deviation $\sigma_{\mathrm{PSF}} \approx 3\,\mu\mathrm{m}$ [39].

5.5 Experimental protocol and tomography process

To experimentally verify the area law of MI,

1. we prepare our system in a thermal equilibrium state or a prethermalized state in a double-well potential with strong tunneling strength. We *do not make any assumptions* about this initial state: We *do not* assume that it is an equilibrium state of the KG model and we *do not* even assume that it is Gaussian. We rather confirm the Gaussianity by showing that the higher-order correlations are negligible (see fig. 5.1).

2. We then measure the vN entropy and MI by a tomography process. It is important to note that the only assumption for the tomography is that the dynamics of the system are given by the free massless theory, the Tomonaga-Luttinger liquid (TLL).

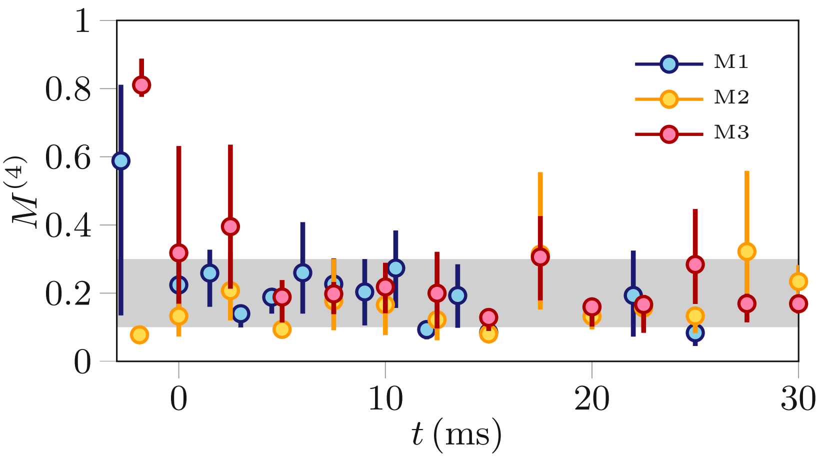

Figure 5.1 Fourth order correlations. The error bars represent 95% confidence intervals obtained via bootstrapping. The shaded area is the typically calculated bias [15, 16].

3 To compare the experiment with theory, we extract the relevant parameters, including the temperature and the KG mass use them to calculate the correlations in eqs. (5.18) to (5.20). The final results are shown in figs. 5.4 and 5.5

5.5.1 Initial states

The extracted parameters for the three measurements[1] presented in this chapter are written in table 5.1. Also, the corresponding raw images with a MATLAB script to calculate the absorption images are available online [45].

For measurements M2 and M3, the initial state is prepared by cooling the atoms directly into the double-well potential, resulting in a thermal equilibrium state with typical temperatures ranging from 30 to 120 nK and linear atomic densities of approximately 70 µm^{-1} in a box-like potential with a length of about 50 µm. The double-well barrier is set low enough ensuring strong tunneling-coupling between the two condensates. These measurements were taken before the implementation of the DMD setup by Bernhard Rauer. Hence the longitudinal trapping potential is provided by shining a blue-detuned 767 nm light through a mask. The details can be found in **Rauer-Thesis**.

To achieve lower *effective* temperatures in measurement M1, I create prethermalized states with different temperatures between common and relative degrees of freedom [12].

---

[1] M1: Scan 9617, M2: Scan 5722, M3: Scan 5831

Die approbierte gedruckte Originalversion dieser Dissertation ist an der TU Wien Bibliothek verfügbar.
The approved original version of this doctoral thesis is available in print at TU Wien Bibliothek.
TU Bibliothek WIEN Your knowledge hub

Measurement	T (nK)	λ_T (µm)	$\omega_M/2\pi$ (Hz)	l_C (µm)	$q = \lambda_T/\ell_J$	$r = \hbar\omega_M/k_\mathrm{B}T$
M1	14	37	34	7.3	5	0.11
M2	48	18	43	6.8	2.6	0.043
M3	94	9.5	40	7.4	1.3	0.021

Table 5.1 List of relevant parameters for the three measurements. T is the temperature, λ_T the thermal coherence length, $\omega_M = Mv^2/\hbar$ the KG mass in angular frequency units, and l_C the healing length of the phase.

To this end, I initially cool the atoms down in a dressed single-well potential, where the first excited state is in the vacuum state. Then, gradually splitting the atomic cloud into two parts maps the ground state and the first excited state to two states with a smaller energy gap and symmetric and anti-symmetric wave functions. This leads to a prethermalized state with a lower effective temperature in the relative degrees of freedom.

It is important to note again that we do not make any assumptions about our prepared initial states. We do *not* assume that they are the equilibrium states of any Hamiltonian. We even do *not* assume that the prepared states are Gaussian, rather we confirm their Gaussianity by calculating the normalized, averaged connected fourth-order correlations, $M^{(4)}$, as introduced and discussed in **Schweigler-Thesis**. The results are presented in fig. 5.1.

5.5.2 Mass quench

As mentioned earlier, we opt to quantify vN entropy and MI of the thermal states of the KG model in equilibrium. However, to initiate the independent evolution of the initially coupled condensates, and to implement the tomography process explained in section 5.5.3, we perform a mass quench in a short time. The mass quench is implemented by ramping the radio frequency amplitude linearly in about 2 ms to increase the barrier height. In theory, this change corresponds to a quench from KG to TLL Hamiltonian. In the next section, we investigate the time evolution under the TLL Hamiltonian.

5.5.3 Tomography process: Post-quench quantum read-out

As discussed in section 3.3.2, we can only directly measure one of the canonical variables, the relative phase. Hence, we indirectly access the canonically conjugate variable, the relative density fluctuations, by allowing the system to evolve under a known harmonic Hamiltonian with known mode frequencies and measuring the phase correlations at different times. To fully characterize the system's state, we employ the quantum tomography method developed in [98].

For each harmonic mode, the dynamics involve rotations in phase space, converting the initial density variance into phase variance and vice versa. By measuring the phase at multiple time points, we can fully reconstruct the initial covariance matrix. This process involves transforming to Fourier space, where modes evolve independently, and then fitting the data for the time evolution of the phase covariance in real space using known functions expressing this data in terms of the initial phase and density correlations.

The tomography process introduced in [98] treats the harmonic modes, but not the *zero mode*, corresponding to zero momentum and energy. The reconstruction of this mode is a novel contribution by our theory-collaborators introduced in [44]. The zero mode requires special treatment as it moves at a constant velocity and exhibits phase diffusion, with its phase variance growing quadratically over time [99]. Additionally, due to the compactified nature of the phase field, phases differing by 2π are considered identical, limiting observations to the interval $[-\pi, +\pi]$. For the zero mode, we fit a quadratic function and restrict the fit to times before reaching the upper bound due to compactification.

The post-quench dynamics follow the Tomonaga-Luttinger liquid (TLL) Hamiltonian, obtained by setting $M = 0$ in eq. (5.17)

$$\hat{H}_{\mathrm{TLL}} = \frac{\hbar v}{2} \int_0^L \mathrm{d}z \left[\frac{\pi}{K} \delta\hat{\rho}^2(z) + \frac{K}{\pi} \left(\partial_z \hat{\varphi}(z)\right)^2 \right] . \tag{5.21}$$

Considering a system with size L in a box-like confinement with hard walls at $z = 0, L$, the particle current on the edges vanishes, resulting in effective boundary conditions of Neumann type,

$$\partial_z \hat{\varphi}(z = 0) = \partial_z \hat{\varphi}(z = L) = 0 \, . \tag{5.22}$$

In this case, the cosine eigenfunctions (see Appendix A),

$$\begin{aligned} f_n^{\hat{\varphi}}(z) &= \begin{cases} \left(\frac{1}{2} nK\right)^{-1/2} \cos\left(n \frac{\pi}{L} z\right) , & n > 0 \\ 1 \, , & n = 0 \end{cases} \\ f_n^{\delta\hat{\rho}}(z) &= \begin{cases} -\frac{1}{L} \left(2nK\right)^{1/2} \cos\left(n \frac{\pi}{L} z\right) , & n > 0 \\ -\frac{1}{L} \, , & n = 0 \end{cases} , \end{aligned} \tag{5.23}$$

diagonalize the Hamiltonian, yielding

$$\hat{\tilde{H}}_{\mathrm{TLL}} = \frac{\hbar u}{2}\delta\hat{\rho}_0^2 + \sum_{n=1}^{\infty}\frac{\hbar\omega_n}{2}\left[\delta\hat{\rho}_n^2 + \hat{\varphi}_n^2\right] \; , \tag{5.24}$$

where

$$u = \frac{\pi v}{LK} \; , \tag{5.25}$$

$$\omega_n = v k_n \; . \tag{5.26}$$

As expected, the dispersion relation of this free massless theory is linear as we see in eq. (5.26), with

$$k_n = \frac{n\pi}{L} \; . \tag{5.27}$$

We are now ready to calculate the time evolution of the eigenmodes using the Heisenberg equation of motion for $\hat{\varphi}_n(t)$,

$$\partial_t\hat{\varphi}_n(t) = \frac{\mathrm{i}}{\hbar}\left[\hat{\tilde{H}}_{\mathrm{TLL}}, \hat{\varphi}_n(t)\right] = -\omega_n\delta\hat{\rho}_n(t) \tag{5.28}$$

$$\partial_t\hat{\varphi}_0(t) = \frac{\mathrm{i}}{\hbar}\left[\hat{\tilde{H}}_{\mathrm{TLL}}, \hat{\varphi}_0(t)\right] = -u\delta\hat{\rho}_0(t) \; , \tag{5.29}$$

and $\delta\hat{\rho}_n(t)$

$$\partial_t\delta\hat{\rho}_n(t) = \frac{\mathrm{i}}{\hbar}\left[\hat{\tilde{H}}_{\mathrm{TLL}}, \delta\hat{\rho}_n(t)\right] = \omega_n\hat{\varphi}_n(t) \tag{5.30}$$

$$\partial_t\delta\hat{\rho}_0(t) = \frac{\mathrm{i}}{\hbar}\left[\hat{\tilde{H}}_{\mathrm{TLL}}, \delta\hat{\rho}_0(t)\right] = 0 \tag{5.31}$$

where we have used

$$\left[\hat{\varphi}_n^2(t), \delta\hat{\rho}_n(t)\right] = -2\mathrm{i}\hat{\varphi}_n(t) \tag{5.32}$$

$$\left[\delta\hat{\rho}_n^2(t), \hat{\varphi}_n(t)\right] = 2\mathrm{i}\delta\hat{\rho}_n(t) \; . \tag{5.33}$$

For $n = 0$ we obtain

$$\delta\hat{\rho}_0(t) = \delta\hat{\rho}_0 = \mathrm{const.} \tag{5.34}$$

$$\hat{\varphi}_0(t) = -u\delta\hat{\rho}_0(0)t + \hat{\varphi}_0(0) \; . \tag{5.35}$$

Die approbierte gedruckte Originalversion dieser Dissertation ist an der TU Wien Bibliothek verfügbar.
The approved original version of this doctoral thesis is available in print at TU Wien Bibliothek.
TU Bibliothek WIEN Your knowledge hub

For the harmonic modes ($n > 0$), we get the following second-order equations,

$$\partial_t^2 \delta\hat{\rho}_n(t) = \omega_n \partial_t \hat{\varphi}_n(t) = -\omega_n^2 \delta\hat{\rho}_n(t) \tag{5.36}$$

$$\partial_t^2 \hat{\varphi}_n(t) = -\omega_n \partial_t \delta\hat{\rho}_n(t) = -\omega_n^2 \hat{\varphi}_n(t) \ . \tag{5.37}$$

These equations motivate the Ansatz:

$$\begin{aligned} \hat{\varphi}_n(t) = \hat{\varphi}_n(0)\,[A_{n,\hat{\varphi}} \cos(\omega_n t) + B_{n,\hat{\varphi}} \sin(\omega_n t)] \\ + \delta\hat{\rho}_n(0)\,[C_{n,\hat{\varphi}} \cos(\omega_n t) + D_{n,\hat{\varphi}} \sin(\omega_n t)] \ , \end{aligned} \tag{5.38}$$

$$\begin{aligned} \delta\hat{\rho}_n(t) = \delta\hat{\rho}_n(0)\,[A_{n,\delta\hat{\rho}} \cos(\omega_n t) + B_{n,\delta\hat{\rho}} \sin(\omega_n t)] \\ + \hat{\varphi}_n(0)\,[C_{n,\delta\hat{\rho}} \cos(\omega_n t) + D_{n,\delta\hat{\rho}} \sin(\omega_n t)] \ . \end{aligned} \tag{5.39}$$

The set of first-order equations gives:

$$\begin{aligned} \partial_t \hat{\varphi}_n(t) = \hat{\varphi}_n(0)\,[-\omega_n A_{n,\hat{\varphi}} \sin(\omega_n t) + \omega_n B_{n,\hat{\varphi}} \cos(\omega_n t)] \\ + \delta\hat{\rho}_n(0)\,[-\omega_n C_{n,\hat{\varphi}} \sin(\omega_n t) + \omega_n D_{n,\hat{\varphi}} \cos(\omega_n t)] \ , \end{aligned} \tag{5.40}$$

$$\begin{aligned} \partial_t \delta\hat{\rho}_n(t) = \delta\hat{\rho}_n(0)\,[-\omega_n A_{n,\delta\hat{\rho}} \sin(\omega_n t) + \omega_n B_{n,\delta\hat{\rho}} \cos(\omega_n t)] \\ + \hat{\varphi}_n(0)\,[-\omega_n C_{n,\delta\hat{\rho}} \sin(\omega_n t) + \omega_n D_{n,\delta\hat{\rho}} \cos(\omega_n t)] \ . \end{aligned} \tag{5.41}$$

Putting eqs. (5.38) and (5.40) in eq. (5.28) and also eqs. (5.39) and (5.41) in eq. (5.30) yields

$$\begin{aligned} -\omega_n A_{n,\hat{\varphi}} &= -\omega_n D_{n,\delta\hat{\rho}} \ , \\ \omega_n B_{n,\hat{\varphi}} &= -\omega_n C_{n,\delta\hat{\rho}} \ , \\ -\omega_n C_{n,\hat{\varphi}} &= -\omega_n B_{n,\delta\hat{\rho}} \ , \\ \omega_n D_{n,\hat{\varphi}} &= -\omega_n A_{n,\delta\hat{\rho}} \ . \end{aligned}$$

From the initial conditions $\hat{\varphi}_n(t) = \hat{\varphi}_n(0)$, $\delta\hat{\rho}_n(t) = \delta\hat{\rho}_n(0)$ we get $C_{n,\hat{\varphi}} = 0$, $C_{n,\delta\hat{\rho}} = 0$ and thus $B_{n,\delta\hat{\rho}} = 0$ and $B_{n,\hat{\varphi}} = 0$. They also give $A_{n,\hat{\varphi}} = 1$, $A_{n,\delta\hat{\rho}} = 1$. The resulting time evolution of the harmonic modes is

$$\hat{\varphi}_n(t) = \hat{\varphi}_n(0) \cos(\omega_n t) - \delta\hat{\rho}_n(0) \sin(\omega_n t) \ , \tag{5.42}$$

$$\delta\hat{\rho}_n(t) = \delta\hat{\rho}_n(0) \cos(\omega_n t) + \hat{\varphi}_n(0) \sin(\omega_n t) \ . \tag{5.43}$$

Having these equations of motion at hand, we will go through the reconstruction process based on measured relative phase profiles in the upcoming sections.

Zero mode $(n = 0)$

As mentioned earlier, the zero mode, representing a constant eigenfunction in real space, behaves differently from all higher modes since it is not a harmonic oscillator mode. The reason is that the Hamiltonian for the zero mode term contains only one of the canonical variables, $\delta\hat{\rho}_0$.

The time evolution of the zero mode is given by eqs. (5.34) and (5.35), meaning that the time dependence of the phase variance has the following form,

$$\left\langle\hat{\varphi}_0^2(t)\right\rangle = \left\langle\hat{\varphi}_0^2(0)\right\rangle - \langle\{\hat{\varphi}_0(0), \delta\hat{\rho}_0(0)\}\rangle\, ut + \left\langle\delta\hat{\rho}_0^2(0)\right\rangle u^2t^2 \tag{5.44}$$

However, due to the compactified nature of the phase field, the zero mode component $\hat{\varphi}_0$ is not a directly measurable operator. Only imaginary exponentials of the form $e^{\mathrm{i}n\hat{\varphi}_0}$ for integer n are well-defined. Nonetheless, assuming the initial state is Gaussian in terms of the zero mode, as well as all other modes, and remains Gaussian under the dynamics governed by H_{TLL}, we can determine the zero mode variance from the mean value of $e^{\mathrm{i}n\hat{\varphi}_0}$. Using the cumulant expansion formula for Gaussian random variables, we obtain

$$\langle\exp\left(\mathrm{i}\hat{\varphi}_0(t)\right)\rangle = \exp\left(\mathrm{i}\left\langle\hat{\varphi}_0(t)\right\rangle - \left\langle\hat{\varphi}_0^2(t)\right\rangle/2\right) , \tag{5.45}$$

from which we find

$$\left\langle\hat{\varphi}_0^2(t)\right\rangle = -2\ln\left|\langle\exp\left(\mathrm{i}\hat{\varphi}_0(t)\right)\rangle\right| . \tag{5.46}$$

Thus, to extract the zero mode part of the covariance matrix $\langle\hat{\varphi}_0^2(0)\rangle$, $\langle\delta\hat{\rho}_0^2(0)\rangle$, and $\langle\{\hat{\varphi}_0(0), \delta\hat{\rho}_0(0)\}\rangle$ in the initial state, we calculate the zero mode variance of the phase at each time using (5.46) and fit it with the theoretical formula (5.44).

Harmonic modes $(n > 0)$

To reconstruct the initial covariance of the harmonic modes, we first calculate a referenced second-order phase correlation function using the measured phase profiles,

$$\Phi_{ab}^2(t) = \left\langle\Big(\hat{\varphi}(z_a, t) - \hat{\varphi}(z_0, t)\Big)\Big(\hat{\varphi}(z_b, t) - \hat{\varphi}(z_0, t)\Big)\right\rangle . \tag{5.47}$$

The reason to subtract the phase of an arbitrary reference position z_0 is merely to remove the zero mode contribution, but it has no effect on the higher modes. Expanding $\hat{\varphi}$ with cosine eigenfunctions (5.23), yields

$$\Phi_{ab}^2(t) = \sum_{j,k=1}^{N} f_{j,k}^{a,b}\,\langle\hat{\varphi}_j(t)\hat{\varphi}_k(t)\rangle \tag{5.48}$$

with

$$f_{j,k}^{a,b} = \left(f_j^{\hat{\varphi}}(z_a) - f_j^{\hat{\varphi}}(z_0) \right) \left(f_k^{\hat{\varphi}}(z_b) - f_k^{\hat{\varphi}}(z_0) \right) . \tag{5.49}$$

Inserting the equation of motion for the phase modes, eq. (5.42), and defining $\tilde{Q}_{jk} = \langle \hat{\varphi}_j(0)\hat{\varphi}_k(0)\rangle$, $\tilde{R}_{jk} = \left\langle \frac{1}{2} \{\hat{\varphi}_j(0), \delta\hat{\rho}_k(0)\} \right\rangle$, and $\tilde{P}_{jk} = \langle \delta\hat{\rho}_j(0)\delta\hat{\rho}_k(0)\rangle$, we obtain

$$\begin{aligned} \Phi^2_{ab}(t) = &\sum_{j,k=1}^{N} f_{j,k}^{a,b} \cos(\omega_j t) \cos(\omega_k t) \tilde{Q}_{jk} \\ &+ \sum_{j,k=1}^{N} (-f_{j,k}^{a,b} - f_{j,k}^{a,b}) \cos(\omega_j t) \sin(\omega_k t) \tilde{R}_{jk} \\ &+ \sum_{j,k=1}^{N} f_{j,k}^{a,b} \sin(\omega_j t) \sin(\omega_k t) \tilde{P}_{jk} . \end{aligned} \tag{5.50}$$

This equation plays the central part in the tomography process: The objective is to determine the elements of $\tilde{Q}$, $\tilde{R}$, and $\tilde{P}$ through an optimization process. It is important to note that the left-hand side is obtained from experimentally measured phase profiles, while the right-hand side involves the calculation of $f_{j,k}^{a,b}$ and ω_j using experimental parameters, as described in (5.23) and (5.26), respectively. The tomography results for the three measurements are presented in section 5.6.1.

5.6 Experimental results

5.6.1 Tomography results

The outcomes of the reconstruction process for the three measurements are depicted in figs. 5.2 and 5.3. We illustrate both the covariance matrix elements obtained in the Fourier space after tomography and the elements in the position space following a discrete inverse Fourier transform. It is essential to note that the sole constraint on the elements of $\tilde{\Gamma}$ is to ensure that the resulting state is physical, adhering to the Heisenberg uncertainty relation [98]. We refrain from limiting the state by any further assumptions, such as assuming Gaussianity or assuming small values for $\tilde{R}$.

Estimating the temperature and Klein-Gordon mass

To compute theoretical predictions for the mutual information in the initial state, assuming it to be the thermal state of the KG model, we need to estimate two parameters: The KG mass, M, and the temperature, T. This estimation involves fitting the results of the tomographic reconstruction for the mode variances to those

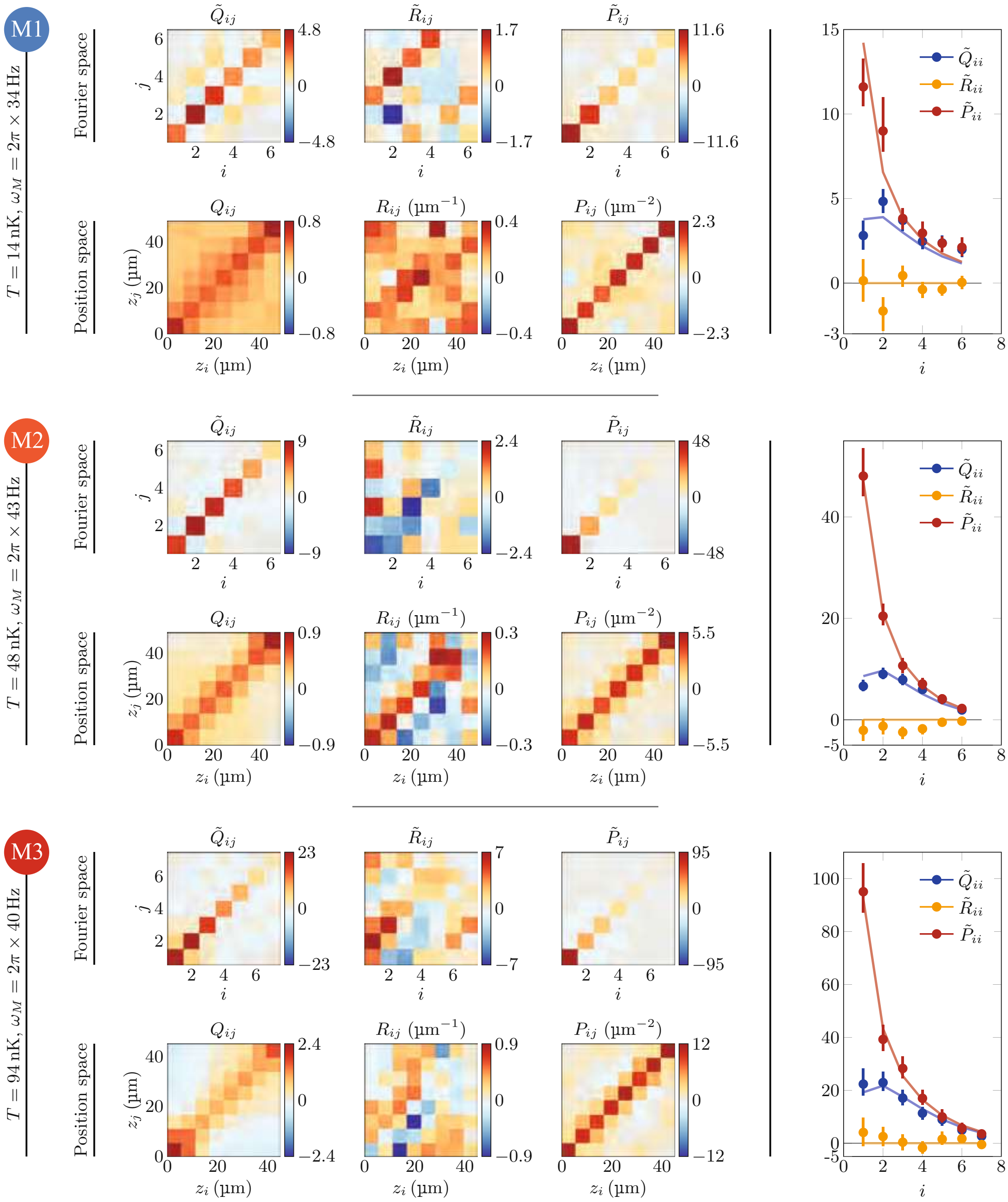

Figure 5.2 Tomography results for three measurements with increasing temperatures (M1 to M3). For each measurement, the covariance matrix elements are shown in both Fourier and position space. The diagonal elements of the covariance matrix in Fourier space are displayed on the right. Error bars represent 95% confidence intervals obtained through bootstrapping. The theory calculations corresponding to the extracted temperature and KG mass for each measurement are represented by solid lines.

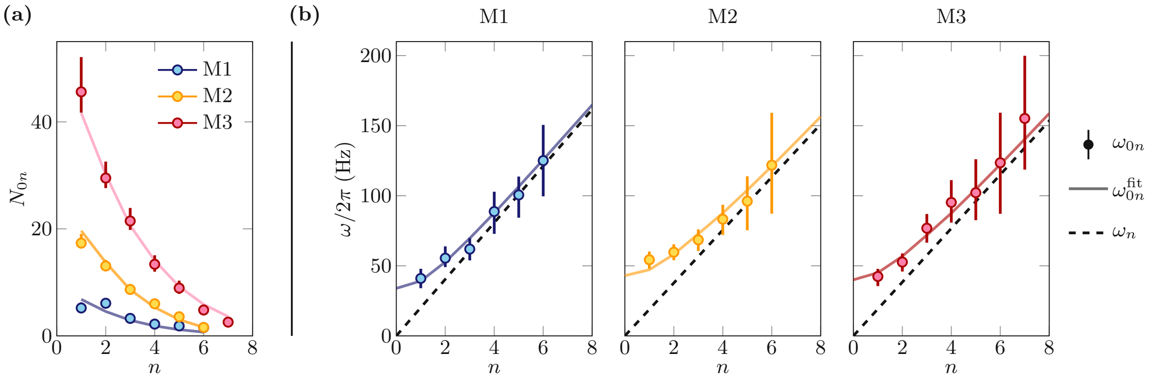

Figure 5.3 Fitting temperature and KG mass from mode occupation number and dispersion relation. (a) Measurement results of N_{0n} are shown along with a fitting curve (solid line), N_{0n}^{fit}. **(b)** The dispersion relation for three different measurements is plotted. Error bars for each quantity represent 95% confidence intervals obtained through bootstrapping.

corresponding to KG thermal states. As the modes are decoupled from each other both initially and during the tomography dynamics, we can independently estimate the KG mode frequency for each mode. Once the mode frequencies are estimated, we can verify if they follow the theoretical dispersion relation of the KG model and extract the corresponding mass parameter through a fitting process.

The relationship between the post-quench quadratures and the initial KG state with mode occupation number N_{0n} is described by the following equations:

$$\tilde{Q}_{nn} = \frac{\omega_n}{\omega_{0n}}\left(N_{0n} + \frac{1}{2}\right) , \tag{5.51}$$

$$\tilde{P}_{nn} = \frac{\omega_{0n}}{\omega_n}\left(N_{0n} + \frac{1}{2}\right) , \tag{5.52}$$

where ω_{0n} and ω_n are the pre- and post-quench mode frequencies, respectively. The quantities $\tilde{Q}_{nn}$ and $\tilde{P}_{nn}$ are the reconstructed correlations, and ω_n is given by the eq. (5.26). From eqs. (5.51) and (5.52), we can calculate both ω_{0n} and N_{0n},

$$N_{0n} = \sqrt{\tilde{Q}_{nn}\tilde{P}_{nn}} - \frac{1}{2} , \tag{5.53}$$

$$\omega_{0n} = \omega_n \sqrt{\frac{\tilde{P}_{nn}}{\tilde{Q}_{nn}}} . \tag{5.54}$$

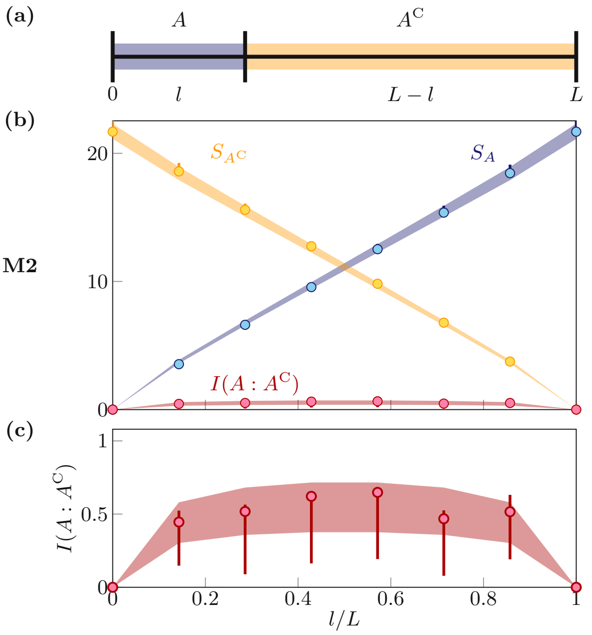

Figure 5.4 Area law of Mutual Information (MI) and volume law of von Neumann entropy. **(a)** We consider a system of size $L = 49\,\mu\mathrm{m}$ that is divided into a subsystem A of length l and its complement subsystem of length $(L - l)$. **(b)** The experimental results for $I(A : A^{\mathrm{C}})$, S_A, and $S_{A^{\mathrm{C}}}$, calculated based on $N = 7$ modes, are represented as data points with error bars denoting the 95% confidence intervals obtained using bootstrapping [100]. The shaded regions represent the 95% confidence interval for the theoretical predictions, accounting for the uncertainty in the estimated temperature and tunneling rate J. **(c)** A close-up view of the measured MI.

Assuming thermal initial states, we fit a convolved Bose-Einstien distribution to N_{0n}, to fit the temperature, $T = (\beta k_{\mathrm{B}})^{-1}$ and σ_{PSF},

$$N_{0n}^{\mathrm{fit}} + \frac{1}{2} = \left(\frac{1}{\exp(\hbar\omega_{0n}\beta) - 1} + \frac{1}{2} \right) \exp\left(-k_n^2 \sigma_{\mathrm{PSF}}^2 / 2 \right) . \tag{5.55}$$

The convolution is due the finite imaging resolution.

To extract the KG mass, we fit the KG dispersion relation,

$$\omega_{0n}^{\mathrm{fit}} = \sqrt{v^2 k_n^2 + M^2 v^4 / \hbar^2} \, , \tag{5.56}$$

to the calculated ω_{0n}.

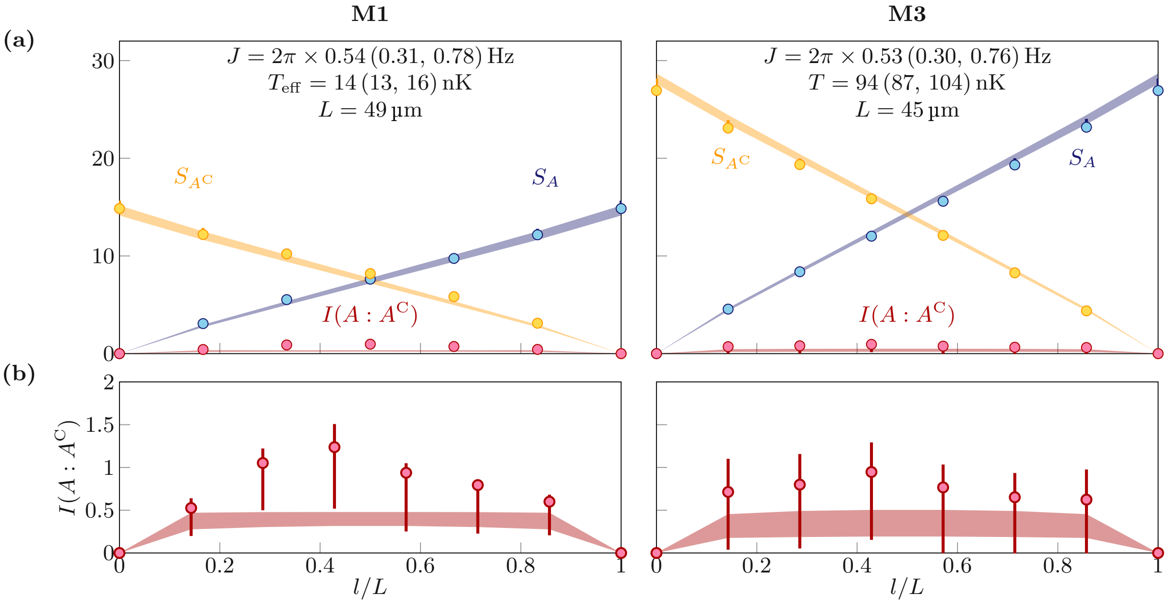

Figure 5.5 Results for area law of mutual information and volume law of von Neumann entropy for measurements M1 and M3 (a) Experimental data for $I(A : A^{\mathrm{C}})$, S_A, and $S_{A^{\mathrm{C}}}$, obtained using $N = 7$ modes (refer to fig. 5.4 for detailed explanation). The extracted parameters, along with their 95% confidence intervals in parenthesis, are provided above. **(b)** Close-up view of the measured mutual information.

5.6.2 Von Neumann entropy and mutual information

Once we have the covariance matrix in the Fourier space for the first N modes, we employ a discrete Fourier transformation (see Appendix A) based on the cosine eigenfunctions (eq. (5.23)) to compute the covariance matrix Γ in the real space. The cut-off is determined based on the reconstructed occupation numbers (fig. 5.3), and we consider only modes with positive occupation numbers, corresponding to physical states. This covariance matrix is then used to calculate the vN entropy of a subsystem A using eq. (5.12). The vN entropy results are shown in fig. 5.4(b) and fig. 5.5(a). We also calculate the MI between two subsystems A and B using eq. (5.5). To study the scaling behavior of the vN entropy and MI, we calculate the vN entropy for subsystems of varying lengths and subsequently compute the MI with their complementary subsystems, as illustrated in fig. 5.4(a). As expected for thermal states, the vN entropy follows a volume law, exhibiting a linear dependence on the subsystem size. Measuring the vN entropy allows us to investigate the scaling of the mutual information. We observe an area law for the MI, with a plateau forming within the bulk of the system as shown

TU Bibliothek Die approbierte gedruckte Originalversion dieser Dissertation ist an der TU Wien Bibliothek verfügbar. The approved original version of this doctoral thesis is available in print at TU Wien Bibliothek.
WIEN Your knowledge hub

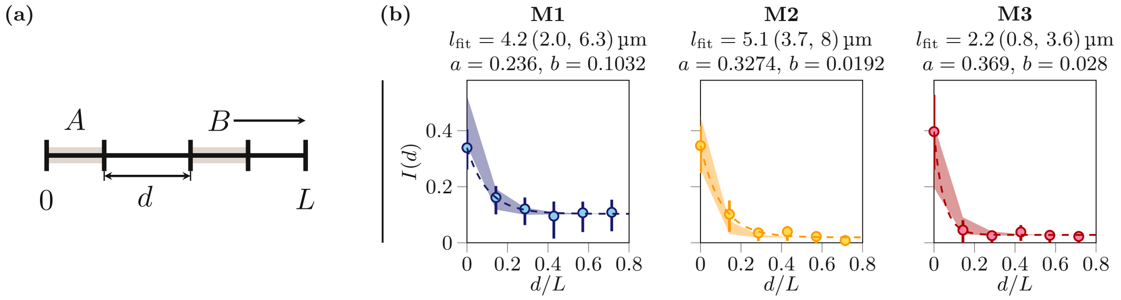

Figure 5.6 Information shared between spatially separated subsystems. In this analysis, we calculate the MI between two disjoint subsystems with the same length, $l/L = 0.15$, as a function of the distance between them, d. **(a)** Illustration of the setting, where subsystem A is fixed at the left edge of the system, while subsystem B is shifted away to the other edge. **(b)** For three measurements, the circles represent experimental data for $I(d) = I(A : B)$, the shaded area corresponds to theoretical data (see fig. 5.4 for more information on error bars and shading), and the dashed lines is an exponential fit, $f_{\mathrm{fit}} = a \exp(-d/l_{\mathrm{fit}}) + b$. The fit results are written in the title of each plot (The reported intervals represent the 95% confidence intervals obtained via bootstrapping.). Note that to better represent the agreement between theory and experimental data, the theoretical calculations are shifted by b. The finite bias b arises from estimating a positive quantity, MI, using finite statistics.

in fig. 5.4(c) and fig. 5.5(b). These findings provide experimental verification of a fundamental characteristic of quantum many-body systems [86].

Next, we examine the dependence of the MI on the distance between two subsystems, specifically the gap length d that separates subsystems A and B. The results are presented in fig. 5.6. Consistent with expectations, the MI decreases as the separation between the two subsystems increases. By fitting an exponential function to the experimental data, we extract a decay length denoted as l_{fit}. For measurement M2, this fitted decay length agrees with the correlation length ℓ_J calculated based on the experimental parameters as introduced in eq. (2.37). For the other two measurements, the fit underestimates the correlation length. Note that this fit is basically given by the first two points, hence it is highly sensitive to fluctuations of those points.

For typical temperatures in our experiment, the vN entropy exhibits a linear dependence on temperature. However, the linear dependence transitions to a logarithmic dependence when introducing a finite ultra-violet (UV) cut-off, as shown in the inset of fig. 5.7 (dashed lines). As the temperature increases, the symplectic eigenvalues grow, and the calculated entropy using a finite number of modes saturates. In contrast, the MI, regardless of the UV cut-off, converges to a finite asymptotic value determined by

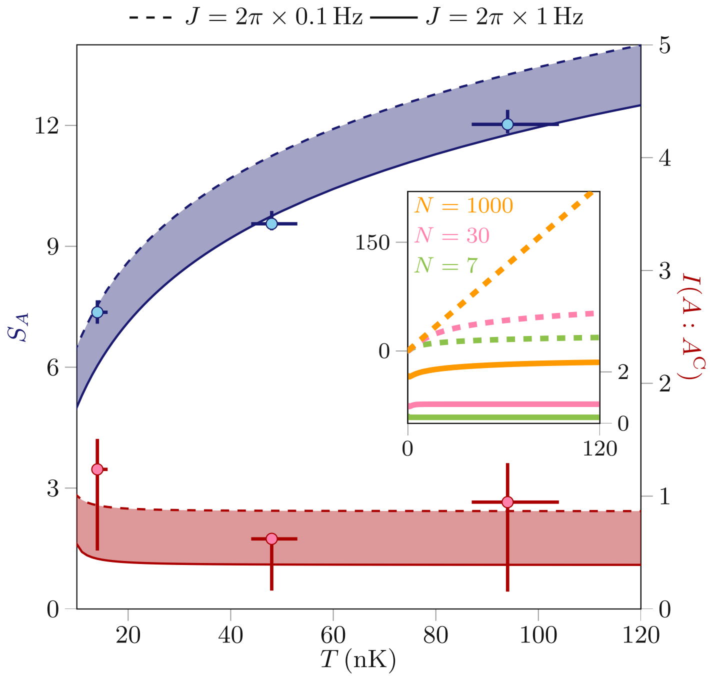

Figure 5.7 Temperature dependence of mutual information (MI) and von Neumann entropy (vN entropy). The experimental data (circles) depict S_A (left axis) and $I(A : A^{\mathrm{C}})$ (right axis) for three different temperatures (M1-M3), all measured with $N = 7$ modes and $l/L = 0.4$. The error bars represent the 95% confidence intervals obtained via bootstrapping. The shaded regions correspond to theoretical calculations based on different tunneling rates, ranging from $J = 2\pi \times 0.1\,\mathrm{Hz}$ (dashed lines) to $2\pi \times 1\,\mathrm{Hz}$ (solid lines). The inset illustrates the theoretical predictions for S_A (left axis) and $I(A : A^{\mathrm{C}})$ (right axis) at three distinct values of N, considering $J = 2\pi \times 0.4\,\mathrm{Hz}$, without accounting for the effect of finite optical resolution.

classical correlations [101]. Reducing the number of modes diminishes the asymptotic value due to the limited information available in the considered modes, as depicted in the inset of fig. 5.7 (solid lines). The main part of this figure illustrates the measured vN entropy and MI for three different temperatures, along with the corresponding theoretical predictions. The measurements align with the theory calculated for the extracted parameters and $N = 7$ lowest modes.

Effect of finite imaging resolution

We investigate the impact of finite imaging resolution and an ultra-violet cut-off on the measurement of MI. The Gaussian point-spread function of the imaging system acts as a soft cut-off, limiting the number of observable modes and affecting the measurement

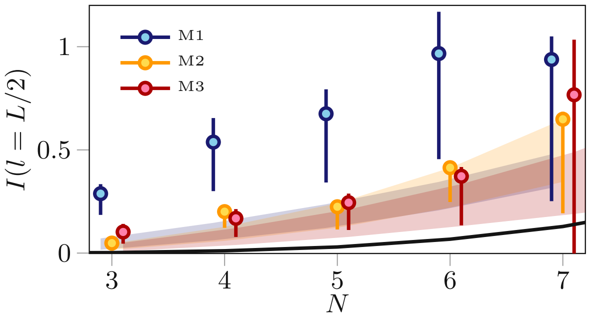

Figure 5.8 Effect of finite imaging resolution on mutual information. The mutual information, $I(A : A^{\mathrm{C}})$, for $l = L/2$ is plotted for various cut-off values, N for three measurements (M1-M3). The error bars indicate the 95% confidence interval, and the shaded areas represent the theoretical calculations. The solid black line corresponds to the residual mutual information arising from the finite imaging resolution effect.

of lower modes (see figs. 5.8 and 5.9 in **Schweigler-Thesis**). At length scales close to or smaller than the imaging resolution, blurring effects introduce correlations, leading to unphysical MI. To quantify this "fake" MI, we consider a state with high temperature and a short correlation length (much shorter than the imaging resolution), resulting in a practically zero MI value ($\sim 10^{-6}$). We calculate the MI of the half-system ($l = L/2$) for this state using different numbers of modes, N, and present the results in fig. 5.8 with solid black lines, alongside the experimental data. The error bars represent 95% confidence intervals obtained through bootstrapping, and the shaded area represents the 95% confidence interval for the theoretical calculation. Notably, the calculated residual MI depends solely on the imaging resolution. The figure indicates that our measured MI is significantly higher than what is theoretically expected to be the residual MI due to the imaging effect: For $N = 7$, where the effect of imaging is largest, our measured MI with 95% confidence interval is larger than the residual value. An alternative reading of the plot is to look at the lower modes, on which the imaging resolution has much less influence. For $N = 3$ for example, our measurement with 95% confidence interval reads $4.8367\,(1.1,\,6.0) \times 10^{-2}$, where the residual MI is an order of magnitude smaller, 2.2878×10^{-3}. This observation along with the states presented in fig. 5.2 shows that our measured MI can not be a residual MI caused by the finite imaging resolution.

We also explore the impact of the hard cut-off on the decay of MI. In fig. 5.9(a), we present information similar to fig. 5.6 for each value of N. In fig. 5.9(b), we plot the dependence of l_{fit} on the total number of modes, N. We find that experimental data and theoretical calculations are in good agreement for all values of N. As the

TU Bibliothek Your knowledge hub WIEN
Die approbierte gedruckte Originalversion dieser Dissertation ist an der TU Wien Bibliothek verfügbar.
The approved original version of this doctoral thesis is available in print at TU Wien Bibliothek.

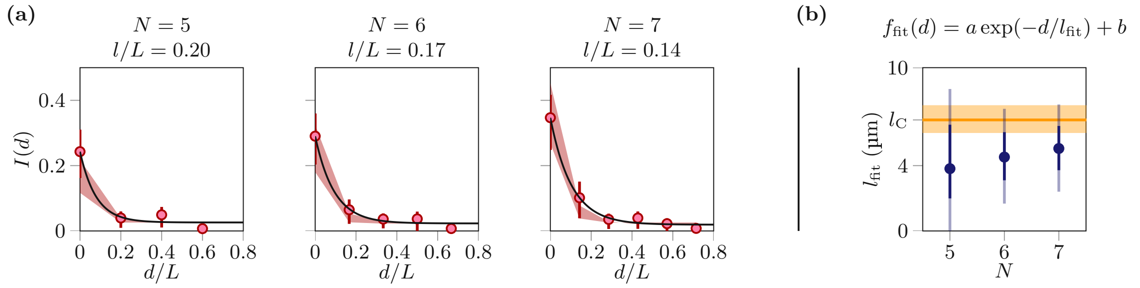

Figure 5.9 Effect of the total number of modes, N, on the decay length, l_{fit}. We **(a)** Similar quantities as shown in fig. 5.6 are plotted for measurement M2. Note that changing the total number of modes also changes the size of the sub-region. **(b)** The resulting decay length, l_{fit}, is plotted for different values of N. The solid part of the error bars represents the 68% confidence interval (standard error), and the extended transparent part represents the 95% confidence interval. The solid orange line and the shaded area show $\ell_{\text{J}} = 6.8\,(6.0, 7.7)\,\mu\text{m}$ and its 95% confidence interval.

number of modes decreases, sub-region size and spacing increase, resulting in larger error bars due to lower fit quality. However, the decay length remains consistent for different cut-offs. It is important to note that for $N < 5$, the sub-regions become too large, and reliable fitting is no longer feasible.

5.7 Outlook

Our results represent a step towards the more ambitious goal of measuring many-body entanglement in a continuous 1D quantum system. The reconstruction of the full covariance matrix enables the calculation of various entanglement measures applicable to both pure and mixed states, such as logarithmic negativity. However, two main limiting factors currently hinder the detection of entanglement. Firstly, a sufficient number of momentum modes with occupation numbers close to the ground state are required for entanglement detection. In our current experiments, the nonzero temperature (10 to 100 nK) of the Bose gas keeps the occupation numbers of the lower momentum modes significantly above the ground state value. Secondly, the finite optical resolution introduces a soft cut-off, which not only prevents the measurement of higher momentum modes but also modifies the lower modes that can be measured. Improvements in either of these aspects would enable the measurement of entanglement.

Another promising avenue for future research is to extend the analysis beyond quadratic models and detect entanglement in interacting models. Previous work has demonstrated that atom chip experiments can effectively simulate the sine-Gordon model, enabling the measurement of higher-order correlation functions [102]. Developing a tomography procedure for such a setting would grant access to entanglement properties in interacting many-body quantum systems [103, 104].

Chapter 6

Observation of curved light-cones

Post-quench propagation of correlations

After quantifying the correlations by measuring the mutual information in equilibrium, it's time to have a look at the propagation of the correlations after the quench. In contrast to the previous chapter, here we start by looking at the experimental results, namely the dynamics of the second-order correlations of a local field. This local field is the velocity field (the derivative of the relative phase). The reason is that in this case, the experimental measurements and the results are very illustrative. Hence, after a brief introduction, I present the experimental protocol, the quantification of the correlations, and then discuss the quantum field theoretical description, based on the introduction from chapter 2. Parts of this chapter have been published in [46], with some parts having substantial overlap, and others being borrowed verbatim.

6.1 Quantum field simulation on a curved background

Our pair of tunneling-coupled 1D condensates is capable of simulating the Klein-Gordon (KG) Hamiltonian introduced in section 2.2.3. In the previous chapter, we measured entropies and mutual information for thermal equilibrium states prepared in a strongly coupled double well and showed that they agree with the KG model. Those measurements were restricted to homogeneous background densities to make both the reconstruction of field quadratures and theory calculations easier.

In this chapter, we adjust the background density and consecutively the speed of sound, $v(z)$, to simulate the KG model with an inhomogeneous metric, defined as

$$g^{\mu\nu} = \begin{pmatrix} -v(z)^{-2} & 0 \\ 0 & 1 \end{pmatrix} . \tag{6.1}$$

For this purpose, it is instructive to write down the action corresponding to the KG Hamiltonian in $1+1$ space-time dimensions,

$$\mathcal{S}[\varphi] \sim \int \mathrm{d}z \mathrm{d}t \sqrt{-g} K(z) \left[g^{\mu\nu} (\partial_\mu \varphi)(\partial_\nu \varphi) + \tfrac{1}{2} M^2 \varphi^2 \right] . \tag{6.2}$$

Here we used the Einstein notation for the summation of indices. Furthermore, $g = \det(g_{\mu\nu}) = -v(z)^2$, M is the KG mass, and $K(z)$ is the space-dependent Luttinger parameter

$$K(z) = \frac{\hbar\pi}{2} \sqrt{\frac{\rho_0(z)}{m g_{1\mathrm{D}}}} . \tag{6.3}$$

The space-dependent speed of sound is related to the microscopic parameters as

$$v(z) = \sqrt{\frac{g_{1\mathrm{D}} \rho_0(z)}{m}} , \tag{6.4}$$

Hence, adjusting the local density, $\rho_0(z)$, by modifying the trapping potential enables the manipulation of the main physical parameter in the simulated metric (6.1). Since we do not change the background density over time in the experiment, we consider $v(z)$ and $K(z)$ to be time-independent.

Note that in $1+1$ dimensions, Laplacian's conformal invariance prevents the absorption of $K(z)$ into the metric through a conformal transformation and must be included in the action for generality. However, we observe that the propagation of correlation fronts is primarily governed by the induced metric.

6.2 Experimental protocol and quantification of velocity field correlations

6.2.1 Initial states

Similar to the experiments presented in chapter 5, we start by cooling down the atoms in a double well potential with a high tunneling rate, such that the condensates are phase locked and are practically in a thermal equilibrium state of the KG Hamiltonian.

Background density	K_{max}	T (nK)	λ_T (µm)	ℓ_{J} (µm)	q
Homogeneous	47	51	19	4.0	4.7
Homogeneous 2	50	48	18	3.2	5.6
Inhomogeneous w. smoothed edges	44	41	19	2.5	7.6
Inhomogeneous w. sharp edges	68	86	16	3.1	5.2

Table 6.1 For every setting relevant parameters are listed: K_{max} is the Luttinger parameter calculated based on the maximum density, T the temperature, λ_T the thermal coherence length, and ℓ_{J} the correlation length.

In the measurements presented in this chapter, I use the digital micro-mirror device (DMD) to shape the 1D potential landscape and create various background density profiles, $\rho_0(z)$. In this chapter, I will discuss the results for three distinct cases presented in table 6.1. First, I present two measurements with homogeneous background densities denoted as *Homogeneous 1* and *Homogeneous 2*. The second case is an *Inhomogeneous* background density *with sharp edges*. In the third and the last case, I prepare atomic clouds with *Inhomogeneous* background densities *with smoothed edges*, which means the density slowly vanishes in the edges. The density profiles are shown in fig. 6.1(a).

6.2.2 Mass quench

To observe the propagation of the correlations, we initiate the dynamics by doing a quantum quench. We rapidly change the transverse potential from a double well with a high tunneling rate to an uncoupled double well. In the experiment, I implement the quench by ramping the radio frequency amplitude linearly in 2 ms to increase the barrier height. In theory, this change corresponds to a global mass quench from a massive to a massless KG model. In this context, global means that the mass is changed for every position at the same time. The system evolves according to a Tomonaga-Luttinger liquid Hamiltonian as discussed in section 5.5.3.

6.2.3 Observable

Similar to the previous chapter, the observable that we directly measure in the experiment is the spatially resolved relative phase, $\hat{\varphi}(z)$. But as we discussed in section 3.3.2, the relative phase has an ambiguity of 2π. In chapter 5, we used the TLL dynamics to fit the zero mode of the initial state from the phase diffusion. Here, we are not only interested in the initial state but also in the post-quench phase profiles. Hence, the

Die approbierte gedruckte Originalversion dieser Dissertation ist an der TU Wien Bibliothek verfügbar.
The approved original version of this doctoral thesis is available in print at TU Wien Bibliothek.
TU Bibliothek WIEN Your knowledge hub

phase ambiguity for later times can only be solved by subtracting the phase at a reference point from the whole phase profile, $\hat{\varphi}_{\mathrm{ref}} = \hat{\varphi}(z) - \hat{\varphi}(z_{\mathrm{ref}})$. It is common to use this quantity whenever we are not dealing with circular operators such as $\langle \cos(\hat{\varphi}(z)) \rangle$. For example, Thomas Schweigler used this observable to calculate higher-order correlations and I use the same definition in the tomography process (see eq. (5.47)). The main purpose of this subtraction is to get rid of the zero mode and the ambiguity therein. But such a subtraction has a deeper impact: It kills the *locality* of the phase observable as it injects the information from point z_{ref} to every other point in the space. This issue prevents us from using it to detect the light-cone propagation of correlations in this chapter, forcing us to use another quantity.

To directly observe the light-cone dynamics, we need a local observable. To solve this issue, we use the velocity field, which is proportional to the first derivative of the phase field,

$$\hat{u}(z) = \frac{\hbar}{m} \partial_z \hat{\varphi}(z) \; . \tag{6.5}$$

This field is related to the particle current, $\hat{j}(z) = \rho_0(z)\hat{u}(z)$, which along with the particle density, $\rho_0(z)$, is one of the fundamental fields in the effective hydrodynamic description. Note that taking the spatial derivative erases the zero mode without affecting the locality.

To estimate the velocity field from the experimental data, we replace the derivative with the finite difference operator

$$\hat{u}(z) \approx \frac{\hbar}{m} \Delta_z \hat{\varphi}(z) \; , \tag{6.6}$$

with

$$\Delta_z \hat{\varphi}(z) = \frac{\hat{\varphi}(z + \Delta z) - \hat{\varphi}(z)}{\Delta z} \; . \tag{6.7}$$

Here, $\Delta z = 2\,\mu\mathrm{m}$ is the camera pixel size on the plane of atoms of the vertical imaging system. Which is smaller than the imaging resolution, $\sigma_{\mathrm{PSF}} \approx 3\,\mu\mathrm{m}$, as mentioned in chapter 3.

Since the initial state is balanced, meaning that the number of atoms in both wells is the same, ideally, the quench will not induce any flow in the system, meaning that the average current is zero, $\langle \hat{j}(z) \rangle = 0$. Instead, the dynamics manifest in the second-order correlations of the velocity field, $C_u(z, z') = \langle \hat{u}(z)\hat{u}(z') \rangle$. Similar to other sections of this thesis, we calculate the expectation values by taking the ensemble average over

Die approbierte gedruckte Originalversion dieser Dissertation ist an der TU Wien Bibliothek verfügbar.
The approved original version of this doctoral thesis is available in print at TU Wien Bibliothek.
TU Bibliothek WIEN Your knowledge hub

many experimental realizations, usually more than two hundred. In the next section, we show and discuss the experimental data.

6.3 Experimental results

6.3.1 Second order correlations of the velocity field

For the three cases introduced in section 6.2.1, we measured the two-point correlation functions of the velocity field, $C_u(z, z') = \langle \hat{u}(z)\hat{u}(z') \rangle$, at different times, with $t = -2\,\mathrm{ms}$ denoting the pre-quench time and $t \geq 0$ the post-quench times. The results for all evolution times are presented in figs. 6.9 and 6.10. For illustration purposes, we will focus on figs. 6.1 and 6.2 that summarize the results of different cases. In fig. 6.1(a), we plotted the average density $\rho_0(z)$ for three different cases.

A global mass quench does not induce an average flow in a balanced pair of tunneling-coupled condensates as we confirm experimentally by measuring the average velocity field. Although $\langle \hat{u}(z) \rangle = 0$, the correlations, $C_u(z, z')$, are nonzero, meaning that the fluctuations at positions z and z' are related. If the correlation is positive, then in every single shot of the experiment, the velocity fluctuations at z and z' tend to be aligned. On the other hand, negative correlations mean the velocity fluctuations point in opposite directions.

As our system simulates the thermal state of the KG model initially, the velocity field shows only short-range correlations, consisting of positive auto-correlations on the diagonal (red) and negative off-diagonal correlations (blue). The correlation lengths ℓ_J are listed in table 6.1. Since for $t = -2\,\mathrm{ms}$ the auto-correlations and the off-diagonal correlations overlap, it is not possible to extract the correlation length from the velocity field correlations. Nevertheless, comparing the numbers and the extent of the correlations in the 2D plots, shows that they are comparable.

To understand the post-quench dynamics, we appeal to the intuitive non-interacting quasi-particle picture. In this picture, pairs of initially correlated phonons carry the dynamics [105–107]. These pairs are shown in the yellow blobs in the space-time plots presented in fig. 6.1(b). Note that this description is justified since we are dealing with non-interacting quadratic Hamiltonians.

In all three settings, regardless of the trapping geometry, the positive auto-correlations persist. In the quasi-particle picture, these correlations are carried by co-moving phonons that were correlated before the quench, as demonstrated in fig. 6.1(b). The schematic also explains why these correlations appear to be static: These phonon

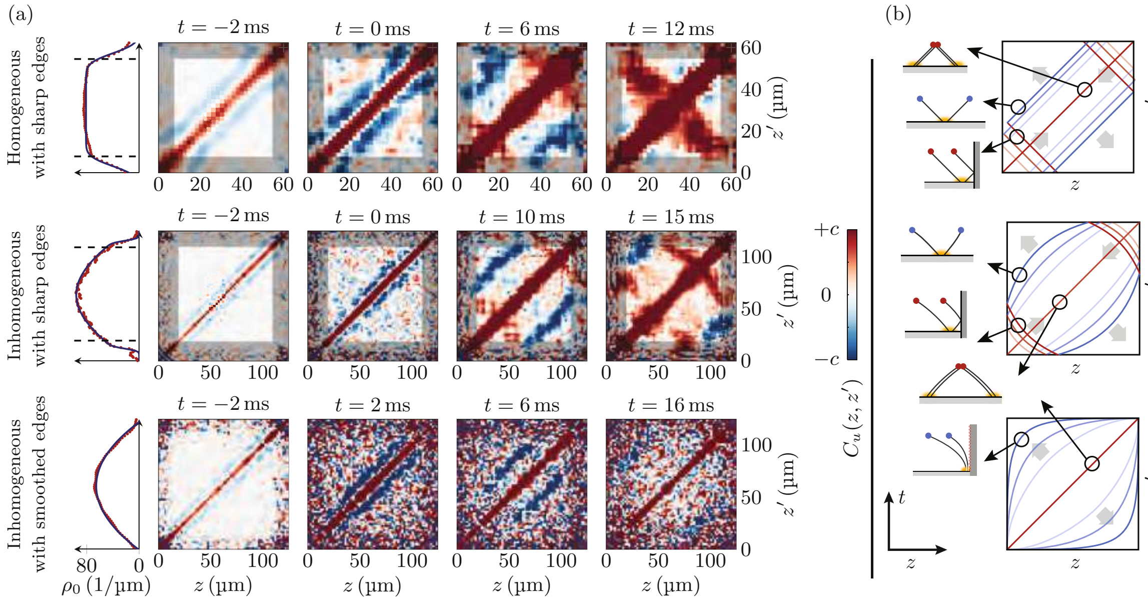

Figure 6.1 Propagation of the flat and curved fronts of the two-point correlation function of the velocity field. **(a)** The measurement results of $C_u(z, z')$ are shown at various times t, both before ($t = -2$) and after the quench ($t \geq 0$). Three different experimental settings are considered, each with a distinct background density profile, as explained on the left. In each case, the measured $\rho_0(z')$ is represented by red dots, and a fit is shown by the blue curves. **(b)** To provide an intuitive explanation of the correlation propagation fronts in different scenarios, we consider points marked with yellow dots at $t = 0$ that are initially correlated. Following the quench, the evolution of correlations between these two points is traced by the light-cone trajectories of the left- and right-moving chiral fields, as depicted in the space-time sketches. The presence of narrow-width fronts, their shape, and the sign of correlations are fully elucidated by considering the effects of reflection at the boundaries and the influence of the effectively curved metric.

pairs are moving with (almost) the same velocity and will stay close together at all evolution times, $z \approx z'$.

The dynamics of the anti-correlation fronts, on the other hand, are governed by the counter-moving phonon pairs. As time passes, the distance between these quasi-particles grows, and hence the correlation fronts move away from the diagonal as shown in the space-time plots of fig. 6.1(b). For a box-like trapping potential, the density profile is homogeneous. Hence, the anti-correlation fronts stay straight throughout the evolution. When the background density is inhomogeneous, the anti-correlation fronts deviate from straight lines. Assuming that there is no curvature in the initial short-ranged correlations, these curved fronts hint at the simulated curved metric. However,

TU Bibliothek WIEN Your knowledge hub
Die approbierte gedruckte Originalversion dieser Dissertation ist an der TU Wien Bibliothek verfügbar.
The approved original version of this doctoral thesis is available in print at TU Wien Bibliothek.

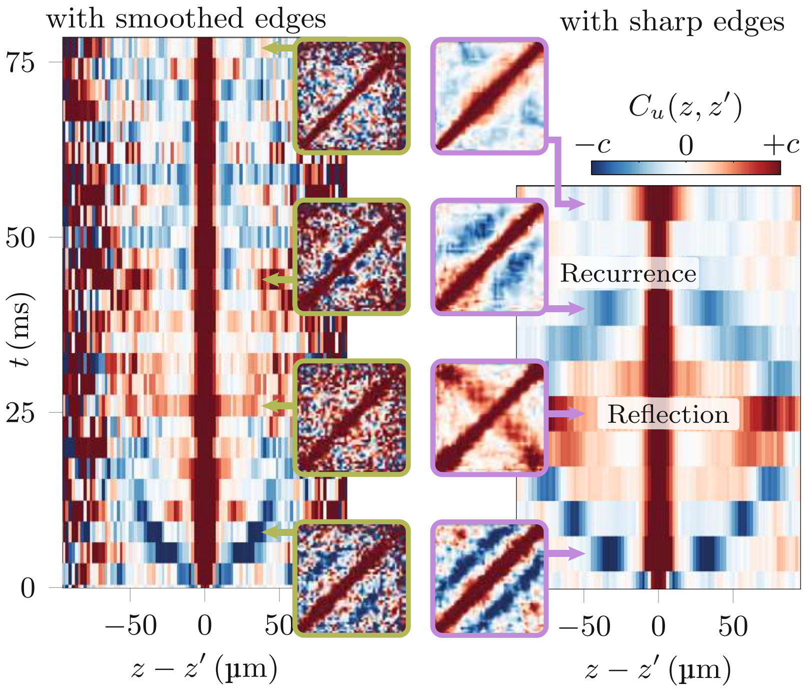

Figure 6.2 We observe light-cone propagation in the two-point correlation function of the velocity field, $C_u(z, z' = -z)$, in two experimental settings: one with sharp edges (right) and the other without sharp edges (left). In the main plots, we display the anti-diagonal correlations as a function of time. In the case with sharp edges in the density, we clearly observe reflection from the boundaries and recurrence, which is absent in the other case. For certain time steps, we also plot the full two-dimensional correlation function, similar to fig. 6.1.

the initial background density is already curved. Thus, to confirm the dynamics based on the curved metric, we further investigate the velocity of the front propagation in the next section. Nevertheless, it was exciting to directly observe these curved correlation fronts in our quantum field simulator.

The third type of correlation front occurs in systems with sharp boundaries where the density vanishes abruptly [108] (first two rows of fig. 6.1). In these cases, we observe positive anti-diagonal fronts emerging from the boundaries and moving inwards. As illustrated by reflected trajectories in fig. 6.1(b), the dynamics are carried by two initially counter-propagating phonons, one of which was reflected from the boundaries and moving in the same direction as the other one.

A noteworthy effect that we observe in cases with a sharp-edged background density is the so-called 'rainbow' pattern: In half a recurrence time, the positive anti-correlation front extends across the entire system (See the homogeneous cases at $t = 12\,\mathrm{ms}$ in

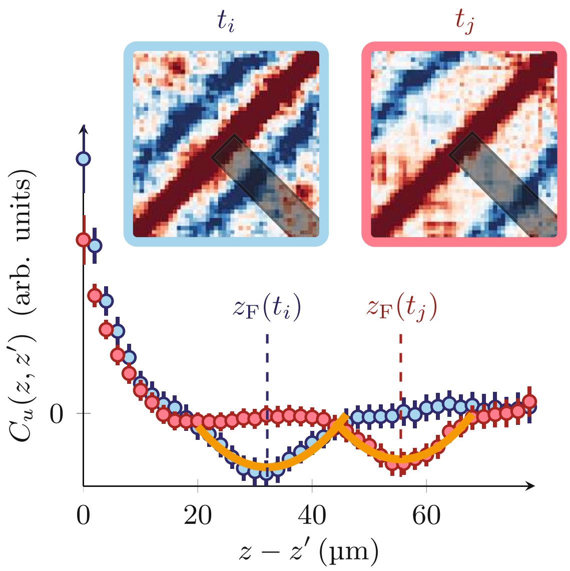

Figure 6.3 Fitting the correlation front positions at different times. For each time, we average along the diagonal of $C_u(z, z')$ to reduce the noise. The results are plotted in blue and red for $t_i < t_j$. The error bars are the standard error of the mean. Orange curves are the parabolic fits. The extracted positions are used to calculate the front velocities with eq. (6.8). The estimated positions are plotted in fig. 6.4 and the front velocities in fig. 6.5.

fig. 6.9 and inhomogeneous case with sharp edges at $t = 25\,\mathrm{ms}$). Additionally, this plot provides new insights into the system dynamics: the quench dynamics have transformed the initial thermal correlations into a configuration resembling the well-known 'rainbow' pattern [109]. The term 'rainbow' is a descriptive way to denote configurations where correlations exist only between pairs of points that are symmetric with respect to the middle. In a correlation matrix displaying an X-shaped pattern, aside from the autocorrelations along the diagonal, correlations also exist between pairs of points $(z, L - z)$ along the anti-diagonal.

In the case with soft boundaries (third row in fig. 6.1), no anti-diagonal fronts appear, signaling the absence of reflections. This is in accordance with the presence (absence) of reflections for the off-diagonal anti-correlation fronts for sharp (smoothed) edges, presented in fig. 6.2. In the presence of sharp edges, the anti-correlation fronts change direction and return to their initial position, resulting in an approximate but clearly visible recurrence of the correlations (see [17]). In contrast, for the soft boundary, we observe the slow-down of the anti-correlation fronts and the absence of reflections and recurrences at longer times.

Die approbierte gedruckte Originalversion dieser Dissertation ist an der TU Wien Bibliothek verfügbar.
The approved original version of this doctoral thesis is available in print at TU Wien Bibliothek.
TU Bibliothek WIEN Your knowledge hub

6.3.2 Correlation front velocity

In order to show that the evolution of the correlations is given by the curved metric, we take a step further to estimate the front velocity, $v_{\mathrm{F}}(t)$. As demonstrated in fig. 6.3, we first estimate the front position. We take a slice of $C_u(z, z')$ along the anti-diagonal, $z' = -z$, and calculate the mean value of $5 - 11$ neighboring pixels. We take the average to reduce the effect of noisy pixels. We show two of such averaged slices in fig. 6.3 at times t_i and t_j. The position of the fronts appears at local minima in these profiles. We quantitatively determine the positions by fitting a parabola to the vicinity of the local minima. This fitting interval is chosen manually. The orange curves in fig. 6.3 are the fitted parabola, whose minima are the estimated positions of the fronts, $z_{\mathrm{F}}(t_i)$ and $z_{\mathrm{F}}(t_j)$. The estimated correlation front positions are plotted in fig. 6.4. We use bootstrapping with 2222 resampling to calculate 68% confidence intervals. Now, the average front velocity at time t is

$$v_{\mathrm{F}}(t) = \frac{z_{\mathrm{F}}(t_i) - z_{\mathrm{F}}(t_j)}{t_i - t_j}\,, \qquad t = \frac{t_i + t_j}{2}\,. \tag{6.8}$$

The measured velocities along with the theory calculations are shown in fig. 6.5. In these figures, we compare the measured $v_{\mathrm{F}}(t)$ (blue circles) with the theoretical prediction (red line) and a constant velocity (orange line). We will discuss the theory in the upcoming sections. The constant velocity is the mean value of all the data points (except the middle value in fig. 6.5). To quantify the agreement between the experimental measurements and the theory, we calculate the reduced χ^2 for N data points defined as

$$\chi^2_{\mathrm{red}} = \frac{1}{N-1} \sum_{i=1}^{N} \frac{\left(v_{\mathrm{F}}(t_i) - v_{\mathrm{F}}^{\mathrm{theo}}(t_i)\right)^2}{\sigma_i^2}\,, \tag{6.9}$$

where σ_i is the standard error of the mean. Here we use half of the 68% confidence interval obtained via bootstrapping.

In the homogeneous case, the measured front propagation is consistent with a constant velocity (a horizontal line in fig. 6.5(a)). For the inhomogeneous density profiles, shown in fig. 6.5(b) and (c), the effective velocities depend on the position in accordance with the theoretically predicted inhomogeneous metric.

The reflection of the correlation front is also clearly visible in fig. 6.5(b) and we find a reasonable agreement to the free Gaussian model (6.2). Therein, if the velocity decreases slower than linearly towards the boundary, the traveling time diverges, so there is

TU Bibliothek WIEN Your knowledge hub
Die approbierte gedruckte Originalversion dieser Dissertation ist an der TU Wien Bibliothek verfügbar.
The approved original version of this doctoral thesis is available in print at TU Wien Bibliothek.

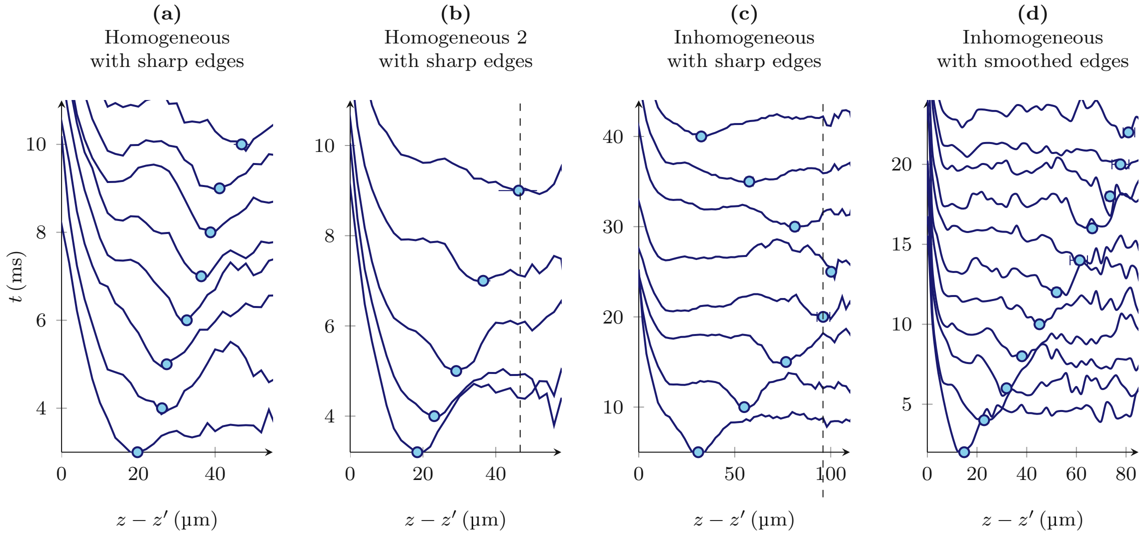
(a) Homogeneous with sharp edges

(b) Homogeneous 2 with sharp edges

(c) Inhomogeneous with sharp edges

(d) Inhomogeneous with smoothed edges

Figure 6.4 Estimated correlation front positions. The positions of the fronts (light blue circles) at different times for the four settings presented in section 6.2.1. Dark blue curves are the anti-diagonal correlations similar to fig. 6.3 (presented as lines only for illustration purposes).

neither reflection nor turn. Therefore, light-like trajectories converge asymptotically to the boundary, in agreement with the geodesics of eq. (6.1). This is in agreement with experimental observations (see figs. 6.2 and 6.5(c)). Note however, that the Tomonaga-Luttinger liquid description is expected to break down near the edges due to vanishingly low atomic density [110] and hence the absence of reflections might be dominated by dispersive or higher-order corrections to the Gaussian model (6.2).

6.4 Theoretical description

For the theoretical investigation, we first unravel the connection between the action in eq. (6.2) and its corresponding Hamiltonian introduced in section 2.2.3. We then write the Heisenberg equations of motion for the velocity field and look at the solutions for different cases: First, we consider flat background densities in infinite space and in a finite-sized box. Then we consider inhomogeneous background densities. Finally, we discuss the subtle differences between our description with a typical Klein-Gordon Hamiltonian.

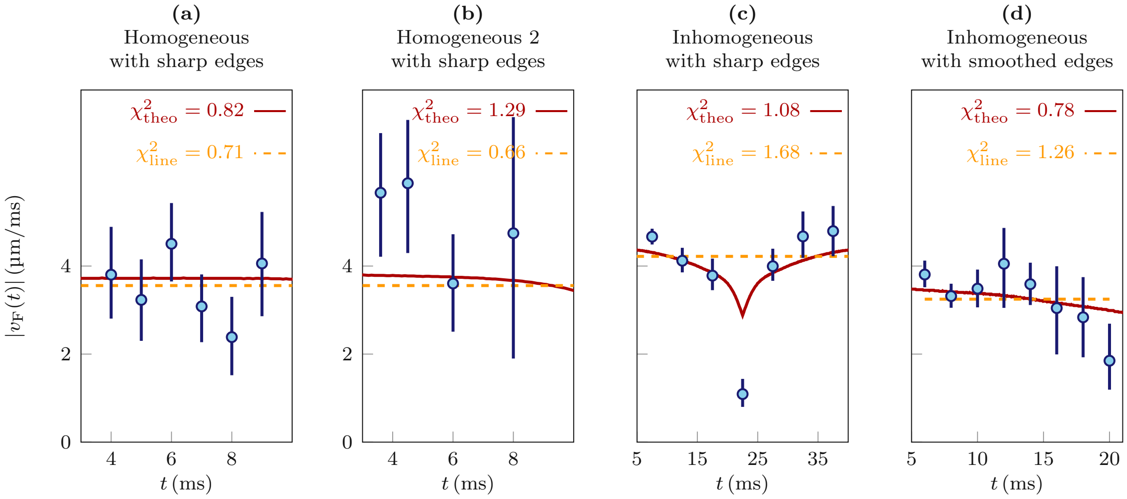

Figure 6.5 Estimation of correlation front velocity. We estimate the average front velocity for the four settings introduced in section 6.2.1. The extracted velocities are denoted by blue circles, and the error bars represent 68% confidence intervals obtained through bootstrapping [100]. The red lines correspond to twice the speed of sound calculated from the experimental local density, $\rho_0(z)$. Additionally, there is an orange vertical line marking the average value of the blue circles. To assess the goodness of fit, we calculate the reduced chi-squared values (χ^2) by comparing the red/orange curves with the blue circles. Note that we ignored the experimental data point in the middle in **(c)** while calculating the reduced χ^2.

6.4.1 From action to Hamiltonian

Here, I first write down the so-called *inhomogeneous* Tomonaga-Luttinger liquid Hamiltonian with a space-dependent Luttinger parameter, associated with the post-quench action introduced at the beginning of the chapter. Then, I will point out the difference between this Hamiltonian and the *homogeneous* counterpart, where the Luttinger parameter is a constant.

Space-dependent Luttinger parameter $K(z)$

To explain our experimental observations, we write down the Hamiltonian corresponding to the action in eq. (6.2), that is the KG equation introduced in section 2.2.3,

$$\hat{H}_{\text{KG}} = \int dz \left[g\,\delta\hat{\rho}^2(z) + \frac{\hbar^2\rho_0(z)}{4m}\left(\frac{\partial\hat{\varphi}(z)}{\partial z}\right)^2 + \hbar J\rho_0(z)\hat{\varphi}^2(z) \right] . \tag{6.10}$$

Similar to section 5.4.1, we rewrite this Hamiltonian in terms of macroscopic parameters

$$v(z) = \sqrt{\frac{g_{\mathrm{1D}}\rho_0(z)}{m}} \,, \tag{6.11}$$

$$K(z) = \frac{\hbar\pi}{2}\sqrt{\frac{\rho_0(z)}{m g_{\mathrm{1D}}}} \,, \tag{6.12}$$

$$\tilde{M} = \sqrt{\frac{8mJ}{\hbar}} = \frac{\sqrt{2}}{\ell_J} \,, \tag{6.13}$$

where speed of sound $v(z)$, Luttinger parameter $K(z)$, and the correlation length ℓ_J (eq. (2.37)) have been introduced before. Here $\tilde{M}$ is a Klein-Gordon mass with units m^{-1} not to be confused with the one introduced in section 5.4.1. The Hamiltonian thus can be written as the sum of an inhomogeneous Tomonaga-Luttinger liquid term plus a mass term as

$$\hat{H}_{\mathrm{KG}} = \hat{H}_{\mathrm{TLL}} + \frac{\tilde{M}^2}{2}\int \mathrm{d}z\, v(z)K(z)\varphi^2(z) \,, \tag{6.14}$$

with

$$\hat{H}_{\mathrm{TLL}} = \frac{\hbar}{2}\int dz\, v(z)\left[\frac{\pi}{K(z)}\delta\rho^2(z) + \frac{K(z)}{\pi}\left(\partial_z\varphi(z)\right)^2\right] . \tag{6.15}$$

Through Heisenberg's equation of motion, we find the relation between the density quadrature $\delta\hat{\rho}$ and the time derivative of the phase field as

$$\begin{aligned}
\partial_t\hat{\varphi}(z,t) &= \frac{\mathrm{i}}{\hbar}[H_{\mathrm{KG}}, \hat{\varphi}(z,t)] \\
&= \frac{ig_{\mathrm{1D}}}{\hbar}\int \mathrm{d}z'\Big(\delta\hat{\rho}(z',t)[\delta\hat{\rho}(z',t),\hat{\varphi}(z,t)] + [\delta\hat{\rho}(z',t),\hat{\varphi}(z,t)]\delta\hat{\rho}(z',t)\Big) \\
&= \frac{-2g_{\mathrm{1D}}}{\hbar}\int \mathrm{d}z'\delta(z'-z)\delta\hat{\rho}(z',t) \\
&= \frac{-2g_{\mathrm{1D}}}{\hbar}\delta\hat{\rho}(z,t) \\
&= \frac{-\pi v(z)}{K(z)}\delta\hat{\rho}(z,t) \,.
\end{aligned} \tag{6.16}$$

Replacing (6.16) in (6.15) yields

$$\begin{aligned}\hat{H}_{\mathrm{TLL}} &= \frac{\hbar}{2}\int \mathrm{d}z\, v(z)\left[\frac{K(z)}{\pi}\left(\partial_z\hat{\varphi}(z)\right)^2 + \frac{\pi}{K(z)}\delta\hat{\rho}^2(z)\right]\\ &= \frac{\hbar}{2}\int \mathrm{d}z\left[\frac{K(z)v(z)}{\pi}\left(\partial_z\hat{\varphi}(z)\right)^2 + \frac{K(z)}{\pi v(z)}\left(\partial_t\hat{\varphi}(z)\right)^2\right]\\ &= \frac{\hbar}{2\pi}\int \mathrm{d}z\, K(z)\left[v(z)\left(\partial_z\hat{\varphi}(z)\right)^2 + v(z)^{-1}\left(\partial_t\hat{\varphi}(z)\right)^2\right]\\ &= \frac{\hbar}{2\pi}\int \mathrm{d}z\, v(z)K(z)\left[\left(\partial_z\hat{\varphi}(z)\right)^2 + v(z)^{-2}\left(\partial_t\hat{\varphi}(z)\right)^2\right]. \end{aligned} \tag{6.17}$$

It is important to mention the space dependence of $K(z)$ in eq. (6.17). In literature, a TLL Hamiltonian with a space-dependent Luttinger parameter is often called an *inhomogeneous* TLL Hamiltonian. It is important not to mix the term "inhomogeneous" in this context with a *non-flat* background density, that is space-dependent $v(z)$ and $\rho_0(z)$. I will introduce the Hamiltonian and its associated action at the end of this section and will compare the dynamics of the correlations for non-flat densities in Sec. ??. For now, let's put $\hat{H}_{\mathrm{TLL}}$ and the mass term back together,

$$\hat{H}_{\mathrm{KG}} = \frac{\hbar}{2\pi}\int \mathrm{d}z\, v(z)K(z)\left[v(z)^{-2}\left(\partial_t\hat{\varphi}(z)\right)^2 + \left(\partial_z\hat{\varphi}(z)\right)^2 + \frac{\tilde{M}^2}{2}\varphi(z)^2\right]. \tag{6.18}$$

Finally, setting the two non-trivial elements of the metric to be $g^{tt} = -v(z)^{-2}$ and $g^{zz} = 1$ and hence $\sqrt{-\det(g_{\mu\nu})} = v(z)$, leads to the Lagrangian density in eq. (6.2).

Constant Luttinger parameter K

As mentioned before, in theory, we can write an action with a constant Luttinger parameter $K(z) \equiv K = \text{const.}$, but space-dependent sound velocity $v(z)$ as

$$\mathcal{S}[\phi]\sim K\int \mathrm{d}z\mathrm{d}t\sqrt{-g}\left[g^{\mu\nu}(\partial_\mu\phi)(\partial_\nu\phi) + \tfrac{1}{2}\tilde{M}^2\phi^2\right]. \tag{6.19}$$

This is the action corresponding to *homogeneous* Klein-Gordon theory (hKG),

$$\hat{H}_{\mathrm{hKG}} = \hat{H}_{\mathrm{hTLL}} + \frac{\tilde{M}^2}{2}\int \mathrm{d}z\, v(z)K\phi^2(z)\,, \tag{6.20}$$

with the *homogeneous* Tomanaga-Luttinger liquid theory (hTLL) written as

$$\hat{H}_{\mathrm{hTLL}} = \frac{\hbar}{2}\int dz\, v(z)\left[\frac{\pi}{K}\delta\varrho^2(z) + \frac{K}{\pi}\left(\partial_z\phi(z)\right)^2\right]. \tag{6.21}$$

Note that for the rest of this chapter, I will use $\hat{\phi}$ and $\hat{\varrho}$ instead of $\hat{\varphi}$ and $\hat{\rho}$ to distinguish between the two field theories.

Following the calculation in eq. (6.16),

$$\partial_t \hat{\phi}(z,t) = \frac{\mathrm{i}}{\hbar}[H_{\mathrm{hTLL}}, \hat{\phi}(z,t)] = \frac{-\pi}{K} v(z) \delta\hat{\varrho}(z,t)\ . \tag{6.22}$$

$$\hat{H}_{\mathrm{hKG}} = \frac{\hbar K}{2\pi} \int \mathrm{d}z\, v(z) \Big[v(z)^{-2} (\partial_t \hat{\phi}(z))^2 + \Big(\partial_z \hat{\phi}(z)\Big)^2 + \frac{\tilde{M}^2}{2} \phi(z)^2 \Big]\ . \tag{6.23}$$

6.4.2 Heisenberg equations of motion

Let's calculate the equation of motion for the velocity field $\hat{u}(z,t)$ using the previously introduced Hamiltonians.

Space-dependent Luttinger parameter $K(z)$

We already worked out the equation of motion for the relative phase field in eq. (6.16). For $\delta\hat{\rho}$, we write

$$\begin{aligned}
\partial_t \delta\hat{\rho}(z,t) &= \frac{\mathrm{i}}{\hbar}[\hat{H}_{\mathrm{TLL}}, \delta\hat{\rho}(z,t)] \\
&= \frac{i\hbar}{4m} \int \mathrm{d}z' \Big(\partial_{z'} \rho_0(z') \hat{\varphi}(z',t) \partial_{z'} [\hat{\varphi}(z',t), \delta\hat{\rho}(z,t)] \\
&\quad + (\partial_{z'} [\hat{\varphi}(z',t), \delta\hat{\rho}(z,t)]) \partial_{z'} \hat{\varphi}(z',t) \Big) \\
&= \frac{\hbar}{2m} \int \mathrm{d}z' \rho_0(z') \partial_{z'} \hat{\varphi}(z',t) \cdot \partial_{z'} \delta(z-z') \\
&= \frac{\hbar}{2m} \rho_0(z') \partial_{z'} \hat{\varphi}(z',t) \cdot \delta(z-z') |_{z'=0}^{z'=L} \\
&\quad - \frac{\hbar}{2m} \int \mathrm{d}z' \partial_{z'} \Big(\rho_0(z') \partial_{z'} \hat{\varphi}(z',t) \Big) \delta(z-z') \\
&= -\frac{\hbar}{2m} \int \mathrm{d}z' \partial_{z'} \Big(\rho_0(z') \partial_{z'} \hat{\varphi}(z',t) \Big) \delta(z-z') \\
&= -\frac{\hbar}{2m} \partial_z \Big(\rho_0(z) \partial_z \hat{\varphi}(z,t) \Big)
\end{aligned} \tag{6.24}$$

Note that similar to section 5.5.3, we have assumed a vanishing velocity field at the boundaries $\partial_{z'} \hat{\varphi}(z',t)|_{z'=0,\,L} = 0$. Using the definition of the velocity field and the fact that $\partial_t\partial_z \equiv \partial_z\partial_t$, eqs. (6.16) and (6.24) can be written as

$$\partial_t \hat{u}(z,t) = -\frac{2g_{1\mathrm{D}}}{m}\partial_z \delta\hat{\rho}(z,t)\ , \tag{6.25}$$

$$\partial_t \delta\hat{\rho}(z,t) = -\frac{1}{2}\partial_z(\rho_0(z)\hat{u}(z,t))\ . \tag{6.26}$$

Taking another time derivative yields two decoupled equations,

$$\partial_t^2 \hat{u}(z,t) = \partial_z^2(v^2(z)\hat{u}(z,t))\ , \tag{6.27}$$

$$\partial_t^2 \delta\hat{\rho}(z,t) = \partial_z(v^2(z)\partial_z\delta\hat{\rho}(z,t))\ . \tag{6.28}$$

Constant Luttinger parameter K

In this case, we also have the equation of motion for the phase field in eq. (6.22). Similar to eq. (6.24), we find

$$\partial_t \delta\hat{\varrho}(z,t) = \frac{\mathrm{i}}{\hbar}[\hat{H}_{\mathrm{hTLL}}, \delta\hat{\varrho}(z,t)] = -\frac{K}{\pi}\partial_z(v(z)\partial_z\hat{\phi}(z,t))\ . \tag{6.29}$$

Defining $\hat{\boldsymbol{\mathfrak{u}}}(z) = \hbar\partial_z\hat{\phi}(z)/m$ and considering $\partial_t\partial_z \equiv \partial_z\partial_t$, we get

$$\partial_t \hat{\boldsymbol{\mathfrak{u}}}(z,t) = -\frac{\pi}{K}\partial_z(v(z)\delta\hat{\varrho}(z,t))\ , \tag{6.30}$$

$$\partial_t \delta\hat{\varrho}(z,t) = -\frac{K}{\pi}\partial_z(v(z)\hat{\boldsymbol{\mathfrak{u}}}(z,t))\ . \tag{6.31}$$

Taking another time derivative yields two decoupled equations for the homogeneous case,

$$\partial_t^2 \hat{\boldsymbol{\mathfrak{u}}}(z,t) = \partial_z\left[v(z)\partial_z(v(z)\hat{\boldsymbol{\mathfrak{u}}}(z,t))\right]\ , \tag{6.32}$$

$$\partial_t^2 \delta\hat{\varrho}(z,t) = \partial_z\left[v(z)\partial_z(v(z)\delta\hat{\varrho}(z,t))\right]\ . \tag{6.33}$$

Remarks

We have obtained the decoupled equations of motion for the velocity field and the relative density fluctuations for both inhomogeneous (eqs. (6.27) and (6.28)) and homogeneous (eqs. (6.32) and (6.33)) TLL Hamiltonians. There are two important remarks that should be pointed out:

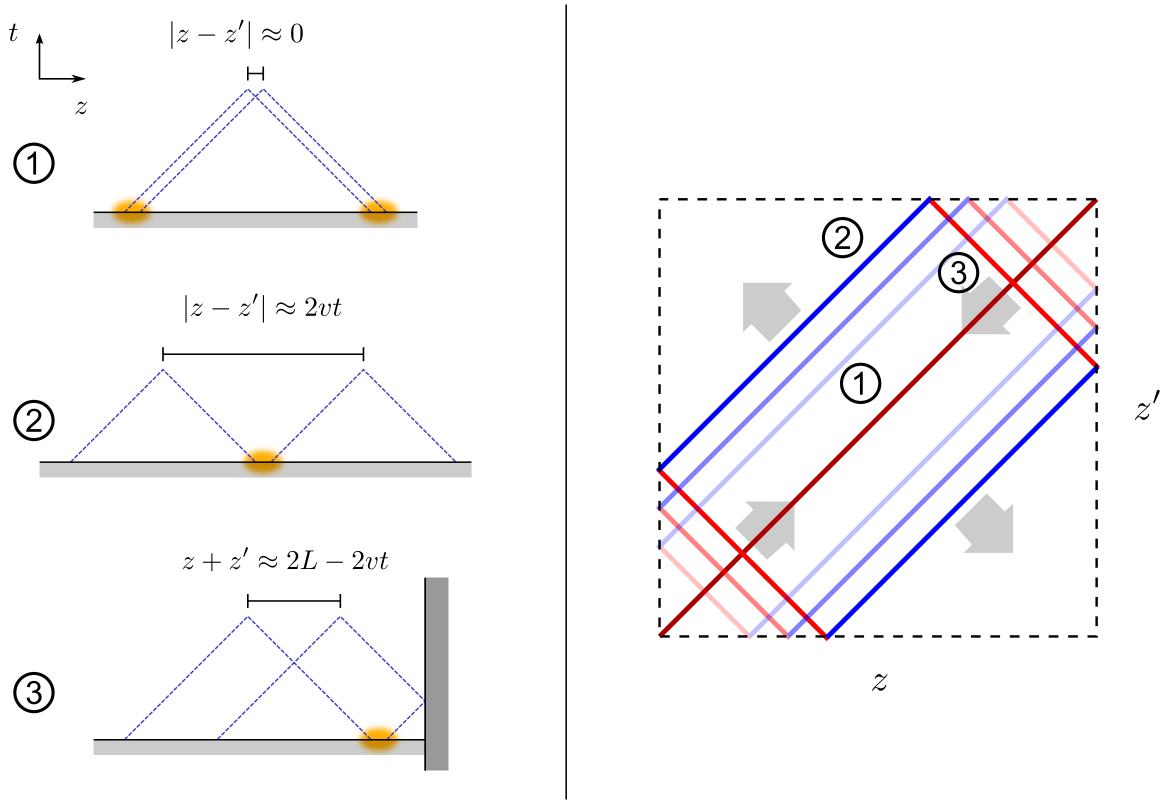

Figure 6.6 Illustrative explanation of the correlation propagation fronts in a finite box with a flat metric. Equilibrium states of massive fields are characterized by correlation functions that decay exponentially with the distance, and here we consider initial states of this type with a correlation length ℓ_J much smaller than the system size L. Following the quench to the massless phase, the time evolution of correlations between two points in space can be understood by backward tracing the light-cone trajectories of left- and right-moving chiral fields. Correlations are significant only if the light-cone projections of the two points to the initial time surface are close to each other, i.e., at a distance of the order $\ell_J > 0$. The apex of the cones signifies that there are two sources of measured correlation, one from the left and one from the right. The gray solid baseline signifies the initial state and the orange shape is the extent of the initial correlation length. We can distinguish three cases: **(1)** Fields propagating in the same direction: these contribute only to diagonal correlations. **(2)** Fields propagating to opposite directions: these give rise to correlation fronts that appear parallel to the diagonal in the covariance matrix and move away from it at speed $2v$. **(3)** One of the propagating fields reflected at one of the boundaries: this case results in fronts perpendicular to the diagonal that move ‘inwards’.

- Obviously, these two sets of equations have different forms. In principle, this difference results in different dynamics. We will discuss the impact of an inhomogeneous Luttinger parameter later in section 6.4.4.

- Another important observation is the fact that the Luttinger parameter is absent from the equations of motion, regardless of spatial dependence. This is the first hint as to why the dynamics merely depend on $v(z)$.

6.4.3 Correlation fronts propagation

We are now ready to discuss the propagation of the correlation fronts. We first consider the flat background density in infinite space as well as in finite-sized box-like confinement. We then draw our attention to curved background densities.

Infinite space with flat background density

For a flat background density, $\rho_0(z) \equiv n_{1\mathrm{D}}$, the speed of sound is a constant, $v(z) \equiv v =$ const.. Hence, the equations of motion for both inhomogeneous (eqs. (6.27) and (6.28)) and homogeneous (eqs. (6.32) and (6.33)) TLL Hamiltonians, reduces to

$$\partial_t^2 \hat{u}(z,t) = v^2 \partial_z^2 \hat{u}(z,t) \ , \tag{6.34}$$

$$\partial_t^2 \delta\hat{\rho}(z,t) = v^2 \partial_z^2 \delta\hat{\rho}(z,t) \ . \tag{6.35}$$

In the following, we want to solve eq. (6.34) in infinite space. The initial conditions are given by $\hat{u}(z,0)$ and the time derivative

$$\partial_t \hat{u}(z,t)|_{t=0} = -\frac{\hbar\pi v}{mK} \partial_z \delta\hat{\rho}(z,0) = -\frac{2g_{1\mathrm{D}}}{m} \partial_z \delta\hat{\rho}(z,0) \ . \tag{6.36}$$

It is easy to show that a general solution for arbitrary initial conditions is

$$\hat{u}(z,t) = \frac{1}{2}\left[\hat{u}(z-vt,0) + \hat{u}(z+vt,0) + \frac{2g_{1\mathrm{D}}}{mv}\left(\delta\hat{\rho}(z-vt,0) - \delta\hat{\rho}(z+vt,0)\right)\right] \ , \tag{6.37}$$

which we will write in as

$$\hat{u}(z,t) = \sum_{\sigma=\pm 1} \hat{\chi}_\sigma(z+\sigma vt) \ , \tag{6.38}$$

with the left- and right-moving chiral fields defined as

$$\hat{\chi}_\sigma(z) \equiv \frac{1}{2}\left[\hat{u}(z,0) - \sigma\frac{2g_{1\mathrm{D}}}{mv}\delta\hat{\rho}(z,0)\right] . \tag{6.39}$$

The second-order correlations of the velocity field at time t are given as

$$C_u(z,z',t) = \langle \hat{u}(z,t)\hat{u}(z',t)\rangle = \sum_{\sigma_1,\sigma_2=\pm1} \langle \hat{\chi}_{\sigma_1}(z+\sigma_1 vt)\hat{\chi}_{\sigma_2}(z'+\sigma_2 vt)\rangle . \tag{6.40}$$

This equation suggests that the correlations between two points z and z' at time t are traced back to the initial correlations.

Given that initial correlations are short-ranged, there are only two possibilities for which the sum mentioned above can significantly contribute: either when $|z-z'| \approx 0$ (where $\sigma_1 = \sigma_2$), or when $|z-z'| \approx 2vt$ (where $\sigma_1 = -\sigma_2$). In the first case, fig. 6.6(1), the contribution is limited to correlations at nearby points for any time after the quench. In the second case, fig. 6.6(2), it leads to the propagation of a correlation front that effectively travels at a speed of $2v$. By " $\approx$ " above, we mean that the difference between the two sides is smaller than or of the same order as the initial correlation length.

In the experiment, quenching from a strongly coupled state, where the initial correlation length, $\ell_J = \sqrt{2}/\tilde{M} \approx 5\,\mu\mathrm{m}$, is much shorter than the system size $L \approx 50\,\mu\mathrm{m}$, the initial correlations of the density fluctuation have a larger contribution compared to those of the velocity field [19] in the later times. To show this dominance, we compare their momentum mode variances for the lower modes (small n),

$$\frac{\langle \delta\hat{\rho}_n^2\rangle}{\langle \hat{u}_n^2\rangle} \propto \frac{v^2k_n^2 + \tilde{M}^2 v^4/\hbar^2}{v^2k_n^2} \sim \left(\frac{L}{\ell_J}\right)^2 \gg 1 . \tag{6.41}$$

From eqs. (6.39) and (6.40), it becomes evident that the correlations after the quench are primarily influenced by the initial correlations of $\delta\hat{\rho}$. These initial correlations have a positive sign when $|z-z'| \approx 0$ (since $\sigma_1 = \sigma_2$) and a negative sign when $|z-z'| \approx 2vt$ (since $\sigma_1 = -\sigma_2$), explaining the observed negative sign of the propagating correlation fronts in the experimental data.

Finite-sized system with flat background density and hard-wall boundaries

Let us now consider the case of a finite system of size L and assume that the confining potential is a hard-wall well. This means that the particle current $\hat{j}(z)$ vanishes at the edges z for all times t, i.e., the boundary conditions imposed at $z = 0, L$ are of the

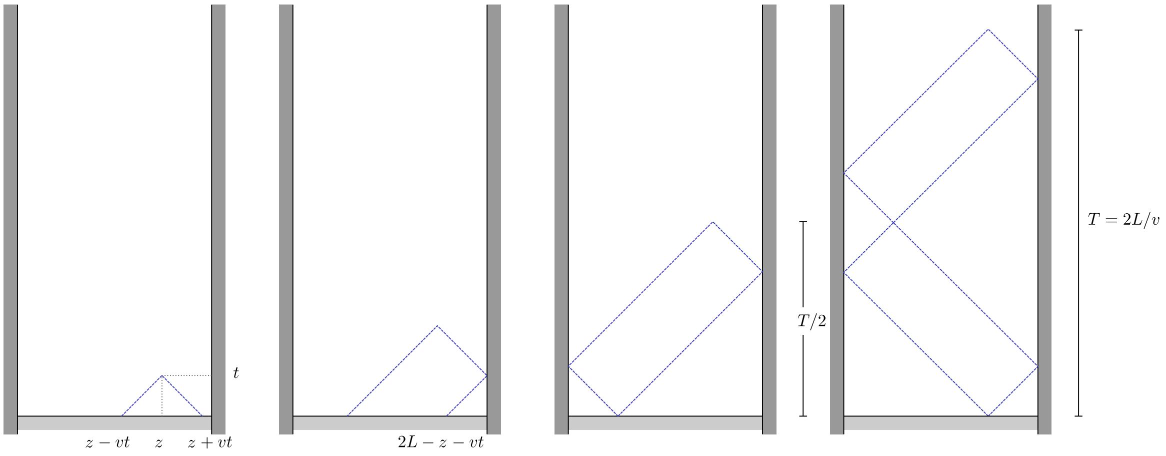

Figure 6.7 Geometric explanation of eq. (6.45). The positions from which the two chiral components of the field $\hat{u}$ at position z and time t originate are $z \pm vt$, if t is smaller than the first reflection time, $t < \min(t_L, t_R)$ with $t_L = z/v, t_R = (L-z)/v)$ corresponding to the reflection times at the left and right boundaries, respectively. After reflection at the left or right boundary, the origins of the reflected chiral components are the points $-z+vt$ or $2L-z-vt$, respectively. The first recurrence of the initial state occurs at $t = t_{\text{rec}} = 2L/v$. However, if the initial state is symmetric under space reflection $z \to L - z$ the correlations will exhibit a recurrence at $t = t_{\text{rec}}/2$.

Dirichlet type for the field $\hat{u}$ (i.e. Neumann type for the phase field)

$$\hat{u}(z,t)\big|_{z=0,L} = 0 \ . \tag{6.42}$$

The initial conditions of equation (6.34) and the range of the solution $\hat{u}(z,t)$ are now limited to the spatial interval $[0,L]$. However, we can easily account for the boundary conditions by making a simple modification to the previous problem. We extend the initial data beyond the interval $[0,L]$ to infinite space by reflecting the initial data at the two boundaries and periodically repeating them with a period of $2L$. With this approach, we can still use the solution derived for infinite space as given in equation (6.38). Nevertheless, to ensure that equation (6.42) is satisfied, the chiral fields must now adhere to the equations

$$\hat{\chi}_\sigma(z) = -\hat{\chi}_{-\sigma}(-z) \ , \tag{6.43}$$

$$\hat{\chi}_\sigma(z) = -\hat{\chi}_{-\sigma}(2L-z) \ . \tag{6.44}$$

In practice, these conditions account for the reflections at the boundaries as shown in fig. 6.7. The solution will take a more complicated form

$$\hat{u}(z,t) = \sum_{\sigma=\pm 1} \varsigma_\sigma(z,t)\hat{\chi}_{\sigma\varsigma_\sigma(z,t)}(|\zeta_\sigma(z,t)|) \ , \tag{6.45}$$

with

$$\zeta_\sigma(z,t) = (z+\sigma v t) \operatorname{mod}_{(-L)}(2L) \ , \tag{6.46}$$

and

$$\varsigma_\sigma(z,t) = \operatorname{sign}(\zeta_\sigma(z,t)) \ . \tag{6.47}$$

Here $x \operatorname{mod}_d p$ is the mod function with real arguments and offset d

$$x \operatorname{mod}_d p = ((x-d) \operatorname{mod} p) + d = x - p\left\lfloor \frac{x-d}{p} \right\rfloor \ , \tag{6.48}$$

where $\lfloor y \rfloor \equiv \text{floor}(y)$ is the flooring operator. From (6.43) and (6.44) it can be verified that the above solution satisfies the boundary conditions (6.42) for all times.

At the recurrence time,

$$t_{\text{rec}} = \frac{2L}{v} \tag{6.49}$$

the solution is identically equal to the initial value $\hat{u}(z,t_{\text{rec}}) = \hat{u}(z,0)$ for all points z in $[0,L]$. At the half a recurrence time, $t = t_{\text{rec}}/2$, the solution is equal to the initial value at the point corresponding to a reflection with respect to the middle point $\hat{u}(z,t_{\text{rec}}/2) = \hat{u}(L-z,0)$ (fig. 6.7).

In addition to the two possibilities mentioned earlier, namely $|z-z'| \approx 0$ or $|z-z'| \approx 2vt$ in the infinite space case, there is another significant contribution when we have hard boundaries. This contribution occurs when one or both of the backward propagating light-cone trajectories undergo one or more reflections at the boundaries. For instance, if only one of the trajectories experiences a reflection, the conditions are $(z+z') \approx 0$ if the reflection is at the left boundary, and $(z+z') \approx 2L-2vt$ if the reflection is at the right boundary as depicted in fig. 6.6(3). All three possibilities are shown in fig. 6.6.

Our analysis reveals that the time-evolved correlation functions are primarily significant near specific geometric locations of points that satisfy one of three equations: $|z-z'| = 0$, $|z-z'| = 2vt$, or $|z+\sigma z'| = |2nL + 2\sigma vt|$, where n is an integer and

$\sigma = \pm 1$. These locations in the (z, z') plane at a fixed time t form the union of the diagonal line $z = z'$ and a rectangle with vertices along the lines $z_{1,2} = 0, L$ and edges parallel and perpendicular to the diagonal, as depicted in Fig. 6.6.

The change in sign of correlations after reflections at the boundaries is explained by the corresponding change in sign of the propagating fields under the Dirichlet boundary conditions (6.42).

At the time $t = t_{\text{rec}}$, the correlations return to their initial values due to the symmetry of both the post-quench Hamiltonian and the initial state under spatial reflection with respect to the middle. However, since there is an additional symmetry, the period of correlation recurrence is $t_{\text{rec}}/2$ [17]. At $t = t_{\text{rec}}/4$, the correlations are mainly significant along the diagonal and the anti-diagonal $z' = L - z$, which explains the characteristic 'rainbow' configuration observed in the experimental data. These key points are crucial for understanding the patterns observed in the experimental correlations

Finite box with inhomogeneous metric

The next step is to introduce a non-flat background. For a non-vanishing speed of sound, $v(z) > 0$ for $0 \leq z \leq L$, the derivation of time-evolved correlations is similar to the previous case, except that the propagation time for excitations from z to z' is given by $|\tau(z', z)|$, where

$$\tau(z', z) = \int_z^{z'} \frac{\mathrm{d}l}{v(l)} \ . \tag{6.50}$$

Hence, to determine the shape of the correlation fronts at time t, we have to find all points z, z' such that there exist a point z_0 between them $(z \leq z_0 \leq z')$ so that

$$\tau(z', z_0) = -\tau(z, z_0) = t \ . \tag{6.51}$$

Note that without loss of generality, we have assumed $z \leq z'$. To determine z' as a function of z and t, we eliminate z_0 by writing

$$\tau(z', z) = \tau(z', z_0) - \tau(z, z_0) = 2t \ . \tag{6.52}$$

For the case where $z' \leq z$ only the sign changes. We summerize both cases in

$$\tau(z', z) = \pm 2t \ . \tag{6.53}$$

The equation suggests that the distance between two points corresponds to a travel time of $2t$ for a particle moving in either direction. Let $\tau_0(z)$ denote the travel time from a reference point, say the center of the system $z_0 = L/2$, to any other point z:

$$\tau_0(z) := \tau(z, z_0) \ . \tag{6.54}$$

The solutions $z'\pm$ of (6.53) as functions of z can then be expressed as:

$$z'\pm = \tau_0^{-1}\left(\tau_0(z) \pm 2t\right) \ . \tag{6.55}$$

It's important to note that τ_0 is invertible since its derivative is a positive function. If any of these solutions is beyond the edges, i.e., $z'+ > L$ or $z'- < 0$, we need to account for the time it takes to reach the edge and turn back. In such cases, we modify the solutions as follows:

$$z''_+ = \tau_0^{-1}\left(2\tau_0(L) - 2t - \tau_0(z)\right), \tag{6.56}$$

$$z''_- = \tau_0^{-1}\left(2\tau_0(0) + 2t - \tau_0(z)\right) \ . \tag{6.57}$$

The above equations (6.55, 6.56, 6.57) determine the shapes of the main and the reflected correlation fronts when the velocity does not vanish at any point, corresponding to fig. 6.8(1-3).

If the velocity $v(z)$ becomes zero at a certain position, such as at the system's boundaries, additional possibilities arise for the behavior of the time-evolved correlations. If $v(z)$ goes to zero rapidly at the edges, the time needed for a chiral field to travel from a point in the bulk to the edge can be finite. However, instead of reflection, the trajectory would have a turning point at the edge. Consequently, the correlation fronts become tangent to the edge lines (fig. 6.8(4)) instead of having a cusp.

On the other hand, if $v(z)$ goes to zero slowly at the edges, the time needed to reach the edge could be infinite. In this scenario, there would be neither reflection nor turning at the edge, and trajectories would instead converge to the edge asymptotically for large times (fig. 6.8(5)). Recurrences should also be absent in such cases, as their emergence relies on boundary reflection or turning. Therefore, in the large time limit, the correlations between all pairs of points in the bulk should approach steady-state values that are determined by initial correlations in the neighborhood of the boundary. To be more specific, if the velocity profile behaves as

$$\lim_{z\to z_b} v(z) = 0 \qquad \text{with } v(z) \sim |z - z_b|^\alpha, \tag{6.58}$$

Die approbierte gedruckte Originalversion dieser Dissertation ist an der TU Wien Bibliothek verfügbar.
The approved original version of this doctoral thesis is available in print at TU Wien Bibliothek.
TU Bibliothek WIEN Your knowledge hub

where z_b is the edge coordinate, then: For $\alpha < 1$, the traveling time to the edge, $\lim_{z\to z_b}\tau_0(z)$, remains finite. For $\alpha \geq 1$, the traveling time to the edge becomes infinite.

It is worth noting that the behavior described above also appears to apply to the case of a parabolic trap without hard walls. In the Thomas-Fermi limit, the density profile is approximately given by $\rho_0(z) \sim \mu - V(z) = -\frac{1}{2}\omega_z^2 z^2$. By diagonalizing the corresponding inhomogeneous Tomonaga-Luttinger liquid Hamiltonian (which can be achieved by expanding in Legendre polynomials instead of Fourier modes as the eigenfunctions), it is suggested that a significant quasi-recurrence should occur at a time $T = 2\pi R_{TF}/v_0 = \pi L/v_0$ [111], where R_{TF} is the Thomas-Fermi radius of the gas and v_0 is the speed of sound at the midpoint. However, this quasi-recurrence behavior is not observed in the experiment, indicating that reflections at the edges are suppressed. In fact, based on the density profile formula, one might expect the density to vanish at points $z = \pm R_{TF}$; however, this is not true since the formula is only valid in the bulk of the system. Near the edges ($z \approx \pm R_{TF}$), the Luttinger liquid description breaks down due to the extremely low density, and the density profile decays smoothly, as shown by the Gross-Pitaevski equation [110]. Understanding the dynamics of quasi-particles close to the edge is challenging due to the lack of a simple theoretical description, and the experimental resolution of the phase profiles in this region is hindered by the very low density. Nonetheless, the absence of recurrences in the experiment is indirect evidence that quasi-particle reflection or turning is unlikely to occur. It is reasonable to assume that the trajectories of quasi-particles converge asymptotically to the edges when the effective velocity profile decays slowly.

6.4.4 The effect of space-dependent Luttinger parameter

Let us compare the inhomogeneous TLL Hamiltonian that describes our system (6.17), with a typical homogeneous TLL Hamiltonian given by eq. (6.21). We mentioned earlier that in 1D, the space dependence of $K(z)$ can not be absorbed through a redefinition of the fields or coordinates [111, 112]. In our case, the spatial variation of $K(z)$ is governed by the same macroscopic parameter $\rho_0(z)$ as the sound velocity $v(z)$, which is a crucial quantity of interest in our analysis. Both $v(z)$ and $K(z)$ are proportional to $\sqrt{\rho_0(z)}$, so if $\rho_0(z)$ varies enough to visibly affect $v(z)$, it will similarly affect $K(z)$.

However, concerning quench correlations, the spatial dependence of $K(z)$ does influence the correlations but has no impact on the shape of correlation fronts. In the case under consideration, where $K(z) \propto v(z)$, the spatial variation of K leads to dispersive effects that violate the Huygens-Fresnel principle. This principle dictates that information propagates strictly along light-like trajectories. As a consequence,

Die approbierte gedruckte Originalversion dieser Dissertation ist an der TU Wien Bibliothek verfügbar.
The approved original version of this doctoral thesis is available in print at TU Wien Bibliothek.
TU Bibliothek Your knowledge hub WIEN

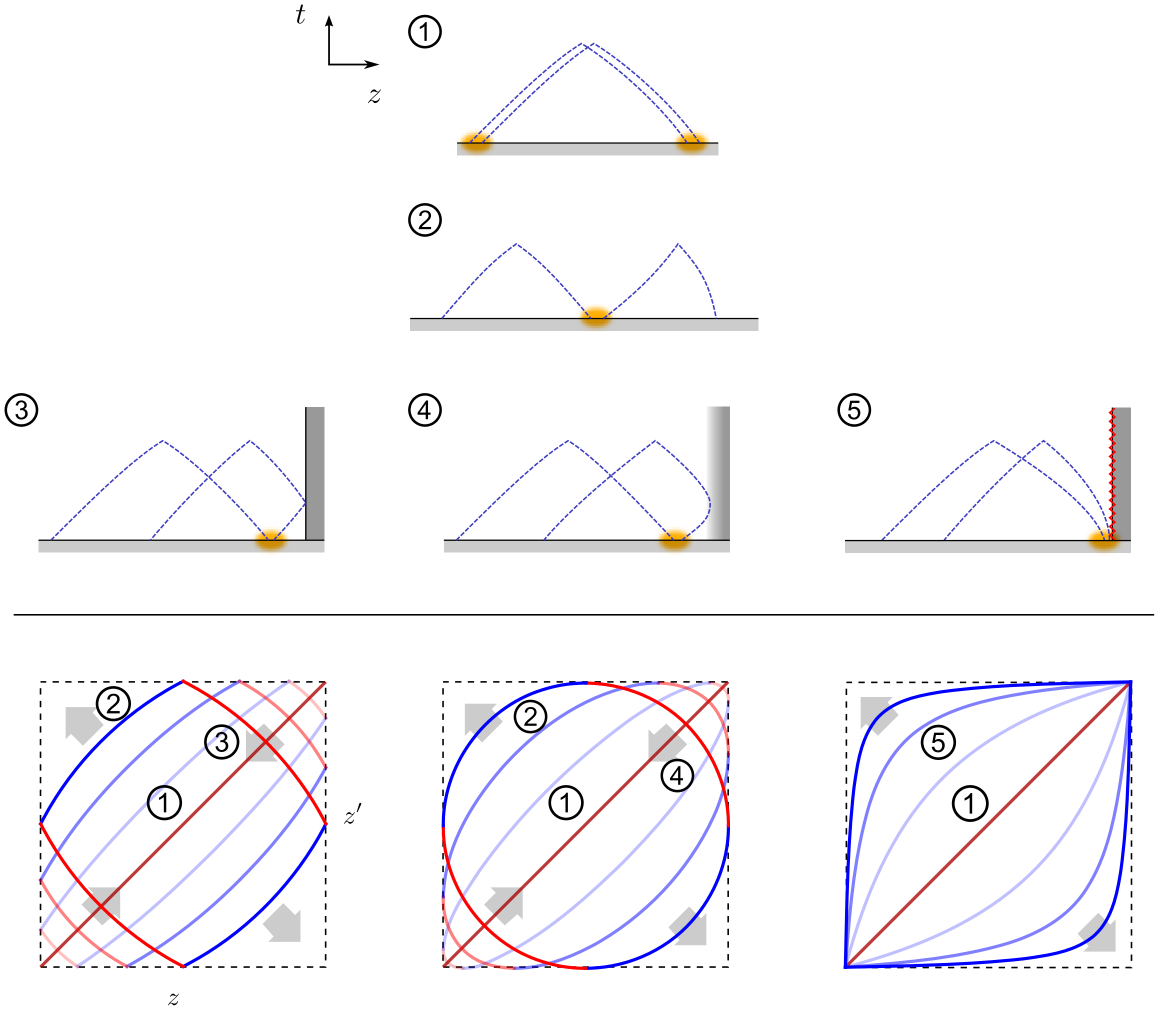

Figure 6.8 Illustrative explanation of the correlation propagation fronts in a finite box with a curved metric. Similar to fig. 6.6 but with a curved metric. As in the flat case, correlation dynamics can be derived by tracing the light-cone trajectories, which are now curved due to the spatial variation of the velocity $v(z)$, resulting in curved correlation fronts. Apart from the previously discussed cases **(1-3)**, additional possibilities alternative to **(3)** arise when $v(z)$ goes to zero at the edge **(4-5)**. If $v(z)$ decays sufficiently fast, then trajectories reach the boundary at finite time and have a turning point there **(4)**. If instead it decays sufficiently smoothly, then light-cone trajectories never reach the boundary, therefore they are neither reflected nor turned back, instead, they approach asymptotically the boundary **(5)**.

information propagation exhibits long tails behind the information fronts. Nevertheless, the front shape itself remains unaffected and is solely determined by $v(z)$. The analysis carried out in ref. [111] applies to Green's functions, which encode the general solution of the initial value problem for the Heisenberg equations of motion and extends to the study of quench correlations.

A simple way to demonstrate the above observation is to compare the equations of motion for the inhomogeneous TLL with the homogeneous model. We already calculated the equations for the velocity and relative density fields for both cases in section 6.4.2. At the end of that section, we even already pointed out the differences. In the following, let's do a more detailed comparison between eqs. (6.27) and (6.32), by taking the derivatives and sorting the terms by the order of spatial derivatives from highest to lowest for the inhomogeneous TLL, that is

$$\partial_t^2 \hat{u}(z,t) = v^2 \partial_z^2 \hat{u}(z,t) + 4vv'\partial_z \hat{\mathbf{u}}(z,t) + 2({v'}^2 + vv'')\hat{u}(z,t) \ , \tag{6.59}$$

and then for the homogeneous TLL

$$\partial_t^2 \hat{\mathbf{u}}(z,t) = v^2 \partial_z^2 \hat{\mathbf{u}}(z,t) + vv'\partial_z \hat{\mathbf{u}}(z,t) + ({v'}^2 + vv'')\hat{\mathbf{u}}(z,t) \ , \tag{6.60}$$

where $v \equiv v(z)$, $v' \equiv \partial_z v(z)$, and $v'' \equiv \partial_z^2 v(z)$. As we see in eqs. (6.59) and (6.60), the terms with the highest order derivative are identical in both cases and the only differences in the second and third terms are constant numerical factors, 4 and 2 respectively. Although we showed that the two equations are indeed *inequivalent*, since the highest derivative terms are identical, the motion of the fastest particles has the same form and velocity. Hence, the first signal carrying the information of a local disturbance travels equally fast in both cases, resulting in the same post-quench dynamics for the correlation fronts given the same initial state.

6.5 Outlook

In this chapter, I showed how our experimental setup paves the way for conducting detailed investigations into dynamics and correlations within an inhomogeneous simulated metric. Leveraging the spatially resolved field, denoted as ϕ, alongside the precise control offered by the optical dipole trap introduced in chapter 4, which shapes the spatiotemporal evolution of the averaged background density, yields a versatile and powerful platform.

Specifically, by designing $v(z) \sim z^{-\kappa}$, we can explore the potential divergence of signaling time for $\kappa < 1$, shedding light on physics near smoothed boundaries where corrections to the action need to be considered.

Beyond simulating dynamics in curved space-times, our presented quantum field simulator holds promise for studying inhomogeneous $1+1$-dimensional quantum fluids, an area of significant theoretical interest. In particular, it can be employed to investigate the inhomogeneous TLL model with a spatially dependent $K(z)$, which is expected to exhibit a breaking of the Huygens-Fresnel principle.

Furthermore, here, we only focused on a free non-interacting field theory. Nevertheless, by tuning the strength of the tunneling coupling J, we can explore the realm of interacting and strongly correlated quantum fields. Prior research has well understood the equilibrium properties of this system, effectively described by the sine-Gordon model. However, delving into the dynamics of its excitations and the resulting information transfer poses theoretical challenges and exciting prospects for future experimental endeavors.

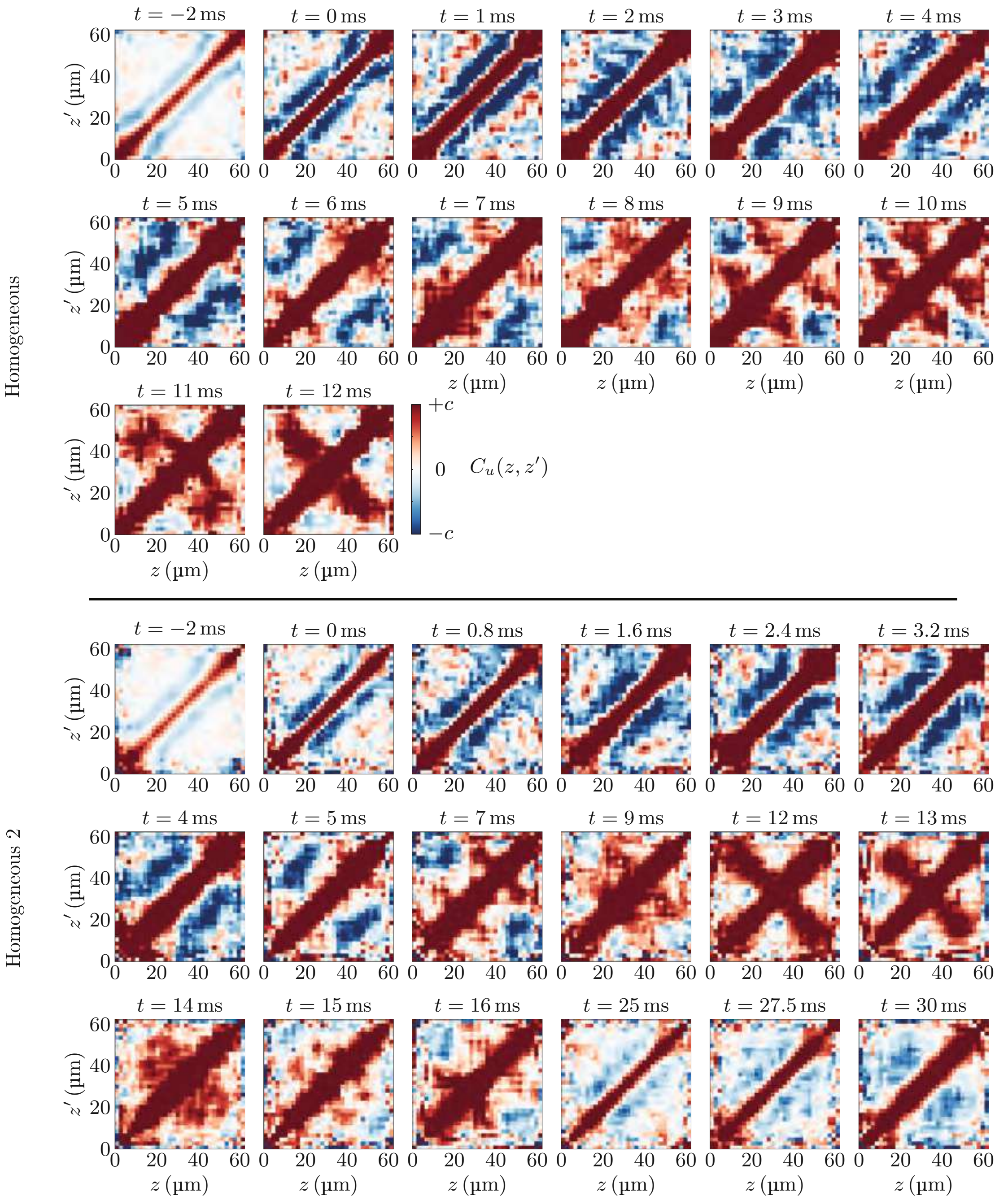

Figure 6.9 Measurement results of $C_u(z, z')$ at different times t for two settings with homogeneous background density.

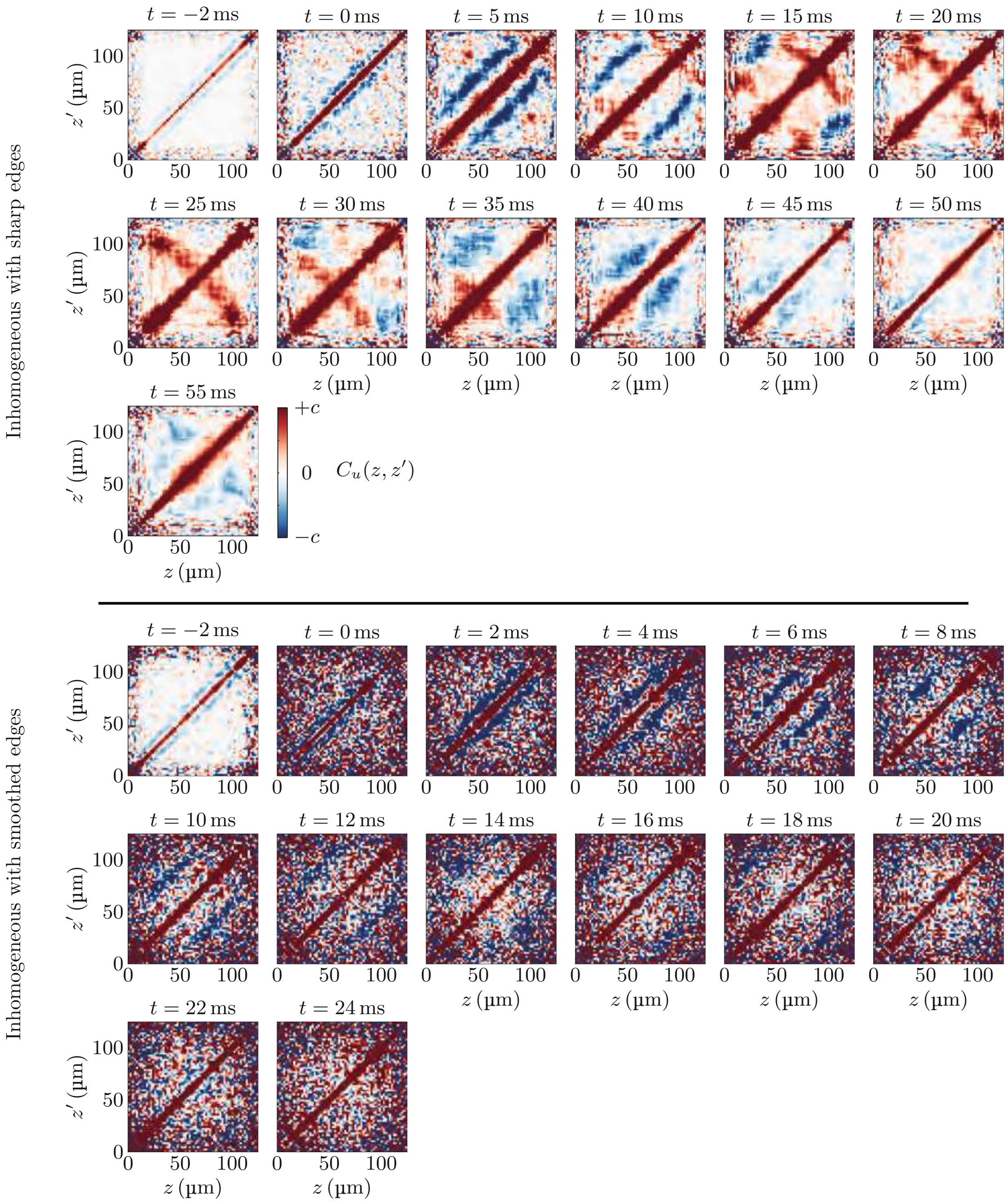

Figure 6.10 Measurement results of $C_u(z, z')$ at different times t for two settings with inhomogeneous background density.

Chapter 7

Final words

Conclusions and future directions

In chapters 5 and 6, I presented the results of the analog simulation of Klein-Gordon Hamiltonian using our tunneling-coupled condensates. We saw the experimental verification of the area law of mutual information and the light-cone propagation of correlation fronts on flat and curved simulated metrics. Although our discussion was limited to a free theory, both main tunable parameters of our quantum simulator, namely the single-particle tunneling rate and the background density, can be used to simulate non-linear theories, as mentioned in the outlooks of each chapter.

Another exciting direction is to use the trapping techniques introduced in chapter 4 to induce a space-dependent coupling in the sine-Gordon model. The key to these types of measurements is the contribution of the average density to the tunneling term in eq. (2.34), $2\hbar J \rho_0(z)\cos(\hat{\varphi}_-(z))$. This technique can be used to engineer different boundary conditions.

We are also planning a few technical improvements to the setup. One of the first steps is the implementation of machine-learning-based DMD pattern optimization for dynamic traps. Furthermore, we are planning to apply these techniques to modify transverse trapping using dipole traps.

Appendix A

Cosine transformations

In chapter 5, we introduced the eigenfunctions (eq. (5.23)) diagonalizing the TLL Hamiltonian in a box-like potential with hard walls,

$$\hat{H}_{\mathrm{TLL}} = \int_0^L dz \left[g_{\mathrm{1D}} \delta\hat{\rho}^2(z) + \frac{\hbar^2 n_{\mathrm{1D}}}{4m} \left(\partial_z \hat{\varphi}(z)\right)^2 \right] .$$

In this chapter, we go one step back and derive the coefficients of the cosine basis function by making an Ansatz following [98] with the minor difference that we will also include the zero modes. We check the consistency of our convention with dimensional analysis in section A.1 and then in section A.2 construct the discrete version of the cosine transformation to perform inverse Fourier transforms and obtain the covariance matrix in position space. This chapter is based on Ivan Kukuljan's notes, developed during our project [44].

Expanding the relative phase and the relative density fluctuation fields gives

$$\hat{\varphi}(t,z) = \sum_{n=0}^{\infty} f_n^{\hat{\varphi}}(z) \hat{\varphi}_n(t) ,$$
$$\delta\hat{\rho}(t,z) = \sum_{n=0}^{\infty} f_n^{\delta\hat{\rho}}(z) \delta\hat{\rho}_n(t) .$$

The commutation relation reads

$$[\delta\hat{\rho}_m(t), \hat{\varphi}_n(t)] = \mathrm{i}\delta_{m,n} .$$

The Ansatz for the wavefunctions is

$$f_n^{\hat\varphi}(z) = \begin{cases} \kappa_n^{\hat\varphi}\sqrt{\frac{2}{L}}\cos\left(n\frac{\pi}{L}z\right) & n>0 \\ \kappa_0^{\hat\varphi}\sqrt{\frac{1}{L}} & n=0 \end{cases}$$
$$f_n^{\delta\hat\rho}(z) = \begin{cases} \kappa_n^{\delta\hat\rho}\sqrt{\frac{2}{L}}\cos\left(n\frac{\pi}{L}z\right) & n>0 \\ \kappa_0^{\delta\hat\rho}\sqrt{\frac{1}{L}} & n=0 \end{cases} .$$

To obtain the coefficients, we first construct the Hamiltonian with these bases. We start with the derivative of the phase

$$\partial_z\hat\varphi(z) = -\kappa^{\hat\varphi}\sqrt{\frac{2}{L}}\sum_{n=1}^{\infty}\hat\varphi_n(t)n\frac{\pi}{L}\sin\left(n\frac{\pi}{L}z\right) ,$$

and then:

$$\begin{aligned}\hat H_{\mathrm{TLL}} &= g_{\mathrm{1D}}\left(\kappa_0^{\delta\hat\rho}\right)^2(\delta\hat\rho_0)^2 + \sum_{n=1}^{\infty}\left[g_{\mathrm{1D}}\left(\kappa_n^{\delta\hat\rho}\right)^2(\delta\hat\rho_n)^2 + \frac{\hbar^2 n_{\mathrm{1D}}}{4m}\left(\kappa_n^{\hat\varphi}\right)^2\left(n\frac{\pi}{L}\right)^2(\hat\varphi_n)^2\right] \\ &= \frac{1}{2}\hbar u\frac{1}{2}\sum_{n=1}^{\infty}\hbar\omega_n\left[(\delta\hat\rho_n)^2+(\hat\varphi_n)^2\right] .\end{aligned}$$

Comparing the coefficients yields (for $n>0$)

$$\begin{aligned} g_{\mathrm{1D}}\left(\kappa_n^{\delta\hat\rho}\right)^2 &= \frac{1}{2}\hbar\omega_n , \\ \frac{\hbar^2 n_{\mathrm{1D}}}{4m}\left(\kappa_n^{\hat\varphi}\right)^2\left(n\frac{\pi}{L}\right)^2 &= \frac{1}{2}\hbar\omega_n .\end{aligned}$$

This is a set of two equations for three variables. We will find the third equation by imposing the canonical commutation relations of the fields,

$$[\hat\varphi(x),\delta\hat\rho(y)] = \mathrm{i}\delta(x-y) .$$

Let's compute:

$$\begin{aligned}[\hat\varphi(x),\delta\hat\rho(y)] &= \sum_{m,n=0}^{\infty} f_m^{\hat\varphi}(x)f_n^{\delta\hat\rho}(y)\,[\hat\varphi_m,\delta\hat\rho_n] \\ &= -\mathrm{i}\frac{1}{L}\kappa_0^{\hat\varphi}\kappa_0^{\delta\hat\rho} - \mathrm{i}\sum_{n=1}^{\infty}\kappa_n^{\hat\varphi}\kappa_n^{\delta\hat\rho}\frac{2}{L}\cos\left(n\frac{\pi}{L}x\right)\cos\left(n\frac{\pi}{L}y\right) \\ &= -\mathrm{i}\frac{1}{L}\kappa_0^{\hat\varphi}\kappa_0^{\delta\hat\rho} - \mathrm{i}\sum_{n=1}^{\infty}\kappa_n^{\hat\varphi}\kappa_n^{\delta\hat\rho}\frac{1}{L}\left[\cos\left(n\frac{\pi}{L}(x-y)\right)+\cos\left(n\frac{\pi}{L}(x+y)\right)\right]\end{aligned}$$

Where we used the trigonometric identity $\cos u \cos v = \frac{1}{2}\left[\cos(u-v) + \cos(u+v)\right]$. We will now apply the Dirac comb formula, $\delta(x) = \frac{1}{2\pi} + \frac{1}{\pi}\sum_{k=1}^{\infty}\cos(kx)$,

$$\begin{aligned}
[\hat{\varphi}(x), \delta\hat{\rho}(y)] = -\mathrm{i}\frac{\pi}{L}\Bigg(&\frac{1}{2\pi}\kappa_0^{\hat{\varphi}}\kappa_0^{\delta\hat{\rho}} + \frac{1}{2\pi}\kappa_0^{\hat{\varphi}}\kappa_0^{\delta\hat{\rho}} \\
&+ \sum_{n=1}^{\infty}\kappa_n^{\hat{\varphi}}\kappa_n^{\delta\hat{\rho}}\left[\frac{1}{\pi}\cos\left(n\frac{\pi}{L}(x-y)\right) + \frac{1}{\pi}\cos\left(n\frac{\pi}{L}(x+y)\right)\right]\Bigg) \\
&= \mathrm{i}\frac{\pi}{L}\left[\delta\left(\frac{\pi}{L}(x-y)\right) + \delta\left(\frac{\pi}{L}(x+y)\right)\right] \\
&= \mathrm{i}\left[\delta(x-y) + \delta(x+y)\right] \\
&\underset{0\le x,y\le L}{=} \mathrm{i}\delta(x-y)\ .
\end{aligned}$$

To obtain this result, in the first line, we have multiplied and divided by π and added and subtracted $1/\pi$ inside the parentheses. In the second line, we have assumed

$$\kappa_n^{\hat{\varphi}}\kappa_n^{\delta\hat{\rho}} = -1\ ,$$

which gives us the missing relation to determine the coefficients. In the third line we have used $\delta(ax) = \frac{1}{|a|}\delta(x)$. An important observation is that it is crucial to include the zero mode to obtain the correct commutation relations. Solving the set of equations,

$$\begin{aligned}
g_{1\mathrm{D}}\left(\kappa_n^{\delta\hat{\rho}}\right)^2 &= \frac{1}{2}\hbar\omega_n\ , \\
\frac{\hbar^2 n_{1\mathrm{D}}}{4m}\left(\kappa_n^{\hat{\varphi}}\right)^2\left(n\frac{\pi}{L}\right)^2 &= \frac{1}{2}\hbar\omega_n\ , \qquad\qquad n>0 \\
\kappa_n^{\hat{\varphi}}\kappa_n^{\delta\hat{\rho}} &= -1\ ,
\end{aligned}$$

for $n>0$, gives

$$\begin{aligned}
\omega_n &= \sqrt{\frac{g_{1\mathrm{D}}n_{1\mathrm{D}}}{m}}\left(n\frac{\pi}{L}\right)\ , \\
\kappa_n^{\hat{\varphi}} &= \left(\frac{1}{n}\frac{2L}{\hbar\pi}\sqrt{\frac{g_{1\mathrm{D}}m}{n_{1\mathrm{D}}}}\right)^{1/2} = \sqrt{\frac{2}{\hbar}\frac{g_{1\mathrm{D}}}{\omega_n}}\ , \\
\kappa_n^{\delta\hat{\rho}} &= -\left(n\frac{\hbar\pi}{2L}\sqrt{\frac{n_{1\mathrm{D}}}{g_{1\mathrm{D}}m}}\right)^{1/2} = -\sqrt{\frac{\hbar}{2}\frac{\omega_n}{g_{1\mathrm{D}}}}\ .
\end{aligned}$$

And for the zero modes, we get

$$\begin{aligned}
\kappa_0^{\hat{\varphi}} &= \sqrt{L}\,, \\
\kappa_0^{\delta\hat{\rho}} &= -\frac{1}{\sqrt{L}}\,, \\
u &= \frac{2g_{1\mathrm{D}}}{\hbar L}\,.
\end{aligned}$$

Setting $\kappa_0^{\hat{\varphi}}$ and $\kappa_0^{\delta\hat{\rho}}$ we had some freedom but we chose them that way that $\hat{\varphi}_0$ and $\delta\hat{\rho}_0$ are dimensionless. So, our result for the wavefunction is:

$$\begin{aligned}
f_n^{\hat{\varphi}}(z) &= \begin{cases} \kappa_n^{\hat{\varphi}}\sqrt{\frac{2}{L}}\cos\left(n\frac{\pi}{L}z\right) & n > 0 \\ \kappa_0^{\hat{\varphi}}\sqrt{\frac{1}{L}} & n = 0 \end{cases} \\
&= \begin{cases} 2\left(\frac{1}{n}\frac{1}{\hbar\pi}\sqrt{\frac{g_{1\mathrm{D}}m}{n_{1\mathrm{D}}}}\right)^{1/2}\cos\left(n\frac{\pi}{L}z\right) & n > 0 \\ 1 & n = 0 \end{cases} \\
f_n^{\delta\hat{\rho}}(z) &= \begin{cases} \kappa_n^{\delta\hat{\rho}}\sqrt{\frac{2}{L}}\cos\left(n\frac{\pi}{L}z\right) & n > 0 \\ \kappa_0^{\delta\hat{\rho}}\sqrt{\frac{1}{L}} & n = 0 \end{cases} \\
&= \begin{cases} -\frac{1}{L}\left(n\hbar\pi\sqrt{\frac{n_{1\mathrm{D}}}{g_{1\mathrm{D}}m}}\right)^{1/2}\cos\left(n\frac{\pi}{L}z\right) & n > 0 \\ -\frac{1}{L} & n = 0 \end{cases}
\end{aligned}$$

A.1 Dimensional analysis

Because $\left[\hat{H}_{\mathrm{TLL}}\right] = \mathrm{J}$, $[\hbar] = \mathrm{J\,s}$, $[g_{1\mathrm{D}}] = \mathrm{J\,m}$, $[\partial_z] = \mathrm{m}^{-1}$, $[n_{1\mathrm{D}}] = \mathrm{m}^{-1}$, $[m] = \mathrm{kg}$ and $\left[\int_0^L dz\right] = \mathrm{m}$ we have

$$\begin{aligned}
[\hat{\varphi}(z)] &= 1 \\
[\delta\hat{\rho}(z)] &= \mathrm{m}^{-1}
\end{aligned}$$

$$\left[\kappa_n^{\hat{\varphi}}\sqrt{\frac{2}{L}}\right] = \left[\left(\frac{1}{n}\frac{4}{\hbar\pi}\sqrt{\frac{g_{1\mathrm{D}}m}{n_{1\mathrm{D}}}}\right)^{1/2}\right] = 1 \tag{A.1}$$

$$\left[\kappa_n^{\delta\hat{\rho}}\sqrt{\frac{2}{L}}\right] = \left[\sqrt{\frac{2}{L}}\left(n\frac{\hbar\pi}{2L}\sqrt{\frac{n_{1\mathrm{D}}}{g_{1\mathrm{D}}m}}\right)^{1/2}\right] = \mathrm{m}^{-1} \tag{A.2}$$

Die approbierte gedruckte Originalversion dieser Dissertation ist an der TU Wien Bibliothek verfügbar.
The approved original version of this doctoral thesis is available in print at TU Wien Bibliothek.
TU Bibliothek Your knowledge hub WIEN

So that

$$[\hat{\varphi}_n] = 1$$
$$[\delta\hat{\rho}_n] = 1$$

A.2 Discrete cosine transform

Let's now use the discrete cosine transformation (type II and its inverse, which is type III[1]) to approximate our system with a spin chain. This step is necessary to protect the canonical invariance and satisfy the Heisenberg uncertainty relation after transforming back to position space from the momentum modes. We thus have

$$X_n = \frac{1}{\sqrt{N}} y_0 + \sqrt{\frac{2}{N}} \sum_{k=1}^{N-1} y_k \cos\left(\frac{\pi}{N}(n+\frac{1}{2})k\right) \ ,$$

$$y_k = \begin{cases} \sqrt{\frac{2}{N}} \sum_{n=0}^{N-1} X_n \cos\left(\frac{\pi}{N}(n+\frac{1}{2})k\right) & k = 1, \dots N-1 \\ \sqrt{\frac{1}{N}} \sum_{n=0}^{N-1} X_n & k = 0 \end{cases} .$$

This assumption splits the position space (grid with index n) into N intervals and assigns a degree of freedom in the middle of every interval ($\frac{1/2}{N}L$, $\frac{1+1/2}{N}L$,...,$\frac{N-1/2}{N}L$). In momentum space, the modes are $k = 0, 1, 2, \dots N-1$ and the zero mode $k = 0$ is treated separately, corresponding to the Neumann boundary conditions. That the above transforms are inverses of one another can be checked using the relations:

$$\sum_{n=0}^{N-1} \cos\left(\frac{\pi}{N}(n+\frac{1}{2})l\right) \cos\left(\frac{\pi}{N}(n+\frac{1}{2})k\right) = \frac{N}{2}\delta_{k,l} \ ,$$
$$\sum_{k=1}^{N-1} \cos\left(\frac{\pi}{N}(n+\frac{1}{2})k\right) \cos\left(\frac{\pi}{N}(l+\frac{1}{2})k\right) = -\frac{1}{2}\delta_{n\neq l} + \frac{N-1}{2}\delta_{n,l} \ ,$$
$$\sum_{n=0}^{N-1} \cos\left(\frac{\pi}{N}(n+\frac{1}{2})k\right) = N\delta_{k,0} \ .$$

which can be checked in Mathematica.

---

[1] https://docs.scipy.org/doc/scipy/reference/generated/scipy.fftpack.dct.html

Now, we try to make this compatible with our convention.

$$\hat{\varphi}(t,z_n) = \sum_{k=0}^{N-1} f_k^{\hat{\varphi}}(z_n)\hat{\varphi}_k(t)$$
$$\delta\hat{\rho}(t,z_n) = \sum_{k=0}^{N-1} f_k^{\delta\hat{\rho}}(z_n)\delta\hat{\rho}_k(t)$$

$$\begin{aligned}
f_k^{\hat{\varphi}}(z_n) &= \begin{cases} \kappa_k^{\hat{\varphi}}\sqrt{\tfrac{2}{L}}\cos\!\left(k\tfrac{\pi}{L}z_n\right) & k>0 \\ \kappa_0^{\hat{\varphi}}\sqrt{\tfrac{1}{L}} & k=0 \end{cases} \\
&= \begin{cases} 2\left(\tfrac{1}{k}\tfrac{1}{\hbar\pi}\sqrt{\tfrac{g_{1\mathrm{D}}m}{n_{1\mathrm{D}}}}\right)^{1/2}\cos\!\left(n\tfrac{\pi}{L}z_n\right) & k>0 \\ 1 & k=0 \end{cases} \\
&= \begin{cases} 2\xi_k\cos\left(k\tfrac{\pi}{N}(n+\tfrac{1}{2})\right) & k>0 \\ 1 & k=0 \end{cases} \\
f_k^{\delta\hat{\rho}}(z_k) &= \begin{cases} \kappa_k^{\delta\hat{\rho}}\sqrt{\tfrac{2}{L}}\cos\!\left(k\tfrac{\pi}{L}z_n\right) & k>0 \\ \kappa_0^{\delta\hat{\rho}}\sqrt{\tfrac{1}{L}} & k=0 \end{cases} \\
&= \begin{cases} -\tfrac{1}{L}\left(k\hbar\pi\sqrt{\tfrac{n_{1\mathrm{D}}}{g_{1\mathrm{D}}m}}\right)^{1/2}\cos\!\left(k\tfrac{\pi}{L}z_n\right) & k>0 \\ -\tfrac{1}{L} & k=0 \end{cases} \\
&= \begin{cases} -\tfrac{1}{Na}\tfrac{1}{\xi_k}\cos\left(k\tfrac{\pi}{N}(n+\tfrac{1}{2})\right) & k>0 \\ -\tfrac{1}{Na} & k=0 \end{cases}
\end{aligned}$$

Thus:

$$\hat{\varphi}(t,z_n) = \hat{\varphi}_0(t) + \sum_{k=1}^{N-1} 2\xi_k\cos\left(k\frac{\pi}{N}(n+\frac{1}{2})\right)\hat{\varphi}_k(t)\ ,$$
$$\delta\hat{\rho}(t,z_n) = -\frac{1}{Na}\delta\hat{\rho}_0(t) - \sum_{k=0}^{N-1}\frac{1}{Na}\frac{1}{\xi_k}\cos\left(k\frac{\pi}{N}(n+\frac{1}{2})\right)\delta\hat{\rho}_k(t)\ ,$$

with $z_n = (n+\frac{1}{2})a$, where $a = L/N$ is the lattice spacing, and N is the number of intervals or, equivalently, the number of momentum modes. We also defined

$$\xi_k \equiv \left(\frac{1}{k}\frac{1}{\hbar\pi}\sqrt{\frac{g_{1\mathrm{D}}m}{n_{1\mathrm{D}}}}\right)^{1/2}\ ,$$

and for convenience

$$\xi_0 \equiv 1 \; .$$

Now, we construct the inverse cosine transform,

$$\hat{\varphi}_k(t) = \frac{1}{N}\frac{1}{\xi_k}\sum_{n=0}^{N-1}\hat{\varphi}(t,z_n)\cos\left(\frac{\pi}{N}(n+\frac{1}{2})k\right)$$

$$\delta\hat{\rho}_k(t) = \begin{cases} -2a\xi_k\sum_{n=0}^{N-1}\delta\hat{\rho}(t,z_n)\cos\left(\frac{\pi}{N}(n+\frac{1}{2})k\right) & k = 1,\dots N-1 \\ -a\sum_{n=0}^{N-1}\delta\hat{\rho}(t,z_n) & k = 0 \end{cases}$$

Let's check if these are inverses of one another

$$\begin{aligned}\hat{\varphi}_k(t) &= \frac{1}{N}\frac{1}{\xi_k}\sum_{n=0}^{N-1}\hat{\varphi}(t,z_n)\cos\left(\frac{\pi}{N}(n+\frac{1}{2})k\right) \\ &= \frac{1}{N}\frac{1}{\xi_k}\hat{\varphi}_0(t)\sum_{n=0}^{N-1}\cos\left(\frac{\pi}{N}(n+\frac{1}{2})k\right) \\ &+\frac{1}{N}\frac{1}{\xi_k}\sum_{l=1}^{N-1}2\xi_l\hat{\varphi}_l(t)\sum_{n=0}^{N-1}\cos\left(l\frac{\pi}{N}(n+\frac{1}{2})\right)\cos\left(\frac{\pi}{N}(n+\frac{1}{2})k\right) \\ &= \frac{1}{N}\frac{1}{\xi_k}\xi_0\hat{\varphi}_0(t)N\delta_{k,0} + \frac{1}{N}\frac{1}{\xi_k}\sum_{l=1}^{\infty}2\xi_l\hat{\varphi}_l(t)\frac{N}{2}\delta_{k,l} \\ &= \hat{\varphi}_k(t)\end{aligned}$$

$$\begin{aligned}\hat{\varphi}(t,z_n) &= \frac{1}{N}\sum_{l=0}^{N-1}\hat{\varphi}(t,z_l) + \sum_{k=1}^{N-1}2\xi_k\cos\left(k\frac{\pi}{N}(n+\frac{1}{2})\right)\frac{1}{N}\frac{1}{\xi_k}\sum_{l=0}^{N-1}\hat{\varphi}(t,z_l)\cos\left(\frac{\pi}{N}(l+\frac{1}{2})k\right) \\ &= \frac{1}{N}\sum_{l=0}^{N-1}\hat{\varphi}(t,z_l) + \frac{2}{N}\sum_{l=0}^{N-1}\hat{\varphi}(t,z_l)\sum_{k=1}^{N-1}\cos\left(k\frac{\pi}{N}(n+\frac{1}{2})\right)\cos\left(\frac{\pi}{N}(l+\frac{1}{2})k\right) \\ &= \frac{1}{N}\sum_{l=0}^{N-1}\hat{\varphi}(t,z_l) + \frac{2}{N}\sum_{l=0}^{N-1}\hat{\varphi}(t,z_l)\left(-\frac{1}{2}\right)\delta_{n\neq l} + \frac{N-1}{N}\sum_{l=0}^{N-1}\hat{\varphi}(t,z_l)\delta_{n,l} \\ &= \hat{\varphi}(t,z_n)\end{aligned}$$

For $\delta\hat{\rho}_k$, with $k = 1, \dots N-1$ we get

$$\begin{aligned}
\delta\hat{\rho}_k(t) &= -2a\xi_k \left(-\frac{1}{Na}\delta\hat{\rho}_0(t)\right) \sum_{n=0}^{N-1} \cos\left(\frac{\pi}{N}(n+\frac{1}{2})k\right) \\
&\quad -2a\xi_k \sum_{n=0}^{N-1} \left(-\sum_{l=1}^{N-1} \frac{1}{Na}\frac{1}{\xi_l}\delta\hat{\rho}_l(t) \cos\left(l\frac{\pi}{N}(n+\frac{1}{2})\right)\right) \cos\left(\frac{\pi}{N}(n+\frac{1}{2})k\right) \\
&= \frac{2}{N}\sum_{l=1}^{\infty} \frac{1}{\xi_l}\delta\hat{\rho}_l(t)\frac{N}{2}\delta_{k,l} \\
&= \delta\hat{\rho}_k(t)
\end{aligned}$$

and for the zero mode, $k = 0$,

$$\begin{aligned}
\delta\hat{\rho}_0(t) &= -a\sum_{n=0}^{N-1}\left(-\frac{1}{Na}\delta\hat{\rho}_0(t)\right) - a\sum_{n=0}^{N-1}\left(-\sum_{l=1}^{N-1}\frac{1}{Na}\frac{1}{\xi_l}\cos\left(l\frac{\pi}{N}(n+\frac{1}{2})\right)\delta\hat{\rho}_l(t)\right) \\
&= -a\sum_{n=0}^{N-1}\delta\hat{\rho}(t,z_n) \\
&= \delta\hat{\rho}_0(t)
\end{aligned}$$

$$\begin{aligned}
\delta\hat{\rho}(t,z_n) &= -\frac{1}{Na}\left(-a\sum_{n=0}^{N-1}\delta\hat{\rho}(t,z_n)\right) \\
&\quad -\sum_{k=1}^{N-1}\frac{1}{Na}\frac{1}{\xi_k}\cos\left(k\frac{\pi}{N}(n+\frac{1}{2})\right)\left(-2a\xi_k\sum_{l=0}^{N-1}\delta\hat{\rho}(t,z_l)\cos\left(\frac{\pi}{N}(l+\frac{1}{2})k\right)\right) \\
&= \frac{1}{N}\sum_{n=0}^{N-1}\delta\hat{\rho}(t,z_n) + \frac{2}{N}\sum_{l=0}^{N-1}\delta\hat{\rho}(t,z_l)\left(-\frac{1}{2}\right)\delta_{n\neq l} + \frac{N-1}{N}\sum_{l=0}^{N-1}\delta\hat{\rho}(t,z_l)\delta_{n,l} \\
&= \delta\hat{\rho}(t,z_n)
\end{aligned}$$

These are the discrete versions of the cosine transformations introduced in eq. (5.23).

Die approbierte gedruckte Originalversion dieser Dissertation ist an der TU Wien Bibliothek verfügbar.
The approved original version of this doctoral thesis is available in print at TU Wien Bibliothek.
TU Bibliothek WIEN Your knowledge hub

References

[1] M. H. Anderson, J. R. Ensher, M. R. Matthews, C. E. Wieman, and E. A. Cornell, “Observation of bose-einstein condensation in a dilute atomic vapor,” *Science*, vol. 269, no. 5221, pp. 198–201, 1995.

[2] K. B. Davis, M. O. Mewes, M. R. Andrews, N. J. van Druten, D. S. Durfee, D. M. Kurn, and W. Ketterle, “Bose-einstein condensation in a gas of sodium atoms,” *Phys. Rev. Lett.*, vol. 75, pp. 3969–3973, Nov 1995.

[3] S. Bose, “Plancks Gesetz und Lichtquantenhypothese,” *Zeitschrift für Physik*, no. 26, p. 178, 1924.

[4] A. Einstein, “Quantentheorie des einatomigen idealen Gases,” *Sitzungsber. Kgl. Preuss. Akad. Wiss.*, p. 261, 1924.

[5] A. Einstein, “Quantentheorie des einatomigen idealen Gases (Zweite Abhandlung),” *Sitzungsber. Kgl. Preuss. Akad. Wiss.*, p. 3, 1925.

[6] I. Bloch, J. Dalibard, and W. Zwerger, “Many-body physics with ultracold gases,” *Rev. Mod. Phys.*, vol. 80, pp. 885–964, Jul 2008.

[7] I. Bloch, J. Dalibard, and S. Nascimbène, “Quantum simulations with ultracold quantum gases,” *Nature Physics*, vol. 8, pp. 267–276, 2012.

[8] H. Pichler, L. Bonnes, A. J. Daley, A. M. Läuchli, and P. Zoller, “Thermal vs. entanglement entropy: A measurement protocol for fermionic atoms with a quantum gas microscope,” *New J. Phys.*, vol. 15, p. 063003, 2013.

[9] C. Viermann, M. Sparn, N. Liebster, M. Hans, E. Kath, A. Parra-López, M. Tolosa-Simeón, N. Sánchez-Kuntz, T. Haas, H. Strobel, S. Floerchinger, and M. K. Oberthaler, “Quantum field simulator for dynamics in curved spacetime,” *arXiv:2202.10399*, 2022.

[10] C. L. Degen, F. Reinhard, and P. Cappellaro, “Quantum sensing,” *Rev. Mod. Phys.*, vol. 89, p. 035002, Jul 2017.

[11] T. Schumm, S. Hofferberth, L. M. Andersson, S. Wildermuth, S. Groth, I. Bar-Joseph, J. Schmiedmayer, and P. Krüger, “Matter-wave interferometry in a double well on an atom chip,” *Nature Physics*, vol. 1, no. 1, pp. 57–62, 2005.

[12] M. Gring, M. Kuhnert, T. Langen, T. Kitagawa, B. Rauer, M. Schreitl, I. Mazets, D. A. Smith, E. Demler, and J. Schmiedmayer, “Relaxation and prethermalization in an isolated quantum system,” *Science*, vol. 337, no. 6100, pp. 1318–1322, 2012.

[13] M. Gring, *Prethermalization in an Isolated Many Body System*. PhD thesis, TU Wien, 2012.

[14] M. Kuhnert, *Thermalization and Prethermalization in an ultracold Bose Gas*. PhD thesis, TU Wien, Nov 2013.

[15] T. Schweigler, V. Kasper, S. Erne, I. Mazets, B. Rauer, F. Cataldini, T. Langen, T. Gasenzer, J. Berges, and J. Schmiedmayer, "Experimental characterization of a quantum many-body system via higher-order correlations," *Nature*, vol. 545, p. 323, 2017.

[16] T. Schweigler, M. Gluza, M. Tajik, S. Sotiriadis, F. Cataldini, S.-C. Ji, F. S. Møller, J. Sabino, B. Rauer, J. Eisert, and J. Schmiedmayer, "Decay and recurrence of non-Gaussian correlations in a quantum many-body system," *Nature Phys.*, vol. 17, p. 559, 2021.

[17] B. Rauer, S. Erne, T. Schweigler, F. Cataldini, M. Tajik, and J. Schmiedmayer, "Recurrences in an isolated quantum many-body system," *Science*, 2018.

[18] F. Cataldini, F. Møller, M. Tajik, J. a. Sabino, S.-C. Ji, I. Mazets, T. Schweigler, B. Rauer, and J. Schmiedmayer, "Emergent Pauli blocking in a weakly interacting Bose gas," *Phys. Rev. X*, vol. 12, p. 041032, Dec 2022.

[19] M. Gluza, T. Schweigler, M. Tajik, J. Sabino, F. Cataldini, F. S. Møller, S.-C. Ji, B. Rauer, J. Schmiedmayer, J. Eisert, and S. Sotiriadis, "Mechanisms for the emergence of Gaussian correlations," *SciPost Phys.*, vol. 12, p. 113, 2022.

[20] C. Mora and Y. Castin, "Extension of Bogoliubov theory to quasicondensates," *Physical Review A*, vol. 67, p. 053615, May 2003.

[21] V. Gritsev, A. Polkovnikov, and E. Demler, "Linear response theory for a pair of coupled one-dimensional condensates of interacting atoms," *Phys. Rev. B*, vol. 75, p. 174511, May 2007.

[22] M. Peskin and D. Schroeder, *An introduction to quantum field theory*. Frontiers in Physics, Westview Press, 1995.

[23] J. Cuevas-Maraver, P. G. Kevrekidis, and F. Williams, eds., *The sine-Gordon model and its applications*. Nonlinear systems and complexity, Switzerland: Springer International Publishing, 2014.

[24] J. I. Cirac and P. Zoller, "Goals and opportunities in quantum simulation," *Nature Phys.*, vol. 8, p. 264, 2012.

[25] S. Weinfurtner, P. Jain, M. Visser, and C. W. Gardiner, "Cosmological particle production in emergent rainbow spacetimes," *Classical and Quantum Gravity*, vol. 26, p. 065012, feb 2009.

[26] C. Barceló, S. Liberati, and M. Visser, "Analogue gravity," *Living Rev. Rel.*, vol. 14, no. 1, pp. 1–159, 2011.

[27] M. J. Jacquet, S. Weinfurtner, and F. König, “The next generation of analogue gravity experiments,” *Philosophical Transactions of the Royal Society A: Mathematical, Physical and Engineering Sciences*, vol. 378, no. 2177, p. 20190239, 2020.

[28] J.-C. Jaskula, G. B. Partridge, M. Bonneau, R. Lopes, J. Ruaudel, D. Boiron, and C. I. Westbrook, “Acoustic analog to the dynamical Casimir effect in a Bose-Einstein condensate,” *Phys. Rev. Lett.*, vol. 109, p. 220401, Nov 2012.

[29] S. Eckel, A. Kumar, T. Jacobson, I. B. Spielman, and G. K. Campbell, “A rapidly expanding Bose-Einstein condensate: an expanding universe in the lab,” *Phys. Rev. X*, vol. 8, no. 2, p. 021021, 2018.

[30] B. P. Lanyon, C. Hempel, D. Nigg, M. Müller, R. Gerritsma, F. Zähringer, P. Schindler, J. T. Barreiro, M. Rambach, G. Kirchmair, M. Hennrich, P. Zoller, R. Blatt, and C. F. Roos, “Universal digital quantum simulation with trapped ions,” *Science*, vol. 334, pp. 57–61, 2011.

[31] B. P. Lanyon, C. Hempel, D. Nigg, M. Müller, R. Gerritsma, F. Zähringer, P. Schindler, J. T. Barreiro, M. Rambach, G. Kirchmair, M. Hennrich, P. Zoller, R. Blatt, and C. F. Roos, “Universal digital quantum simulation with trapped ions,” *Science*, vol. 334, pp. 57–61, 2011.

[32] A. A. Houck, H. E. Tuereci, and J. Koch, “On-chip quantum simulation with superconducting circuits,” *Nature Phys.*, vol. 8, p. 292, 2012.

[33] C. vom Hagen, *Towards a low-dimensional degenerate Fermi-Fermi-Bose mixture.* PhD thesis, Ruperto-Carola University of Heidelberg, Combined Faculties for the Natural Sciences and for Mathematics, 2008.

[34] B. Stix, “A new imaging system for dual-species atomchip experiments,” Master’s thesis, TU Wien, 2008.

[35] T. Langen, *Non-equilibrium dynamics of one-dimensional Bose gases.* PhD thesis, TU Wien, Oct 2013.

[36] B. Rauer, “Evaporative cooling of one-dimensional Bose gases,” Master’s thesis, TU Wien, Jun 2012.

[37] M. Tajik, “Arbitrary one-dimensional optical dipole potentials on an atom chip,” Master’s thesis, TU Wien, Jun 2017.

[38] B. Rauer, *Non-equilibrium dynamics beyond dephasing: Recurrences and loss induced cooling in one-dimensional Bose gases.* PhD thesis, TU Wien, Sep 2018.

[39] T. Schweigler, *Correlations and dynamics of tunnel-coupled one-dimensional Bose gases.* PhD thesis, TU Wien, Mar 2019.

[40] F. S. Moller, *Hydrodynamics of quasi one-dimensional Bose gases.* PhD thesis, TU Wien, Jan 2023.

[41] J. Sabino, *Quantum field machines with cold atoms.* PhD thesis, TU Wien and Instituto Superior Técnico, Jul 2023.

[42] S. A. Erne, *Far-From-Equilibrium Quantum Many-Body Systems: From Universal Dynamics to Statistical Mechanics.* PhD thesis, Universität Heidelberg, Jul 2018.

[43] M. L. Gluza, *Non-equilibrium dynamics in quantum simulators.* Dissertation, Freie Universität Berlin, 2020.

[44] M. Tajik, I. Kukuljan, S. Sotiriadis, B. Rauer, T. Schweigler, F. Cataldini, J. Sabino, F. Møller, P. Schüttelkopf, S.-C. Ji, D. Sels, E. Demler, and J. Schmiedmayer, "Verification of the area law of mutual information in a quantum field simulator," *Nature Physics*, 2023.

[45] M. Tajik, B. Rauer, T. Schweigler, F. Cataldini, J. Sabino, F. Møller, P. Schüttelkopf, S.-C. Ji, and J. Schmiedmayer, "Raw Data to 'Experimental verification of the area law of mutual information in quantum field theory', arXiv:2206.10563," July 2022.

[46] M. Tajik, M. Gluza, N. Sebe, P. Schüttelkopf, F. Cataldini, J. Sabino, F. Møller, S.-C. Ji, S. Erne, G. Guarnieri, S. Sotiriadis, J. Eisert, and J. Schmiedmayer, "Experimental observation of curved light-cones in a quantum field simulator," *Proceedings of the National Academy of Sciences*, vol. 120, no. 21, p. e2301287120, 2023.

[47] M. Tajik, P. Schüttelkopf, F. Cataldini, J. Sabino, F. Møller, S.-C. Ji, and J. Schmiedmayer, "Relative Phase Data to 'Experimental observation of curved light-cones in a quantum field simulator', arXiv:2209.09132," Sept. 2022.

[48] E. H. Lieb and W. Liniger, "Exact analysis of an interacting Bose gas. I. The general solution and the ground state," *Phys. Rev.*, vol. 130, no. 4, p. 1605, 1963.

[49] E. H. Lieb, "Exact analysis of an interacting Bose gas. II. The excitation spectrum," *Phys. Rev.*, vol. 130, pp. 1616–1624, May 1963.

[50] M. Girardeau, "Relationship between systems of impenetrable bosons and fermions in one dimension," *Journal of Mathematical Physics*, vol. 1, no. 6, pp. 516–523, 1960.

[51] C. Gerry and P. Knight, *Introductory Quantum Optics.* Cambridge University Press, 2004.

[52] N. K. Whitlock and I. Bouchoule, "Relative phase fluctuations of two coupled one-dimensional condensates," *Phys. Rev. A*, vol. 68, p. 053609, 2003.

[53] S. Beck, I. E. Mazets, and T. Schweigler, "Nonperturbative method to compute thermal correlations in one-dimensional systems," *Phys. Rev. A*, vol. 98, p. 023613, 2018.

[54] W. Ketterle, D. Durfee, and D. Stamper-Kurn, "Making, probing and understanding Bose-Einstein condensates," In Bose-Einstein condensation in atomic gases, Proceedings of the International School of Physics "Enrico Fermi", Course CXL, pp. 67–176, IOS Press, Amsterdam, 1999.

[55] J. Reichel and V. Vuletic, *Atom chips.* John Wiley & Sons, 2011.

[56] C. J. Pethick and H. Smith, *Bose–Einstein Condensation in Dilute Gases.* Cambridge University Press, 2 ed., 2008.

[57] N. P. Proukakis, D. W. Snoke, and P. B. Littlewood, *Universal Themes of Bose-Einstein Condensation.* Cambridge: Cambridge University Press, 2017.

[58] R. Folman, P. Krüger, D. Cassettari, B. Hessmo, T. Maier, and J. Schmiedmayer, "Controlling cold atoms using nanofabricated surfaces: Atom chips," *Phys. Rev. Lett.*, vol. 84, pp. 4749–4752, May 2000.

[59] M. H. T. Extavour, L. J. LeBlanc, J. McKeever, A. B. Bardon, S. Aubin, S. Myrskog, T. Schumm, and J. H. Thywissen, *Fermions on Atom Chips*, pp. 365–394. Wiley-VCH Verlag GmbH & Co. KGaA, 2011.

[60] J. D. Carter, O. Cherry, and J. D. D. Martin, "Electric-field sensing near the surface microstructure of an atom chip using cold rydberg atoms," *Phys. Rev. A*, vol. 86, p. 053401, Nov 2012.

[61] S. A. Meek, H. Conrad, and G. Meijer, "Trapping molecules on a chip," *Science*, vol. 324, no. 5935, pp. 1699–1702, 2009.

[62] J. M. Amini, J. Britton, D. Leibfried, and D. J. Wineland, *Micro-Fabricated Chip Traps for Ions*, pp. 395–420. Wiley-VCH Verlag GmbH & Co. KGaA, 2011.

[63] A. Al-Rjoub and J. Verdú, "Electronic detection of a single particle in a coplanar-waveguide penning trap," *Applied Physics B*, vol. 107, no. 4, pp. 955–964, 2012.

[64] R. Folman, P. Treutlein, and J. Schmiedmayer, *Atom Chip Fabrication*, pp. 61–117. Wiley-VCH Verlag GmbH & Co. KGaA, 2011.

[65] P. Krüger, X. Luo, M. W. Klein, K. Brugger, A. Haase, S. Wildermuth, S. Groth, I. Bar-Joseph, R. Folman, and J. Schmiedmayer, "Trapping and manipulating neutral atoms with electrostatic fields," *Phys. Rev. Lett.*, vol. 91, p. 233201, Dec 2003.

[66] S. Hofferberth, I. Lesanovsky, B. Fischer, J. Verdu, and J. Schmiedmayer, "Radiofrequency-dressed-state potentials for neutral atoms," *Nat Phys*, vol. 2, pp. 710–716, Oct 2006.

[67] B. Rauer, P. Grisins, I. E. Mazets, T. Schweigler, W. Rohringer, R. Geiger, T. Langen, and J. Schmiedmayer, "Cooling of a one-dimensional Bose gas," *Phys. Rev. Lett.*, vol. 116, p. 30402, 2016.

[68] D. A. Smith, S. Aigner, S. Hofferberth, M. Gring, M. Andersson, S. Wildermuth, P. Krüger, S. Schneider, T. Schumm, and J. Schmiedmayer, "Absorption imaging of ultracold atoms on atom chips," *Optics Express*, vol. 19, pp. 8471–8485, Apr 2011.

[69] S. Manz, R. Bücker, T. Betz, C. Koller, S. Hofferberth, I. E. Mazets, A. Imambekov, E. Demler, A. Perrin, J. Schmiedmayer, and T. Schumm, "Two-point density correlations of quasicondensates in free expansion," *Phys. Rev. A*, vol. 81, p. 031610(R), Mar 2010.

[70] F. Møller, T. Schweigler, M. Tajik, J. Sabino, F. Cataldini, S.-C. Ji, and J. Schmiedmayer, "Thermometry of one-dimensional Bose gases with neural networks," *Phys. Rev. A*, vol. 104, p. 043305, Oct 2021.

[71] M. Tajik, B. Rauer, T. Schweigler, F. Cataldini, J. Sabino, F. S. Møller, S.-C. Ji, I. E. Mazets, and J. Schmiedmayer, "Designing arbitrary one-dimensional potentials on an atom chip," *Opt. Express*, vol. 27, pp. 33474–33487, Nov 2019.

[72] Y. V. Gott, M. S. Ioffe, and V. G. Tel'kovskii *Nucl. Fusion Suppl.*, vol. 3, p. 1045, 1962.

[73] D. E. Pritchard, "Cooling neutral atoms in a magnetic trap for precision spectroscopy," *Phys. Rev. Lett.*, vol. 51, pp. 1336–1339, Oct 1983.

[74] P. Krüger, L. M. Andersson, S. Wildermuth, S. Hofferberth, E. Haller, S. Aigner, S. Groth, I. Bar-Joseph, and J. Schmiedmayer, "Potential roughness near lithographically fabricated atom chips," *Phys. Rev. A*, vol. 76, p. 063621, Dec 2007.

[75] R. Grimm, M. Weidemüller, and Y. B. Ovchinnikov, "Optical dipole traps for neutral atoms," vol. 42 of *Advances In Atomic, Molecular, and Optical Physics*, pp. 95 – 170, Academic Press, 2000.

[76] P. Zupancic, P. M. Preiss, R. Ma, A. Lukin, M. E. Tai, M. Rispoli, R. Islam, and M. Greiner, "Ultra-precise holographic beam shaping for microscopic quantum control," *Opt. Express*, vol. 24, pp. 13881–13893, Jun 2016.

[77] L. Salasnich, A. Parola, and L. Reatto, "Effective wave equations for the dynamics of cigar-shaped and disk-shaped Bose condensates," *Phys. Rev. A*, vol. 65, p. 043614, 2002.

[78] A. Deutschmann-Olek, M. Tajik, M. Calzavara, J. Schmiedmayer, T. Calarco, and A. Kugi, "Iterative shaping of optical potentials for one-dimensional bose-einstein condensates," in *2022 IEEE 61st Conference on Decision and Control (CDC)*, pp. 5801–5806, 2022.

[79] M. Calzavara, Y. Kuriatnikov, A. Deutschmann-Olek, F. Motzoi, S. Erne, A. Kugi, T. Calarco, J. Schmiedmayer, and M. Prüfer, "Optimizing optical potentials with physics-inspired learning algorithms," *Phys. Rev. Appl.*, vol. 19, p. 044090, Apr 2023.

[80] F. Cataldini, *(In progress)*. PhD thesis, TU Wien, Jul 2023.

[81] J. Schmiedmayer, "One-dimensional atomic superfluids as a model system for quantum thermodynamics," in *Thermodynamics in the Quantum Regime: Fundamental Aspects and New Directions* (F. Binder, L. A. Correa, C. Gogolin, J. Anders, and G. Adesso, eds.), pp. 823–851, Springer International Publishing, 2018.

[82] M. Gluza, J. Sabino, N. H. Y. Ng, G. Vitagliano, M. Pezzutto, Y. Omar, I. Mazets, M. Huber, J. Schmiedmayer, and J. Eisert, “Quantum field thermal machines,” *PRX Quantum*, vol. 2, p. 030310, 2021.

[83] R. Horodecki, P. Horodecki, M. Horodecki, and K. Horodecki, “Quantum entanglement,” *Rev. Mod. Phys.*, vol. 81, pp. 865–942, Jun 2009.

[84] P. Calabrese and J. Cardy, “Entanglement entropy and quantum field theory,” *Journal of Statistical Mechanics: Theory and Experiment*, vol. 2004, p. P06002, June 2004.

[85] P. Calabrese and J. Cardy, “Entanglement entropy and conformal field theory,” *Journal of Physics A: Mathematical and Theoretical*, vol. 42, p. 504005, Dec. 2009.

[86] M. M. Wolf, F. Verstraete, M. B. Hastings, and J. I. Cirac, “Area laws in quantum systems: Mutual information and correlations,” *Phys. Rev. Lett.*, vol. 100, p. 070502, Feb 2008.

[87] N. Schuch, M. M. Wolf, F. Verstraete, and J. I. Cirac, “Entropy scaling and simulability by matrix product states,” *Phys. Rev. Lett.*, vol. 100, p. 030504, Jan 2008.

[88] J. Eisert, M. Cramer, and M. B. Plenio, “Colloquium: Area laws for the entanglement entropy,” *Reviews of Modern Physics*, vol. 82, pp. 277–306, Feb. 2010.

[89] J. Polchinski, “The Black Hole Information Problem,” in *New Frontiers in Fields and Strings*, (Boulder, Colorado), pp. 353–397, WORLD SCIENTIFIC, Jan. 2017.

[90] L. Luo, B. Clancy, J. Joseph, J. Kinast, and J. E. Thomas, “Measurement of the entropy and critical temperature of a strongly interacting Fermi gas,” *Phys. Rev. Lett.*, vol. 98, p. 080402, Feb 2007.

[91] R. Islam, R. Ma, P. M. Preiss, M. Eric Tai, A. Lukin, M. Rispoli, and M. Greiner, “Measuring entanglement entropy in a quantum many-body system,” *Nature*, vol. 528, pp. 77–83, Dec 2015.

[92] E. Cocchi, L. A. Miller, J. H. Drewes, C. F. Chan, D. Pertot, F. Brennecke, and M. Köhl, “Measuring entropy and short-range correlations in the two-dimensional Hubbard model,” *Phys. Rev. X*, vol. 7, p. 031025, Aug 2017.

[93] T. Brydges, A. Elben, P. Jurcevic, B. Vermersch, C. Maier, B. P. Lanyon, P. Zoller, R. Blatt, and C. F. Roos, “Probing Rényi entanglement entropy via randomized measurements,” *Science*, vol. 364, no. 6437, pp. 260–263, 2019.

[94] K. Modi, A. Brodutch, H. Cable, T. Paterek, and V. Vedral, “The classical-quantum boundary for correlations: Discord and related measures,” *Rev. Mod. Phys.*, vol. 84, pp. 1655–1707, Nov 2012.

[95] J. Zhang and S. L. Braunstein, "Continuous-variable gaussian analog of cluster states," *Phys. Rev. A*, vol. 73, p. 032318, Mar 2006.

[96] T. F. Demarie, "Pedagogical introduction to the entropy of entanglement for gaussian states," *European Journal of Physics*, vol. 39, p. 035302, mar 2018.

[97] M. Le Bellac, *Thermal field theory.* Cambridge Monographs on Mathematical Physics, Cambridge University Press, 1996.

[98] M. Gluza, T. Schweigler, B. Rauer, C. Krumnow, J. Schmiedmayer, and J. Eisert, "Quantum read-out for cold atomic quantum simulators," *Comm. Phys.*, vol. 3, p. 12, 2020.

[99] T. Berrada, S. van Frank, R. Bücker, T. Schumm, J.-F. Schaff, and J. Schmiedmayer, "Integrated Mach–Zehnder interferometer for Bose–Einstein condensates," *Nature Communications*, vol. 4, June 2013.

[100] B. Efron and R. Tibshirani, "Bootstrap methods for standard errors, confidence intervals, and other measures of statistical accuracy," *Statist. Sci.*, vol. 1, pp. 54–75, 02 1986.

[101] D. Katsinis and G. Pastras, "An inverse mass expansion for the mutual information in free scalar qft at finite temperature," *Journal of High Energy Physics*, vol. 2020, p. 91, Feb 2020.

[102] T. Schweigler, V. Kasper, S. Erne, I. Mazets, B. Rauer, F. Cataldini, T. Langen, T. Gasenzer, J. Berges, and J. Schmiedmayer, "Experimental characterization of a quantum many-body system via higher-order correlations," *Nature*, vol. 545, p. 323, 2017.

[103] I. Kukuljan, S. Sotiriadis, and G. Takacs, "Correlation functions of the quantum sine-Gordon model in and out of equilibrium," *Phys. Rev. Lett.*, vol. 121, p. 110402, Sep 2018.

[104] P. Emonts and I. Kukuljan, "Reduced density matrix and entanglement of interacting quantum field theories with hamiltonian truncation," Jul 2022.

[105] P. Calabrese and J. Cardy, "Time Dependence of Correlation Functions Following a Quantum Quench," *Phys. Rev. Lett.*, vol. 96, Apr. 2006.

[106] P. Calabrese and J. Cardy, "Quantum quenches in extended systems," *J. Stat. Mech.*, vol. 2007, pp. P06008–P06008, June 2007.

[107] M. Cramer, C. M. Dawson, J. Eisert, and T. J. Osborne, "Exact relaxation in a class of nonequilibrium quantum lattice systems," *Phys. Rev. Lett.*, vol. 100, p. 030602, 2008.

[108] F. H. L. Essler and M. Fagotti, "Quench dynamics and relaxation in isolated integrable quantum spin chains," *J. Stat. Mech.*, vol. 2016, p. 064002, jun 2016.

[109] G. Ramírez, J. Rodríguez-Laguna, and G. Sierra, "Entanglement over the rainbow," *J. Stat. Mech.*, vol. 2015, no. 6, p. P06002, 2015.

[110] F. Dalfovo, L. Pitaevskii, and S. Stringari, "Order parameter at the boundary of a trapped Bose gas," *Phys. Rev. A*, vol. 54, pp. 4213–4217, Nov 1996.

[111] M. Gluza, P. Moosavi, and S. Sotiriadis, "Breaking of Huygens–Fresnel principle in inhomogeneous Tomonaga–Luttinger liquids," *J. Phys. A*, vol. 55, p. 054002, Jan. 2022.

[112] Y. Brun and J. Dubail, "The inhomogeneous Gaussian free field, with application to ground state correlations of trapped 1d Bose gases," *SciPost Phys.*, vol. 4, p. 013102, 2018.

Curriculum Vitae

Personal data

Name:	Mohammadamin Tajik
Date of birth:	[redacted]
Place of birth:	[redacted]
E-mail:	amintajik.physics@gmail.com
LinkedIn:	https://www.linkedin.com/in/amintajik/

Academic education

Since 07/2017	Technische Universität Wien, Vienna, Austria Doctoral program Technical Physics
01/2023 - 05/2023	Caltech, Pasadena, USA Visiting Student Researcher (VSR), Biophysics
02/2014 - 06/2017	Technische Universität Wien, Vienna, Austria Master's program Technical Physics
09/2009 - 07/2013	University of Tehran, Tehran, Iran Bachelor's program Physics

Master's thesis

Title	Arbitrary One-Dimensional Optical Dipole Potentials on an Atom Chip
Supervisors	Prof. Jörg Schmiedmayer and Dr. Bernhard Rauer